

Chapter 1

INTRODUCTION

1.1. Preliminary Considerations

Compared with its three-phase counterpart, a multiphase machine (machine with more than three phases) provides many additional benefits, such as lower torque ripple, lower per phase power/current (for the same overall power rating), possibility of achieving torque enhancement via harmonic injection, a possibility of operating multiple motor drive systems with independent control using a single multiphase power electronic converter, better fault tolerance, etc. (Levi *et al.*, 2008). For the past few decades, there has been an increasing interest in the field of multiphase machine and drive research, with some practical applications in the field of electric ship propulsion and electric transportation (Simoes and Vieira, 2002; Parsa and Toliyat, 2007; Jung *et al.*, 2012; Villani *et al.*, 2012), and wind energy conversion systems (Gonzalez *et al.*, 2006; Brisset *et al.*, 2008; Parker *et al.*, 2011; Xiang-Jun *et al.*, 2012; Yuan *et al.*, 2012). Among the multiphase machines, those with multiple three-phase windings (such as six-phase, nine-phase or eighteen-phase machine) are most frequently discussed. While having the benefits of a multiphase machine, the modular three-phase structures allow the use of the well-established three-phase technology and equipment, thus providing an easier and less costly transition from three-phase system to a multiphase system.

For the particular case of a six-phase machine, the stator windings can be wound in such a way that the two three-phase windings (denoted as $a1b1c1$ and $a2b2c2$) are spatially shifted by an angle of 30° or 60° degrees, as shown in Fig. 1.1. The former is known as an asymmetrical six-phase machine, while the latter is usually called a symmetrical six-phase machine. In general, an asymmetrical six-phase machine is the preferred choice, since a symmetrical six-phase machine is in essence a three-phase machine where two phase belts under the different magnetic poles are not connected in series and are taken out as separate phases. The asymmetrical configuration has a better dc-bus voltage utilisation when operated with a single neutral point, than the symmetrical one (where maximum modulation index in the linear region is restricted to 1 when there is a single neutral point). However, the advancements in power electronics technology and the recent development of pulse-width modulation techniques for both machine configurations enable the two machines to be controlled in such a way that the achieved performance is practically the same.

In (Munoz and Lipo, 2000), a special type of a six-phase induction machine was presented, where the two three-phase windings of the machine are wound with different pole number ratio of 1:3. With this dissimilar pole configuration, this machine was reported to have several advantages over conventional six-phase machines, such as ease of sensorless control, better utilization of stator windings and the elimination of circulating currents (Wu *et al.*, 2007). Nevertheless, the structure of the winding is more complicated, hence less popular than the standard six-phase machine with the same pole number for both three-phase windings.

In this thesis, investigations are done for an asymmetrical six-phase induction machine with regular winding (the same number of poles), in an attempt to explore and provide additional contributions to the control of the machine. Through the literature survey, reported in Chapter 2, three areas have been identified as the focus of this thesis,

i.e. current control methods, development and control of alternative converter topologies, and post-fault control.

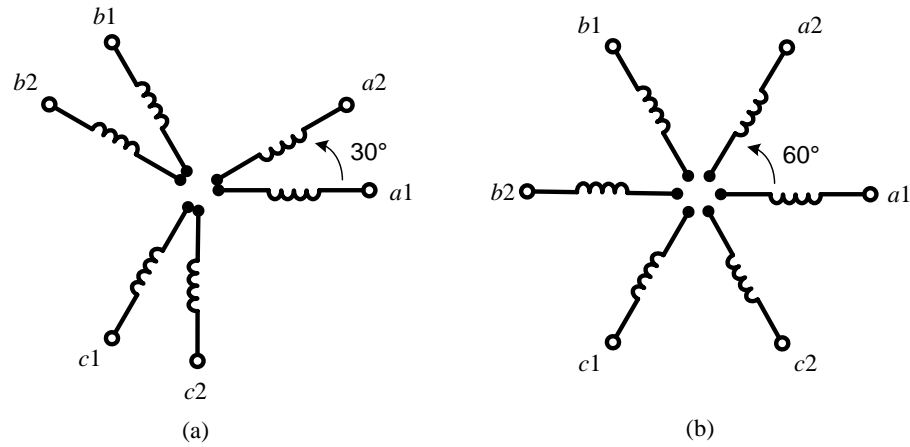


Fig. 1.1.1. Stator winding arrangement for (a) asymmetrical and (b) symmetrical six-phase machine.

1.2. Objectives

The main objectives of this thesis are as follows:

- i) To compare the performance of different current control methods for an asymmetrical six-phase induction machine. Special attention is given to the compensation of machine/converter asymmetries and dead-time effect.
- ii) To investigate the operation of an asymmetrical six-phase induction machine using series-connected machine-side converters. The investigation will include analysis of the topology and its control, in order to identify its potential merits and demerits.
- iii) To develop post-fault control strategies for an asymmetrical six-phase machine, with PI controller-based current control.
- iv) To build test-rig, which will allow experimental verifications of new and original theoretical research results, arrived at by meeting objectives (iv) to (vi). The test-rig will consist of an asymmetrical six-phase induction machine

coupled to a dc-machine (as load), with control algorithms developed using a dSpace platform.

1.3. Thesis Novelty and Originality

The original research results of the investigation are presented in Chapters 3-5 of this thesis. Following are the novel contributions provided by this thesis:

- 1) Correlations between components in Vector Space Decomposition model and components in double- dq model, which allow better understanding of the fictitious x - y currents, are shown in Chapter 3.
- 2) The performance comparisons of PI controllers in difference reference frame for x - y current control are detailed in Chapter 3.
- 3) The use of resonant controller in anti-synchronous frame for compensating dead-time effect in six-phase machine is demonstrated in Chapter 3.
- 4) The use of x - y current controller to achieve dc-link voltage balancing in the topology with series-connected machine-side converters is presented in Chapter 4.
- 5) Analysis of the effect of an open-circuit fault on the performance of current control using PI controllers is reported in Chapter 5.
- 6) Quantitative comparisons of performance for different modes of post-fault operation for asymmetrical six-phase induction machine configured with two and single isolated neutral are described in Chapter 5.

The research conducted within the scope of the thesis has led to the production of four IEEE conference papers and two IEEE Transactions papers. The relationship between outputs and the chapters of this thesis is as follows. The most important results

of Chapter 3 have been published in (Che *et al.*, 2012c) and (Che *et al.*, 2013c). The considerations of Chapter 4 have been made available in (Che *et al.*, 2012a), (Che *et al.*, 2012b) and (Che *et al.*, 2013b). Finally, output (Che *et al.*, 2013a) relates to the content of Chapter 5.

1.4. Thesis Structure

This thesis is organised in the following manner: Chapter 2 provides a detailed literature review in the areas associated with the topics covered in the thesis, with an emphasis placed on the recent work related to asymmetrical six-phase drive and generation systems. Chapters 3, 4 and 5 subsequently cover the three main topics of this thesis, identified in section 1.1. Chapter 3 deals with the current control methods, with an emphasis on the control of the current components in the non-flux/torque producing plane within the framework of the rotor flux oriented control. Chapter 4 analyses the operation with series-connected machine-side converters, with a focus on the means for balancing the capacitor voltages in the two series connected dc-side capacitors; an entirely new use of the stator current components in the non-flux/torque producing plane is developed in this Chapter. Finally, Chapter 5 develops strategies for post-fault control, with an emphasis on the comparison of two neutral points and single neutral point configurations in post-fault operation.

Each chapter provides a complete discussion encompassing theoretical analysis, simulation and/or experimental studies for the respective topic. Finally, conclusions of the completed research work and suggestions for future work are given in Chapter 6.

Beside the main chapters, four appendices have been included in this thesis. Appendix A provides detail information on the simulation model developed in Matlab/Simulink environment for performing simulation studies presented in the thesis.

The experimental setup used in this research project is then described in Appendix B. Appendix C contains derivations of machine equations for faulted machine, which is useful in understanding the analysis presented in Chapter 5. The last appendix, i.e. Appendix D, shows the list of publications resulted from this thesis.

Chapter 2

LITERATURE REVIEW

2.1. Introduction

Multiphase machines (machines with more than three phases) and drives have been a subject of extensive research scrutiny during the past few decades, and numerous fundamental aspects have been explored in detail and reported in the literature. Comprehensive reviews of the research in multiphase machine and drive areas, covering modelling, control and applications, have been presented in recent past (Levi *et al.*, 2007a; Levi, 2008). Using these fundamental findings, research on multiphase machines and drives has continued to prosper in the last few years, with a tendency of moving towards more complex issues. For instance, studies of pulse-width modulation (PWM) techniques have moved from the case with n -leg two-level voltage source converter (VSC) and star-connected stator windings, to more complex multi-level VSCs (Dodervic *et al.*, 2013a; Dodervic *et al.*, 2013b) and open-end winding configurations (Jones *et al.*, 2012; Levi *et al.*, 2012; Bodo *et al.*, 2013). Control of multiphase machines using more sophisticated algorithms, such as predictive control, is also an active topic of research in recent years (Barrero *et al.*, 2009; Gregor *et al.*, 2010; Barrero *et al.*, 2011; Duran *et al.*, 2012; Riveros *et al.*, 2013; Lim *et al.*, 2013).

In this chapter, a literature review of the latest research developments in the field of multiphase machines and drives is reported. To allow a better correlation between the

surveyed literature and this thesis, the remainder of this chapter is divided into three main sections. Section 2.2 reviews the current control methods for multiphase drive systems, with a focus on control based on the vector space decomposition (VSD) model. Section 2.3 gives an account of the operation of multiphase machines based on various alternative converter topologies, while Section 2.4 summarises current knowledge in the area of the post-fault control of multiphase machines.

2.2. Current Control Methods

2.2.1. Machine models

Control of multiphase machines is usually an extension of the control principles used for the three-phase machines. As with a three-phase machine, the control of a multiphase machine is based on a suitable machine model. For the particular case of a six-phase machine, two different models have been commonly used for control development, i.e. the double- dq model (Lipo, 1980) and the VSD model (Zhao and Lipo, 1995).

For the double- dq model, two separate decoupling (Clarke) three-phase transformations are first applied onto the two sets of three-phase phase variables. Taking stator currents as an example, this results in two pairs of α - β currents ($i_{\alpha 1} - i_{\beta 1}$ and $i_{\alpha 2} - i_{\beta 2}$) in the stationary reference frame. These currents are then subjected to a rotational (Park) transformation, to yield corresponding two pairs of d - q currents ($i_{d1} - i_{q1}$ and $i_{d2} - i_{q2}$). With the d -axis aligned to the rotor flux, machine flux is controlled by regulating i_{d1} and i_{d2} , while the machine torque is controlled by regulating i_{q1} and i_{q2} . This is analogous to the rotor flux oriented control (RFOC) in three-phase machines, except that two sets of d - q current controllers are needed instead of just one.

Successful implementation of current control based on this approach has been reported in (Singh *et al.*, 2005). An extension of this model to a nine-phase machine was demonstrated in (Jung *et al.*, 2012) for ultra-high speed elevator application, by using three instead of two decoupling transformations and three pairs of $d-q$ current controllers. However, one obvious disadvantage of this model is that its applicability is restricted to multiphase machines with multiple three-phase windings.

An alternative to the double- dq model is the VSD model developed in (Zhao and Lipo, 1995). The VSD model serves as an important tool for the analysis of multiphase machines, and subsequently the development of current control methods. Using the VSD approach, an n -phase machine can be represented using $n/2$ (or $(n-1)/2$ for machines with an odd number of phases) orthogonal subspaces, which include one $\alpha\text{-}\beta$ subspace and several $x\text{-}y$ subspaces, and the zero-sequence components. For a machine with sinusoidal magneto-motive force (MMF) distribution, only the $\alpha\text{-}\beta$ components contribute to useful electro-mechanical energy conversion, while $x\text{-}y$ and zero-sequence components only produce losses (Levi *et al.*, 2007a). Based on the VSD approach, the $\alpha\text{-}\beta$ machine equations of a multiphase machine are identical to those of a three-phase machine, so that direct implementation of the standard three-phase vector control becomes possible. Nevertheless, due to the presence of additional loss-producing components, the corresponding currents need to be controlled as well for improved system performance.

Compared to the double- dq model, the VSD model is more general and is applicable to multiphase machines of any phase number. The separation of flux and torque producing components ($\alpha\text{-}\beta$) from the loss producing components ($x\text{-}y$ and zero-sequence) in VSD model provides an insightful tool for the development of space vector pulse-width modulation (SVPWM) for multiphase machines (Zhao and Lipo, 1995; Hadiouche *et al.*, 2006; Dujic *et al.*, 2008), which cannot be done easily using the

double- dq model. In terms of control, it was concluded in (Bojoi *et al.*, 2003c) that similar dynamic performance can be obtained regardless of the type of the model chosen. Nevertheless, it was also noted in (Bojoi *et al.*, 2003c) that the vector control of the six-phase machine using VSD approach requires voltage decoupling terms that are less complicated than in the double- dq approach. Due to the advantages of the VSD model, such as clear information of the harmonic mapping into different planes, most of the recent works on multiphase machines, including this thesis, are based on this model.

It should be noted that although both VSD and double- dq model are essentially applicable to the same machine, the machine parameters for each model are different. In (Bojoi, 2002) it was shown that if the mutual leakage inductance between the two three-phase windings is considered to be negligible, a simple and direct correlation between parameters of the two models exists. The stator resistance and stator leakage inductance are equal for the two models, while the mutual inductance, rotor leakage inductance and rotor resistance of the VSD model are twice that in the double- dq model. Several methods for estimating the machine parameters based on the VSD model have been reported in (Jacobina *et al.*, 2002; Riveros *et al.*, 2012; Yepes *et al.*, 2012).

2.2.2. Current Controllers

The use of VSD model greatly simplifies the control of a multiphase machine, since the resultant $\alpha\text{-}\beta$ machine equations are identical to those of a conventional three-phase machine. Hence, control of stationary reference frame $\alpha\text{-}\beta$ currents (or their synchronous reference frame counterparts, i.e. $d\text{-}q$ currents) is the same as that of a three-phase machine. For rotor flux oriented control, control is usually done in the synchronous ($d\text{-}q$) reference frame using PI controllers (Levi *et al.*, 2007a), although current regulation in the stationary reference frame has also been demonstrated (Bojoi *et al.*, 2006).

It should be emphasised here that the statement above is only valid for PWM-based control methods and does not hold true for other control methods, such as look-up-table-based direct torque control (LUT-DTC) or model predictive control (MPC). This is because the LUT-DPC and MPC operate by analysing the effect of each switching state of the converter on the controlled variables (current, torque, flux etc.). Since the switching states in a three-phase converter are different from those of a multiphase converter, implementation of these control methods in multiphase motor drives requires substantial modifications, compared to the three-phase drive control. Although successful implementations of LUT-DTC (Bojoi *et al.*, 2005) and MPC (Barrero *et al.*, 2009; Gregor *et al.*, 2010; Barrero *et al.*, 2011; Duran *et al.*, 2012; Riveros *et al.*, 2013; Lim *et al.*, 2013) have been reported, they are beyond the scope of this thesis and hence not discussed further.

As mentioned earlier, due to the additional degrees of freedom in a multiphase machine, controlling just the α - β currents is inadequate to ensure high performance operation. The loss-producing x - y and zero-sequence currents need to be regulated as well. To simplify the control, zero-sequence currents are usually eliminated by choosing a suitable stator winding configuration. For machines with odd number of phases, this is done by having star-connected winding with an isolated neutral point. For the case of machines with multiple three-phase windings, zero-sequence currents can be eliminated by configuring the machine windings into multiple three-phase windings, each with an isolated neutral point. Under such circumstances, additional control of the zero-sequence currents can be avoided.

Unlike the zero-sequence currents, x - y currents cannot be eliminated by winding configuration and hence have to be controlled. Under normal conditions, the x - y currents are regulated to zero to reduce stator losses and improve system efficiency. Nevertheless, they can also be utilised for other purposes, such as to provide torque

enhancement in concentrated winding machines (Lyra and Lipo, 2002; Abdel-Khalik *et al.*, 2010), to allow independent control of motors in multi-machine drives with a single multiphase supply source (Levi *et al.*, 2004a; Levi *et al.*, 2004b; Jones *et al.*, 2005, Levi *et al.*, 2005; Levi *et al.*, 2006; Levi *et al.*, 2007b) or to enable fault-tolerant operation (Locment *et al.*, 2008; Tani *et al.*, 2012; Zarri *et al.*, 2013).

From the surveyed literature, it can be concluded that control of x - y currents has only been investigated to some extent. Several different x - y current control methods have been proposed in the past. In (Vukosavic *et al.*, 2005), the x - y and zero-sequence currents were minimised by simply setting the corresponding voltage references to zero, without using any additional controllers. While this was found to be a simple yet adequate approach in the case of (Vukosavic *et al.*, 2005), (Bojoi *et al.*, 2003a) showed that in the presence of machine/converter asymmetry, lack of x - y current controllers can cause the flow of x - y currents, which are a consequence of imbalance in phase currents. Subsequently, additional controllers have to be utilised to control these loss-producing currents. In (Jones *et al.*, 2009), the authors suggested the use of PI controllers in the synchronous reference frame to control x - y currents in a five-phase induction machine. In (Bojoi *et al.*, 2006), resonant controllers were used for controlling the x - y currents in an asymmetrical six-phase induction machine. In (Tani *et al.*, 2012; Zarri *et al.*, 2013), dual PI controllers were used for regulating x - y currents, but for a very specific reason of accommodating fault-tolerant control (Tani *et al.*, 2012) and detecting high impedance connections (Zarri *et al.*, 2013). Even though the proposed controllers were shown to yield satisfactory performance, a systematic comparison between the different control methods for x - y currents is not available yet. Hence, this is provided in this thesis, where performances of x - y current control using PI controllers in different reference frames are compared.

2.3. Operation with Alternative Converter Topologies

From the literature, it is found that the most widely used converter topology for an n -phase machine is an n -leg voltage source converter (VSC) feeding an n -phase machine with a star-connected stator winding, as illustrated in Fig. 2.1. For the converter, a two-level VSC can be considered as the standard solution. For the case of a permanent magnet synchronous generator, where bidirectional power flow is not necessary, the converter can be an n -leg rectifier. These are, however, not the only options available, and some alternative topologies have been proposed.

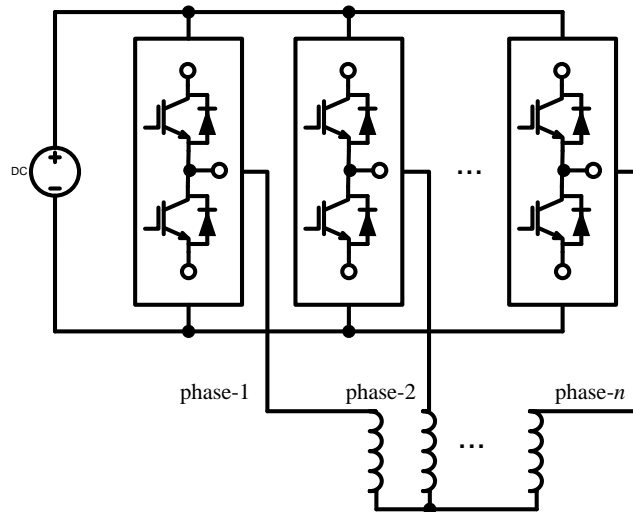


Fig. 2.1. Conventional parallel-connected n -leg two-level VSC feeding an n -phase machine with star-connected stator windings (only stator phase windings are shown).

In (Andersen and Birk, 2007; Birk and Andersen, 2007), an eighteen-phase permanent magnet generator was used for wind energy conversion as shown in Fig. 2.2(a). Instead of having a single dc-link with all eighteen legs of the VSC connected in parallel, the proposed system utilised six back-to-back three-phase VSCs giving a modular structure to the system. This allows some of the back-to-back VSC modules to be switched off at lower-than-rated power, giving rise to overall improved system efficiency. In (Zhang *et al.*, 2009), operation of a twelve-phase brushless dc generator with a twelve-phase half-wave rectifier (Fig. 2.2(b)) for low voltage dc system on an aircraft is investigated. The study compares the twelve-phase system with a six-phase system with a six-phase full-wave rectifier. Results show that, for the same number of

switches, the twelve-phase system is superior due to better efficiency and reduced system size.

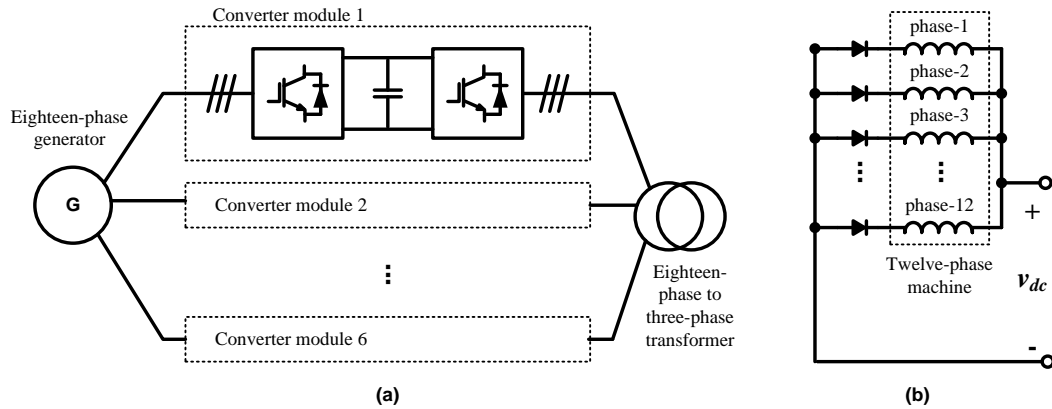


Fig. 2.2. (a) Parallel converters for eighteen-phase machine discussed in (Andersen and Birk, 2007; Birk and Andersen, 2007), and (b) Half-wave rectifier for twelve-phase machine discussed in (Zhang *et al.*, 2009).

Instead of a parallel connection, the machine-side converters can also be connected in series. For machines with multiple three-phase windings, each winding can be connected to a separate three-phase converter. These three-phase converters can then be cascaded in series, to yield an elevated dc-link. A study of series connection of diode rectifiers for a twelve-phase permanent magnet synchronous generator was reported in (Di Gerlando *et al.*, 2012). Apart from diode-based rectifiers, VSC-based machine-side converters with series connection have also been explored. One such system was demonstrated in (Duran *et al.*, 2011), using a six-phase permanent magnet generator connected to two three-phase VSCs. In the studied system, the two three-phase VSCs were connected in series, with the two dc links cascaded to give a higher overall dc-link voltage. The main benefit is to allow integration of a low-voltage generator with a high-voltage dc system. A similar concept, which utilises a twelve-phase permanent magnet generator with four cascaded machine-side converters, is investigated in (Xiang-Jun *et al.*, 2012). Instead of using two-level VSCs, the studied system uses Vienna rectifiers as the machine-side converters. In (Gjerde and Undeland, 2012), the authors suggested a wind energy conversion system using a twenty-seven (9×3) phase generator with nine modular three-phase VSCs connected in series. The idea is further extended in (Gjerde

et al., 2012; Olsen *et al.*, 2012), with more discussion on the aspects of the machine design, converter structure and control.

Investigation of an open-end winding topology for multiphase machines has also gained some popularity recently, since it provides several advantages, such as better (multilevel) voltage output, improved dc-voltage utilisation and higher fault tolerance (Bodo *et al.*, 2013), compared to a single-sided two-level VSC supply. For multiphase motor drive applications, open-end winding structure was studied mainly because of its fault-tolerance feature (Grandi *et al.*, 2011, Grandi *et al.*, 2012; Villani *et al.*, 2012). In (Spooner *et al.*, 2005; Ng *et al.*, 2008; Parker *et al.*, 2011; Yuan *et al.*, 2012; Parker *et al.*, 2013), an interesting combination of the open-end winding concept and the series-connected converter concept was demonstrated. The machine windings are fed with modular ac-dc-ac converters in an open-end winding manner, which are then cascaded in series to form a cascaded H-bridge multilevel converter, as seen in Fig. 2.3. Such a topology allows the direct interfacing of the generator with a three-phase grid without the need for a bulky and expensive step-up transformer.

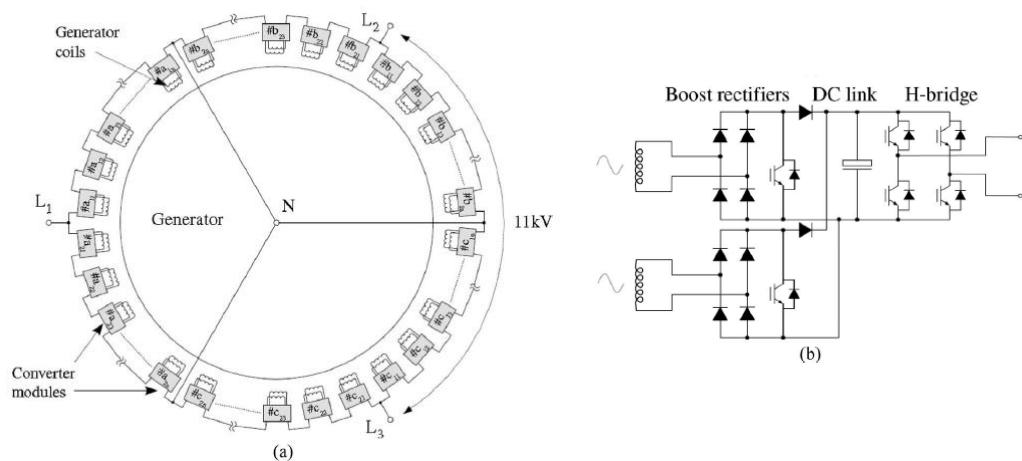


Fig. 2.3. (a) Overall structure for a three-phase grid converter, and (b) individual converter module of the power electronics converter presented in (Parker *et al.*, 2011).

(Bu *et al.*, 2012a; Bu *et al.*, 2012b) demonstrated a special application of a six-phase induction machine as an integrated ac and dc generation system (Fig. 2.4). In the proposed system, the windings are separated into two sets of three-phase windings,

which are called the control winding and the power winding, respectively. The control winding is fed with a three-phase VSC and is responsible for both providing the excitation flux and the dc power. The power winding, on the other hand, provides the ac power and is directly connected to ac loads.

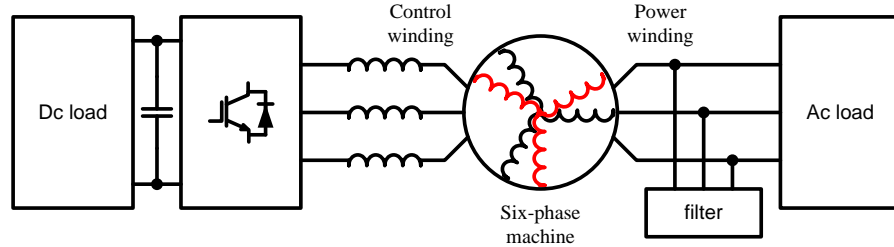


Fig. 2.4. Integrated ac and dc generation system discussed in (Bu *et al.*, 2012a; Bu *et al.*, 2012b).

Based on the surveyed literature, it is found that the series-connected converter topology suggested in (Duran *et al.*, 2011) is a promising candidate for further research. The main advantage of the topology is its simplicity, since a standard six-phase machine and standard three-phase VSCs are utilised. Due to the series-connection of the VSCs, it is expected that additional control will be required for balancing the dc-link voltages, However, this was not covered in (Duran *et al.*, 2011). Thus, the operation of the series-connection topology is investigated in this thesis, to understand the potential merits and demerits of the structure. A dc-link voltage balancing control is proposed to provide effective dc-link voltage regulation by using the additional degrees of freedom provided by the x - y currents.

2.4. Post-fault Control

Among the many merits of a multiphase machine, fault tolerance is without any doubt one of the most important features. For a three-phase machine controlled with a three-leg VSC, the machine loses controllability in an event of fault unless a special converter topology is used (Welchko *et al.*, 2004; Mendes and Cardoso, 2006). On the other hand, an n -phase machine, fed with an n -leg VSC, can continue to operate after

losing up to $(n-3)$ phases, provided a suitable post-fault control is utilised (Levi *et al.*, 2007a). It is found that, with a few exceptions, such as (Apsley and Williamson, 2006; Miranda *et al.*, 2007; Alberti and Bianchi, 2012; Aboelhassan *et al.*, 2013), most studies of post-fault control only address an open-circuit fault, where the connection between the converter and the machine is lost. This can be due to mechanical failure of a terminal connector, internal winding rupture or electrical failure of a converter leg (Tani *et al.*, 2012). By applying proper control, the effect of open-circuit fault can be compensated and the faulted machine can continue to operate. On the other hand, the effect of short-circuit fault is closely related to the design rather than to the control of the machine. By using a suitable type of the machine, such as concentrated/modular winding machines (Baudart *et al.*, 2012) and flux-switching machines (Aboelhassan *et al.*, 2013), or by proper arrangement of the machine windings (Alberti and Bianchi, 2012), better short-circuit fault tolerance can be obtained. Thus, the short-circuit fault mitigation is more of a machine design problem than a control problem. Since the focus of this thesis is on control of the six-phase machine, further discussions are related to an open-circuit fault. Consequently, a “fault” in this thesis will always refer to an open-circuit fault, unless stated otherwise.

In (Levi *et al.*, 2007a) it is emphasised that the simplest form of fault-tolerant operation can be obtained with multiphase machines that have m sets of k -phase stator windings, such as six-phase ($m=2, k=3$), nine-phase ($m=3, k=3$), fifteen-phase ($m=5, k=3$ or $m=3, k=5$), eighteen-phase ($m=6, k=3$) machines, etc. In an event of fault, the whole k -phase winding containing the fault can be disconnected, and the machine can continue to operate with $(m-1)$ sets of k -phase windings. One example of the application of such an approach was recently demonstrated in (Jung *et al.*, 2012), for a nine-phase permanent magnet synchronous motor used in ultrahigh-speed elevator. However, taking out the whole k -phase winding results in significant reduction of the

achievable power, since several healthy phases are taken out in the process. Moreover, this solution is only valid for multiphase machines with $m \times k$ winding structures, and cannot be applied to multiphase machines without such winding configuration.

A more general approach for post-fault control in an n -phase machine is to only take out the faulted phase(s), and continue operating with all the remaining healthy phases. In (Shamsi-Nejad *et al.*, 2008), the authors showed that during the single open-circuit fault, instead of taking out one of the two three-phase windings in a six-phase permanent magnet machine, higher efficiency can be obtained if the five remaining windings are continued to be utilised. However, the complexity of such control increases considerably and the dynamic performance of the control proposed in (Shamsi-Nejad *et al.*, 2008) was poor. Nevertheless, numerous studies have been dedicated to developing post-fault control strategies for multiphase machines, where high performance operation has been reported.

There are two main objectives in the development of a post-fault control for a multiphase drive system:

- 1) To derive the post-fault current references according to a specific criterion, such as minimum stator losses, equal phase currents, minimum torque ripple etc.
- 2) To design suitable controllers that are capable of regulating the currents to their references during post-fault operation.

2.4.1. Derivation of Post-fault Current References

For the first objective above, the fundamental idea is to find a set of current equations that define the desired post-fault characteristic of the machine, and solve them to obtain the current references. Various approaches have been proposed in the past for this purpose.

The most direct approach is to derive the current references in terms of the phase currents. In (Fu and Lipo, 1995), the current equations for maintaining a smooth rotating magneto-motive force (MMF) in the machine are considered, together with several auxiliary equations for equalising phase current amplitude and zero/non-zero neutral point current. A similar MMF-based approach, is adopted in (Parsa and Toliyat, 2007) for up to two lost phases in a five-phase permanent magnet machine. In (Dwari and Parsa, 2008; Dwari and Parsa, 2011; Mohammadpour and Parsa, 2013) the post-fault current references are derived based on power equations, with the effect of the third harmonic components taken into consideration.

In the control of a multiphase machine, it is more common to use the decoupled current components (α - β , x - y and zero-sequence components for the case of VSD approach) than the phase currents as the control variables. For this reason, some authors developed post-fault current references in the form of the decoupled components.

One particular group of works, such as those presented in (Zhao and Lipo, 1995a; Zhao and Lipo, 1995b; Ryu *et al.*, 2006; Kianinezhad *et al.*, 2008), suggest the use of a reduced order decoupling transformation for deriving the post-fault current references. It was proposed to replace the original n -order decoupling transformation by a new reduced order decoupling transformation to reflect the loss of degree(s) of freedom. The overall concept of this approach is detailed in (Zhao and Lipo, 1995a; Zhao and Lipo, 1995b), where a 5×5 decoupling matrix is proposed to replace the original 6×6 matrix for an asymmetrical six-phase induction machine with a single open-circuit fault. In this approach, (Zhao and Lipo, 1995a; Zhao and Lipo, 1995b) retained the α - β rows of the original decoupling transformation matrix, which still represent the flux and torque related components, but with the terms associated with the lost phase removed. The remaining rows of the transformation are then re-derived based on the known orthogonal properties between the matrix rows. Based on the new reduced order

transformation, a whole new set of post-fault machine equations is derived and new control is structured around it. One important conclusion drawn from this approach is that the machine α - β equations retain the same form as in the healthy case, with modifications only related to the mutual inductance. Based on this finding, the same field-oriented control strategy can be applied for post-fault operation, by modifying the value of the mutual inductance and the rotational transformation. Results showed that with this modification, flux and torque of the machine can still be regulated by the d - q currents, respectively. The same concept was used in (Kianinezhad *et al.*, 2008) for the case of a symmetrical six-phase machine, with analysis done in the α - β plane instead of the d - q plane. The changes in the mutual inductance for different combinations of faulted phases are summarised, and the comparison with two other methods is given. In the paper, the authors showed that torque oscillations during post-fault operation can be minimised if the amplitudes of the α - β currents are set to a fixed ratio, whose value depends on the fault. It is worth noting that this is essentially the same concept as (Zhao and Lipo, 1996a; Zhao and Lipo, 1996b), if the analysis is extended to d - q plane using the modified rotational transformation.

Although post-fault control derived based on the reduced order transformation was shown to give good performance, significant alterations of the control structure become necessary. Some researchers hence searched for post-fault control methods that involve minimal reconfiguration of the control structure. In (Baudart *et al.*, 2012) one such method was proposed, where a general approach applicable to an n -phase machine with symmetrical windings was described. By introducing an additional matrix for defining the condition (healthy or faulted) of each phase, a general control structure was introduced to allow transition from healthy to post-fault operation with minimal reconfiguration. Nevertheless, the method involves additional matrix manipulations and is more complex.

One interesting post-fault control strategy was presented in (Locment *et al.*, 2007; Apsley, 2010; Tani *et al.*, 2012) for several machines with different number of phases. Instead of using reduced order decoupling transformation, the same full order transformation (as in the healthy case) is retained even for post-fault operation. Since the transformation matrix is not changed, the post-fault control structure has exactly the same form as in the healthy case. Transition from healthy to post-fault operation only involves change of the current references.

2.4.2. Post-fault Current Control

After obtaining the post-fault current references, it is necessary to have a good current control method, which is capable of regulating the currents to their references. Compared to the derivation of the post-fault current references, this issue is covered less in the literature. Based on the literature which provided sufficient information on the current controller used, it was found that the most frequently discussed current control methods are the hysteresis-type controller (Zhao and Lipo, 1996a; Zhao and Lipo, 1996b; Parsa and Toliyat, 2007; Dwari and Parsa, 2008; Dwari and Parsa, 2011; Mohammadpour and Parsa, 2013) and PI controller with pulse-width modulator (Ryu *et al.*, 2006; Locment *et al.*, 2008; Baudart *et al.*, 2012; Tani *et al.*, 2012), although more complex control methods, such as model predictive control (Guzman *et al.*, 2011), fuzzy control and sliding mode control (Fnaiech *et al.*, 2010), have also been proposed.

Compared with PI controllers, the high bandwidth of hysteresis-type controller provides effective and fast regulation of the machine currents, especially during faulted condition. Nevertheless, the high sampling requirement and variable switching frequency associated with the hysteresis based switching are seen as serious setbacks, especially for high power applications where multiphase machines are of particular importance (Ryu *et al.*, 2006). For PI controllers with a pulse-width modulator, the performance of the current regulation can be degraded by the limited bandwidth of the

controller. In (Ryu *et al.*, 2006), the authors showed that the reduced order decoupling transformation introduces additional disturbance to the controller, which requires special compensation using feedforward approach. In (Jacobina *et al.*, 2004), the authors emphasised that the actual phase voltage of a faulted machine is not solely dependent on the converter leg voltage, but on the voltage of the faulted phase as well. This idea is revisited in (Guzman *et al.*, 2011). Nevertheless, a detailed study of this issue and the effect on linear (PI) controller-based post-fault control are not available in the literature. This is covered here in Chapter 5 of this thesis.

2.4.3. Other Winding Configurations

So far, discussion of the post-fault control of multiphase machines has been predominantly related to the typical machine-converter topology, i.e. an n -phase star-connected machine fed from an n -leg VSC. The studies presented in this thesis are restricted to this type of topology. Nevertheless, it is worth noting that research on post-fault operation of machines with other winding configurations and converter topologies can be found in the literature. In (Sayed-Ahmed and Demerdash, 2012), tolerant operation for three-phase machine with delta winding was studied. In (Abdel-Khalik *et al.*, 2013), the post-fault operation of a five-phase machine configured with both star and pentagon stator winding connections was investigated and compared. In (Mohammadpour and Parsa, 2013), a general analysis of post-fault operation of a five-phase machine with pentagon and pentacle connected stator windings has been presented. With regard to the converters, special converters for achieving better fault tolerance have been reported in (Parker *et al.*, 2011; Ruba *et al.*, 2012; Wang *et al.*, 2012; Parker *et al.*, 2013).

2.5. Summary

From the surveyed literature, it can be concluded that there still exist some areas in the multiphase machine and drive research, i.e. on x - y current control methods, operation with series-connected machine-side converters and post-fault operation, which are not completely covered and hence provide an opportunity for improvement. With a focus on asymmetrical six-phase induction machine, these three interesting topics on multiphase machine control are investigated and reported in the subsequent chapters.

Chapter 3

CURRENT CONTROL METHODS

3.1. Introduction

As pointed out in Chapter 2, current control of a multiphase machine in the torque and flux producing α - β plane has been thoroughly investigated and standard control methods used for three-phase machines have typically been considered. However, the control of the x - y currents, which are not involved in useful electro-mechanical energy conversion, has been considered to a lesser extent. Here, the current control methods for x - y currents in an asymmetrical six-phase induction machine are explored. Two important aspects which are related to the x - y currents, i.e. compensation of machine/converter asymmetry and dead-time effect, are addressed in this chapter.

The chapter is organised as follows. Section 3.2 starts by first establishing the physical interpretation of the x - y currents, based on the VSD and double- dq machine models. This interpretation is useful in determining the suitable frame of control for the x - y currents. Section 3.3 then discusses the two roles of the x - y current controllers, i.e. compensation of asymmetry and dead-time effect. Subsequently, experimental results are given in Section 3.4, where the performance of several different types of PI-based x - y current controllers is compared, in order to validate the analysis of Section 3.3. Finally, conclusions of the work are summarised in Section 3.5.

3.2. Interpretation of the x - y Currents Using VSD and Double- dq Modelling Approaches

Based on the double- dq model (Lipo, 1980), the two three-phase windings in a six-phase machine are treated separately and two three-phase different decoupling (Clarke) transformations are applied to the phase variables for each three-phase winding. The α -axis of the stationary reference frame is aligned with phase- $a1$ of the stator winding, as indicated in Fig. 3.1. This transforms the six-phase variables into two sets of stationary reference frame variables, denoted as $\alpha1$ - $\beta1$ and $\alpha2$ - $\beta2$ components, for windings 1 and 2, respectively:

$$[\lambda_{\alpha1} \ \lambda_{\beta1}]^T = [T_1][\lambda_{a1} \ \lambda_{b1} \ \lambda_{c1}]^T \quad (3.1)$$

$$[\lambda_{\alpha2} \ \lambda_{\beta2}]^T = [T_2][\lambda_{a2} \ \lambda_{b2} \ \lambda_{c2}]^T \quad (3.2)$$

Symbol λ represents arbitrary machine variables (voltage, current or flux). The spatial 30° displacement between the two windings is accounted for in the decoupling transformation.

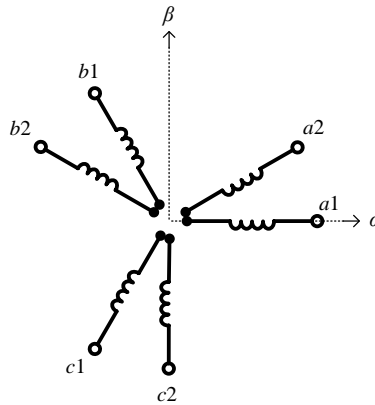


Fig. 3.1. Position of the stationary reference frame (α - β) with respect to the stator phase windings.

For an asymmetrical six-phase machine, the power invariant decoupling transformation for windings 1 and 2, respectively, is given with:

$$[T_1] = \sqrt{\frac{2}{3}} \begin{bmatrix} 1 & -\frac{1}{2} & -\frac{1}{2} \\ 0 & \frac{\sqrt{3}}{2} & -\frac{\sqrt{3}}{2} \end{bmatrix} \quad (3.3)$$

$$[T_2] = \sqrt{\frac{2}{3}} \begin{bmatrix} \frac{\sqrt{3}}{2} & -\frac{\sqrt{3}}{2} & 0 \\ \frac{1}{2} & \frac{1}{2} & -1 \\ \frac{1}{2} & \frac{1}{2} & -1 \end{bmatrix} \quad (3.4)$$

The equivalent circuit of a six-phase induction machine, taking into account the presence of mutual leakage inductance L_{lm} , is shown in Fig. 3.2.

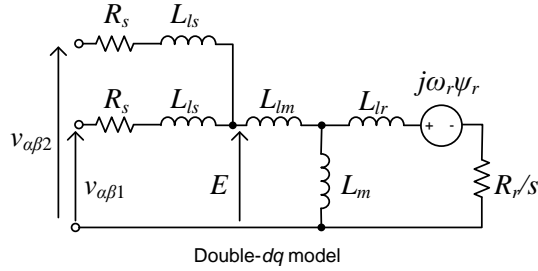


Fig. 3.2. Equivalent circuit for a six-phase induction machine based on double- dq model.

On the other hand, the relationship between VSD variables and phase variables for an asymmetrical six-phase machine with isolated neutrals is given with

$$[\lambda_\alpha \ \lambda_\beta \ \lambda_x \ \lambda_y \ \lambda_{0+} \ \lambda_{0-}]^T = [T][\lambda_{a1} \ \lambda_{b1} \ \lambda_{c1} \ \lambda_{a2} \ \lambda_{b2} \ \lambda_{c2}]^T \quad (3.5)$$

where $[T]$ is the decoupling transformation according to VSD approach:

$$[T] = \frac{1}{\sqrt{3}} \begin{bmatrix} 1 & -\frac{1}{2} & -\frac{1}{2} & \frac{\sqrt{3}}{2} & -\frac{\sqrt{3}}{2} & 0 \\ 0 & \frac{\sqrt{3}}{2} & -\frac{\sqrt{3}}{2} & \frac{1}{2} & \frac{1}{2} & -1 \\ 1 & -\frac{1}{2} & -\frac{1}{2} & -\frac{\sqrt{3}}{2} & \frac{\sqrt{3}}{2} & 0 \\ 0 & -\frac{\sqrt{3}}{2} & \frac{\sqrt{3}}{2} & \frac{1}{2} & \frac{1}{2} & -1 \\ 1 & 1 & 1 & 0 & 0 & 0 \\ 0 & 0 & 0 & 1 & 1 & 1 \end{bmatrix} \quad (3.6)$$

The equivalent circuit of a six-phase induction machine based on the VSD model is shown in Fig. 3.2. The dynamic model for the VSD model can be found in section 4.2.2.

Based on the VSD model, the machine is decoupled into three orthogonal subspaces, denoted as the α - β , x - y and zero-sequence (0+0-) subspaces. For machine with distributed stator windings, stator-rotor coupling only exists in the α - β subspace. Hence, only the α - β components are responsible for useful electro-mechanical energy conversion. The remaining two subspaces can be characterised with an RL circuit, and produce only losses. Note that the leakage inductance in the x - y and the zero sequence

planes is identical to that of the α - β plane. This is due to the assumption that the mutual leakage inductance of the windings is negligible, and thus can only be valid for certain types of the winding structure as explained in (Hadiouche *et al.*, 2004).

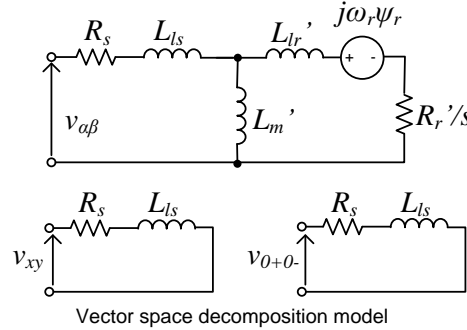


Fig. 3.3. Equivalent circuit for a six-phase induction machine based on VSD model.

As highlighted in Chapter 2, the VSD approach offers many benefits over the double- dq approach, which makes the former a more popular choice among researchers working in the field of multiphase machines. Nevertheless, despite the various advantages of the VSD model, the variables are more difficult to interpret physically, unlike in the double- dq model where $\alpha 1$ - $\beta 1$ variables are clearly related to the winding 1 and $\alpha 2$ - $\beta 2$ variables to the winding 2 of the machine. It is therefore desirable to provide a better physical interpretation of the VSD model variables by relating them with variables in the double- dq model. This can be done by simply comparing the decoupling transformation matrices for the two methods.

By comparing equations (3.3) and (3.4) with (3.6), it can be seen that α - β components in the VSD model are proportional to the sum of the $\alpha 1$ -, $\alpha 2$ - and $\beta 1$ -, $\beta 2$ - components of the double- dq model. On the other hand, x -component and y -component are proportional to the difference between $\alpha 1$ -, $\alpha 2$ - and $\beta 1$ -, $\beta 2$ - components, respectively, with the signs for the x - and y - components inverted. As will be shown later, this opposite sign influences the rotational direction of the x - y current phasor caused by the machine/converter asymmetry. The relationship is given with:

$$\begin{aligned}
\lambda_\alpha &= \sqrt{\frac{1}{2}}(\lambda_{\alpha 1} + \lambda_{\alpha 2}) = \sqrt{\frac{1}{2}}\Sigma\lambda_{\alpha 12} \\
\lambda_\beta &= \sqrt{\frac{1}{2}}(\lambda_{\beta 1} + \lambda_{\beta 2}) = \sqrt{\frac{1}{2}}\Sigma\lambda_{\beta 12} \\
\lambda_x &= \sqrt{\frac{1}{2}}(\lambda_{\alpha 1} - \lambda_{\alpha 2}) = \sqrt{\frac{1}{2}}\Delta\lambda_{\alpha 12} \\
\lambda_y &= \sqrt{\frac{1}{2}}(-\lambda_{\beta 1} + \lambda_{\beta 2}) = -\sqrt{\frac{1}{2}}\Delta\lambda_{\beta 12}
\end{aligned} \tag{3.7}$$

It is useful to express the α - β and x - y components in the form of space vectors:

$$\begin{aligned}
\bar{\Lambda}_{\alpha\beta} &= \lambda_\alpha + j\lambda_\beta \\
\bar{\Lambda}_{xy} &= \lambda_x + j\lambda_y
\end{aligned} \tag{3.8}$$

3.3. X-y Current Control for Six-phase Induction Machine

3.3.1. Asymmetry Compensation

The general structure of the current controllers within the rotor flux oriented control scheme, considered further on and based on VSD approach, is shown in Fig. 3.4. Here x - y currents are not rotationally transformed and are shown as being controlled in the stationary reference frame.

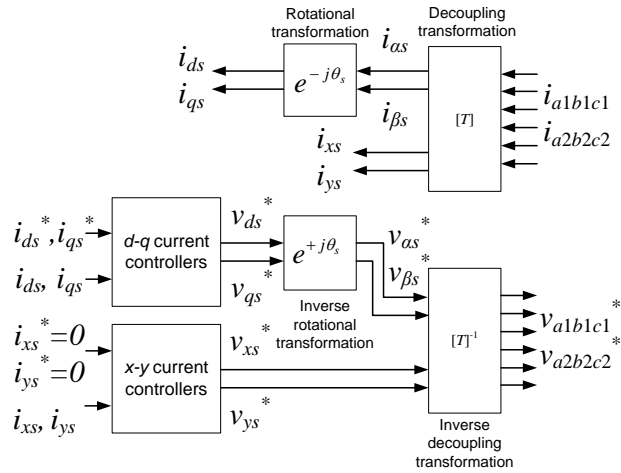


Fig. 3.4. General structure of the current controllers for a six-phase induction machine (rotational transformation is only applied to α - β components).

As shown in (Bojoi *et al.*, 2003a), asymmetry in the machine windings or the converter can cause large current distortion in the six-phase machine. Pulse width modulation can also cause current distortion (Bojoi *et al.*, 2002), but this effect is marginal if the proper PWM technique is chosen. With the effect from PWM minimised, the machine/converter asymmetry leads to the current flow in the x - y plane, so proper x -

x - y current control has to be used to mitigate the problem. Several x - y current control strategies have been proposed as a possible solution, including the use of resonant controllers (Bojoi *et al.*, 2006) and PI controllers (Jones *et al.*, 2009). In particular, the PI controller is the favourable choice for x - y current control, due to its simple structure and well-understood characteristics.

It is well-known that the PI controller is capable of providing zero steady state error regulation for dc-component because of its high open loop gain at zero frequency. However, for components that are not dc in nature, performance of a PI controller deteriorates with increasing frequency. As a result, the reference frame has a decisive effect on the performance of the PI controller.

It has been shown in (Jones *et al.*, 2009) that x - y currents, produced by asymmetry in a five-phase machine, appear as ac components at synchronous frequency. By applying a rotational transformation which rotates the x - y currents in the synchronous direction, the transformed x - y currents will appear as a combination of dc and ac components. The use of PI controllers in this synchronous reference frame will compensate the dc component. However, the ac component will only be suppressed to an extent dictated by the controller's bandwidth. In the light of this, it is desirable to select the most suitable reference frame, such that the x - y currents will appear predominantly as dc component, and can be easily compensated by the PI controller. Focusing on the six-phase machine, the nature of the x - y currents due to machine/converter asymmetry is analysed and a suitable reference frame for control is studied.

Using a general analysis, it can be shown that for a six-phase machine the stator x - y currents due to the machine/converter asymmetry can be fully described using the concept of symmetrical components and the concept of x - y currents discussed in Section 3.2. The six-phase stator currents of the six-phase machine are first separately

considered as two sets of three-phase currents, based on the concept of the double- dq model. If the double- dq transformations (3.3)-(3.4) are applied to these currents, $\alpha 1$ - $\beta 1$ and $\alpha 2$ - $\beta 2$ components are obtained. For ideal machine/converter without any asymmetry, the $\alpha 1$ - $\beta 1$ and $\alpha 2$ - $\beta 2$ currents form circular trajectories that are identical in radius and rotate at the same angular frequency $+\omega_s$. Both $\alpha 1$ - $\beta 1$ and $\alpha 2$ - $\beta 2$ currents can be represented by a positive sequence component, $\vec{I}_{\alpha\beta s+}$ according to (3.8) which is a rotating phasor.

However, if there is an imbalance due to the machine/converter asymmetry, the unbalanced currents will also contain a negative sequence component, $\vec{I}_{\alpha\beta s-}$. To illustrate a general case, the $\alpha 1$ - $\beta 1$ and $\alpha 2$ - $\beta 2$ currents are expressed as a sum of both positive and negative sequence components (it is assumed that there is no phase angle lead/lag between the components, for simplicity):

$$\begin{aligned}\vec{I}_{\alpha\beta s1} &= k_1 \vec{I}_{\alpha\beta s+} + k_2 \vec{I}_{\alpha\beta s-} = k_1 I_{\alpha\beta s} e^{+j\omega_s t} + k_2 I_{\alpha\beta s} e^{-j\omega_s t} \\ \vec{I}_{\alpha\beta s2} &= k_3 \vec{I}_{\alpha\beta s+} + k_4 \vec{I}_{\alpha\beta s-} = k_3 I_{\alpha\beta s} e^{+j\omega_s t} + k_4 I_{\alpha\beta s} e^{-j\omega_s t}\end{aligned}\quad (3.9)$$

Here β -axis leads α -axis by 90° and anti-clockwise rotation is considered as the positive direction. Coefficients k_i , $i = 1, 2, 3, 4$, depend on the type of the asymmetry.

Using the concept of the x - y currents of Section 3.2, the general expression for x - y currents due to the machine/converter asymmetry can be deduced as:

$$\vec{I}_{xys} = (k_1 - k_3) I_{\alpha\beta s} e^{-j\omega_s t} + (k_2 - k_4) I_{\alpha\beta s} e^{+j\omega_s t} = \vec{I}_{xys-} + \vec{I}_{xys+}\quad (3.10)$$

It should be noted that the rotational direction has changed, due to the opposite polarity in x - and y -current equations (3.7); hence the difference of positive sequence component in α - β plane appears as negative sequence component in x - y plane, and vice versa.

It can be concluded from (3.10) that the x - y currents, caused by machine/converter asymmetry, are of the fundamental frequency. Depending on the

type of asymmetry, these x - y currents can rotate in the synchronous, anti-synchronous or in both directions.

Three scenarios can be considered to illustrate the effect of machine/converter asymmetry on the x - y currents:

Case (A): Three-phase currents in both windings are balanced, but with different magnitudes. Hence $k_1 \neq k_3$; $k_2 = k_4 = 0$.

Case (B): Currents in winding 2 are balanced, but currents in winding 1 are unbalanced. Thus $k_1 \neq k_3$; $k_2 \neq 0$; $k_4 = 0$.

Case (C): Currents in both windings 1 and 2 have the same imbalance, so that $k_1 = k_3$; $k_2 \neq k_4$.

The corresponding x - y currents for the three scenarios are:

Case (A): only \vec{I}_{xy-} is present.

Case (B): both \vec{I}_{xy+} and \vec{I}_{xy-} are present.

Case (C): only \vec{I}_{xy+} is present.

By applying a pair of PI controllers to regulate the x - y currents in the synchronous reference frame, the positive sequence component will appear as a dc quantity and hence it can be easily compensated. Similarly, control of the negative sequence component will be made possible if the PI controllers are implemented in an anti-synchronous reference frame. Hence, it is expected that Case (A) and Case (C) require PI control in the anti-synchronous reference frame and the synchronous reference frame, respectively, whereas Case (B) will require both synchronous and anti-synchronous PI controllers for the asymmetry compensation. The experimental study is done using four types of PI controllers which operate in different reference frames, namely, the stationary, synchronous, anti-synchronous and dual (synchronous and anti-synchronous) reference frame, as shown in Fig. 3.5.

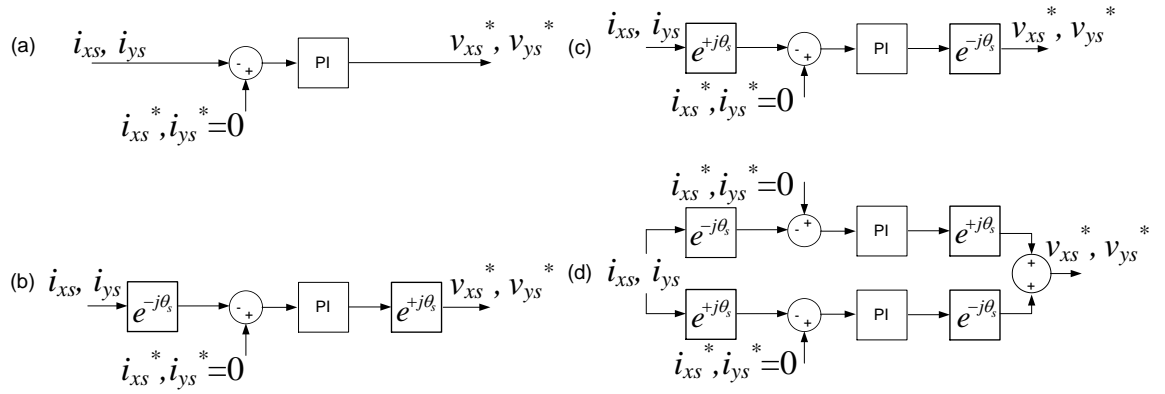


Fig. 3.5. PI current control of x - y currents, implemented in different reference frames: (a) stationary reference frame (b) synchronous reference frame (c) anti-synchronous reference frame, and (d) dual (synchronous and anti-synchronous) reference frame.

3.3.2. Dead-Time Compensation

The existence of inverter dead time introduces harmonics that distort the voltage and current. In the past, various methods have been proposed, especially for single and three-phase systems, where dead-time compensation has been made possible by means of calculating and compensating the voltage error (Jeong and Park, 1991; Wang *et al.*, 2011; Herran, *et al.*, 2013), or by the use of current control methods (Jones *et al.*, 2009; Han *et al.*, 2011). The implementation of the former usually requires knowledge of the system parameters and the phase current polarity, which causes difficulties in implementation. An interesting modification of the method was presented in (Hwang and Kim, 2010) where the output from the d -axis PI controller was used to estimate the voltage error that needs to be compensated. However, the implementation requires multiple integrators with specific control. The current control approach, on the other hand, relies on current controller(s) to suppress the dead-time related harmonic currents and hence achieve dead-time compensation. This approach, which does not require specific calculation of the dead-time voltage error, is considered here.

The dominant dead-time harmonics in multiphase machines appear as ac components in the x - y plane rather than in the d - q plane. The effect of dead time can thus be more severe because the machine's impedance in the x - y plane is low. It was shown in (Jones *et al.*, 2009) that dead-time caused harmonics in a five-phase induction

machine can be suppressed by using synchronous PI current controllers in the x - y plane. However, as discussed earlier, the PI controllers are unable to fully compensate ac components. Nonetheless, suppression of these components is made possible in (Jones *et al.*, 2009) by using a high proportional gain K_p for the synchronous x - y PI current controllers. The limitation of this approach is therefore the maximum value of K_p , which depends on factors such as computational and modulation delays.

Even though the dead-time voltage can exhibit non-linear characteristics at low current level (Guerero *et al.*, 2005), a simple representation of the dead-time effect as a square wave (Jeong and Park, 1991) is used in the discussion here. Using Fourier expansion, the square wave can be resolved into a series of odd order harmonics. For multiphase machines with multiple three-phase windings and mutually isolated neutrals, the third harmonic current cannot flow. Hence, the dominant dead-time harmonics are the 5th and 7th.

An alternative to PI controllers is the use of resonant controllers. For a three-phase system, the 5th and the 7th harmonic currents appear as current vectors rotating with frequencies of $-5\omega_s$ and $+7\omega_s$ in the stationary reference frame, where ω_s is the fundamental frequency. If a reference frame rotating with frequency $+\omega_s$ is used, as is the case when vector control is implemented, these harmonics will appear as the -6th and +6th harmonics, respectively. These harmonics can hence be compensated using a single resonant controller tuned at $6\omega_s$. The concept of utilising such synchronous reference frame resonant (SRF-Res) controller for harmonic compensation has been successfully applied for applications involving three-phase active filters (Bojoi *et al.*, 2005b; Lascu *et al.*, 2007; Limongi *et al.*, 2009; Bojoi *et al.*, 2009) and grid-tied converter (Liserre *et al.* 2006; Han *et al.*, 2011), where multiple SRF-Res controllers are used in parallel to compensate a wide range of harmonics. In (Liu *et al.*, 2012) single SRF-Res controller is used to control a doubly-fed induction generator under distorted grid voltage. Here,

this approach is adopted for dead-time compensation in the drive. For a three-phase machine, the resonant controller can be added in parallel to the d - q current controllers in the synchronous reference frame, as shown in Fig. 3.6.

The same dead-time compensator can be applied for the asymmetrical six-phase machine. However, in this case the 5th and the 7th harmonics appear in the x - y plane rather than in the d - q plane, and rotate with frequencies $+5\omega_s$ and $-7\omega_s$. In order to compensate for these dead-time harmonics, it is therefore necessary to use resonant controller in the anti-synchronous reference frame instead. The structure of the dead-time compensator for the six-phase machine using the resonant controller is shown in Fig. 3.7.

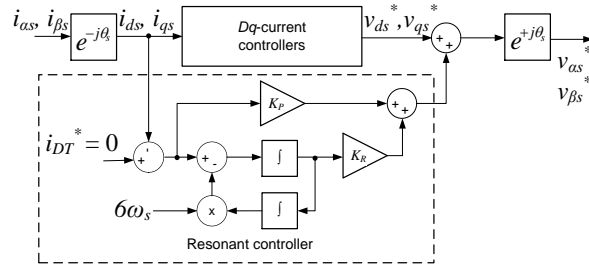


Fig. 3.6. Dead-time compensator for a three-phase machine using resonant controller in the synchronous (d - q) reference frame.

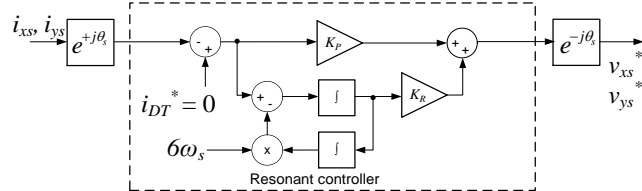


Fig. 3.7. Dead-time compensator for an asymmetrical six-phase machine using resonant controller in the anti-synchronous (x - y) reference frame.

The use of resonant controllers has gained in popularity in recent times (Holmes *et al.*, 2009; Yepes *et al.*, 2010; Yepes *et al.*, 2011a; Yepes *et al.*, 2011b; Cardenas *et al.*, 2012; Holmes *et al.*, 2012; Khajehoddin *et al.*, 2012). Since the resonant frequency is variable in this case, the two-integrator method is used to implement the resonant controller in the vector proportional-integral (VPI) form (Yepes *et al.*, 2011b). A comprehensive discussion of the improvement of frequency accuracy and stability margin of digital resonant controllers, by performing pole correction and delay compensation, is also available in (Yepes *et al.*, 2011b). Here, pole correction is

provided by using the forth-order approximation (not shown in Fig. 3.7). Since the order of harmonics to be compensated is low, VPI resonant controller allows stable operation even without delay compensation.

Using this structure of the resonant controller, the gains K_p and K_R are selected on the basis of $K_p/K_R = L_{ls_xy}/R_{xy}$ of the x - y plane. K_p is then selected to achieve desired selectivity and transient response of the controller (Lascu *et al.*, 2007). A large K_p improves transient response but reduces selectivity, so a compromise between the two is necessary. Since the resonant dead-time compensator is expected to operate in parallel with the other (x - y current) controllers, the value of K_p is selected as sufficiently small to minimise the effect on the other controllers.

3.4. Experimental Results and Discussions

3.4.1. Experimental Setup Overview

Experimental tests are conducted on an asymmetrical six-phase squirrel cage induction machine, configured with two isolated neutral points. It was obtained by rewinding a 1.1 kW, 380 V, 50 Hz machine, with rated current and speed of 1.75 A and 930 rpm, respectively. The machine is supplied using a custom-made eight-phase two-level VSC, configured for six-phase operation. A dc power supply (Sorensen SGI 600-25) is used to provide the dc-link voltage of 300 V to the VSC. A 5 kW dc machine is mechanically coupled to the six-phase machine and is controlled using ABB DCS800 drive in the torque control mode, to provide loading of the six-phase machine. The experimental setup is shown in Fig. 3.8.

The six-phase machine is controlled using indirect rotor flux oriented control (IRFOC) in closed-loop speed control mode. The double zero-sequence injection carrier-based PWM (Bojoi *et al.*, 2002) is utilized. The complete control algorithm is implemented using dSpace DS1006 system. Switching frequency is 5 kHz, with 6 μ s

dead time provided by the hardware in the VSC. Machine phase currents and dc-link voltage are measured (using the LEM sensors embedded in the VSCs) through dSpace at a sampling frequency of 10 kHz. Currents are filtered for display purposes using a low-pass filter with the cut-off frequency of 2 kHz. For variables such as x - y currents and machine speed, the values are calculated within dSpace and displayed on the oscilloscope via DS2101 DAC module. To provide current display at higher resolution, current probe (TCP0030) and Tektronix oscilloscope (MSO2014) are used. The machine and control parameters are given in Table 3.1.

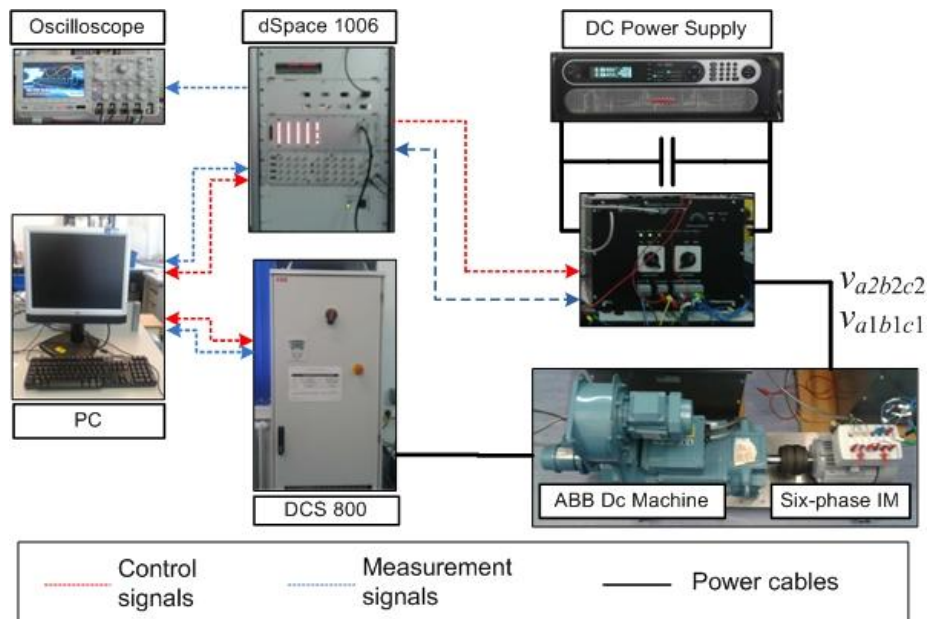


Fig. 3.8. Experimental setup for the asymmetrical six-phase induction motor drive testing.

Table 3.1. Experimental system parameters.

Machine parameters			
$R_s = 12.5 \Omega$	$R_r = 12.0 \Omega$	$J = 0.04 \text{ kg}\cdot\text{m}^2$	$p = 3$
$L_{ls_dq} = 0.0615 \text{ H}$	$L_{lr} = 0.0110 \text{ H}$	$L_m = 0.590 \text{ H}$	
$L_{ls_xy} = 0.0055 \text{ H}$			
Converter Parameters			
$C_1 = C_2 = 1500 \mu\text{F}$	$V_{dc1} = V_{dc2} = 300 \text{ V}$		
Controller Parameters			
$f_{switching} = 5 \text{ kHz}$	$f_{sampling} = 10 \text{ kHz}$		
D-q current controllers:	$K_p = 60$	$K_i = 8000$	
Speed controller:	$K_p = 0.05$	$K_i = 0.05$	

The experimental results are presented in the following order: Section 3.4.2 shows the effect of dead-time compensation using PI controllers and the resonant controller. This helps to establish the effectiveness of the dead-time compensation technique discussed in Section 3.3.2. Section 3.4.3 then discusses the asymmetry compensation capabilities of the PI controllers in different reference frames. In order to

remove the dead-time harmonics from the currents so that the effect of asymmetry becomes more visible, the dead-time compensator of Section 3.4.2 is used throughout the experiments in Section 3.4.3.

3.4.2. Dead-Time Compensator

In order to verify the performance of the resonant dead-time compensator discussed in Section 3.3.2, the controller is compared with the dead-time compensation scheme of (Jones *et al.*, 2009), based on PI controllers in the synchronous reference frame. Based on the considerations presented in Section 3.3, the resonant controller gains are selected as $K_p = 1$ and $K_R = 2272$. For PI controllers, since the dead-time compensation effect depends primarily on the proportional part of the controller, the proportional gain is tuned to be as high as possible without having the controller going into instability. Via trial and error, K_p is found to be 70 in this case. The integral gain, which has little effect on dead-time harmonics, is chosen to be 2500.

The machine is at first operated at a constant speed of +500 rpm without load. The performance of different controllers is compared in Fig. 3.9. Fig. 3.9(a) shows the operation when only $d-q$ current controllers are used. Since no $x-y$ current control is provided, the dead time harmonics are left uncompensated. FFT spectrum of the phase current (obtained by processing the oscilloscope data in Matlab) shows that the phase current contains harmonics with the dominant 5th and 7th order components. Note that the scales of the FFT spectra in Fig. 3.9 and 3.10 have been enlarged to show the dead-time harmonics, so that the fundamental frequency components are truncated at 0.1. Fig. 3.9(b) shows the case when synchronous PI controllers of (Jones *et al.*, 2009) are used. Results show significant improvement of the current waveform since harmonics in the $x-y$ currents have been reduced. FFT analysis shows that the 5th and the 7th harmonic currents have been suppressed to a good extent. The test is repeated next using stationary reference frame PI controllers with the same PI gains ($K_p = 70$ and $K_i = 2500$)

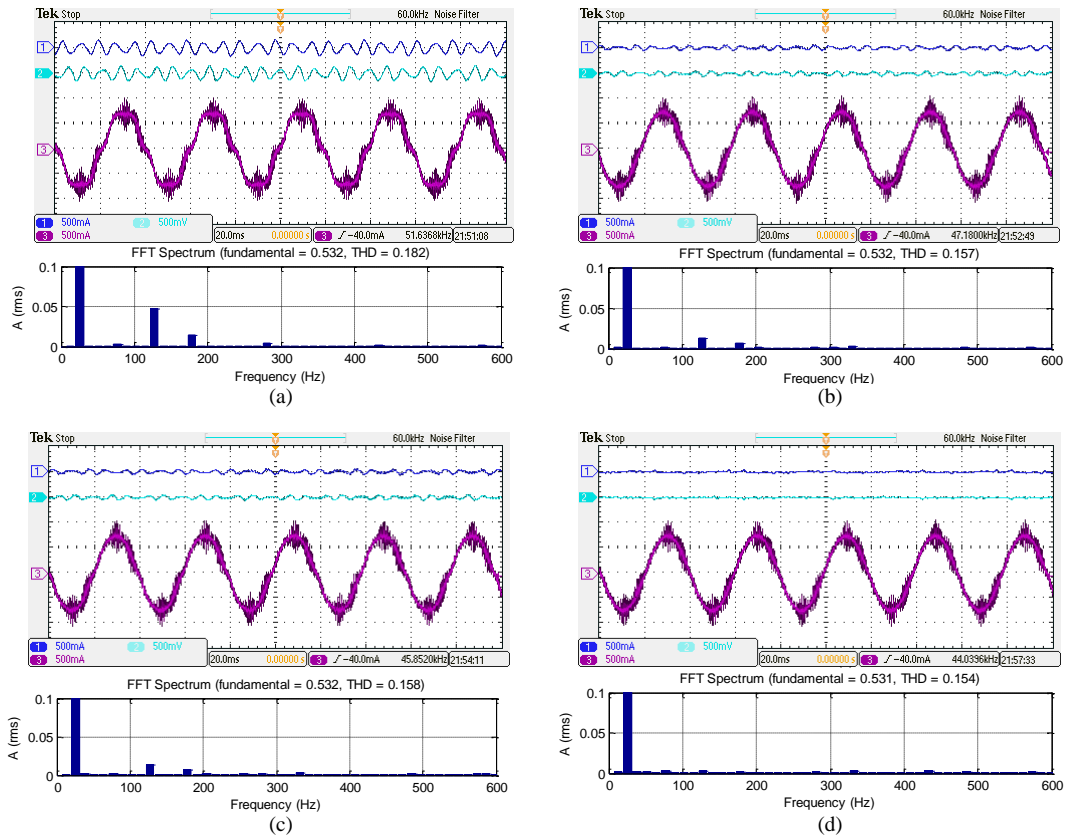


Fig. 3.9. Experimental results (with FFT spectrum of phase- $a1$ current) for no-load operation at 500 rpm with $d-q$ current controllers and (a) no $x-y$ current controllers (b) $x-y$ current control using synchronous PI controllers (c) $x-y$ current control using stationary PI controllers (d) $x-y$ current control using synchronous resonant controller: Channel 1: i_x (0.5A/div), Channel 2: i_y (0.5A/div), Channel 3: phase- $a1$ current (0.5A/div), Horizontal: Time (20ms/div).

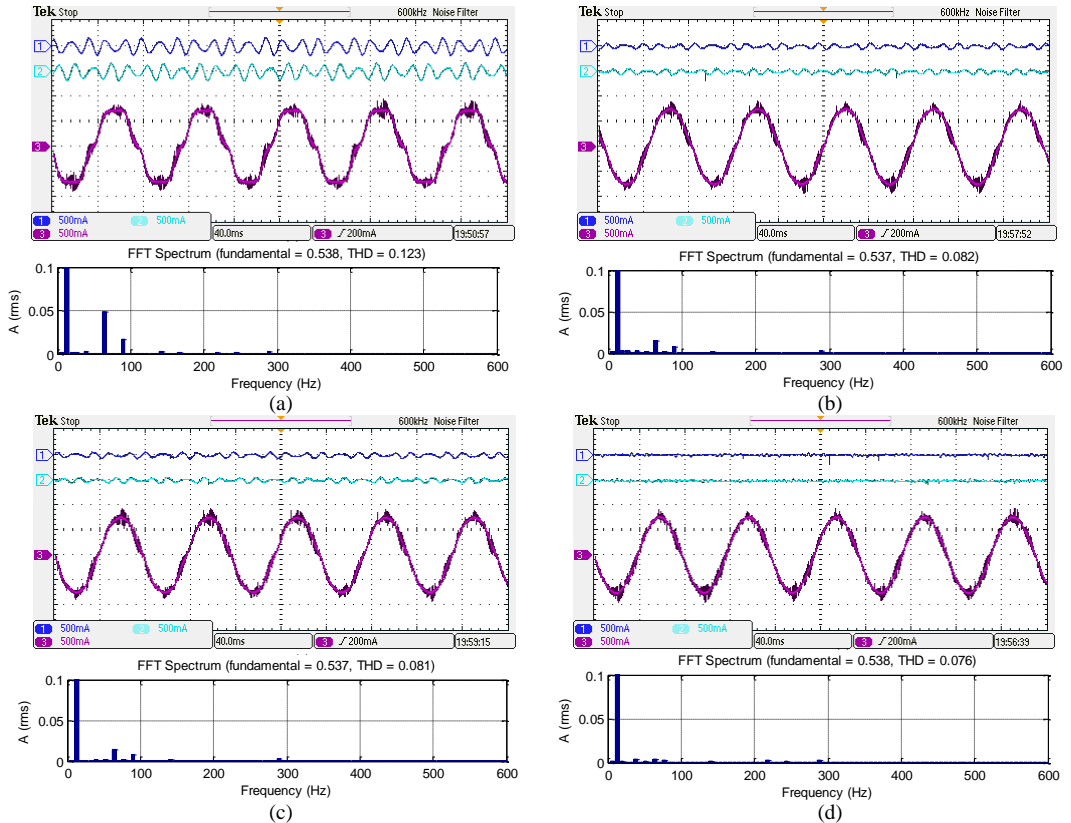


Fig. 3.10. Experimental results (with FFT spectrum of phase- $a1$ current) for no-load operation at 250 rpm with $d-q$ current controllers and (a) no $x-y$ current controllers (b) $x-y$ current control using synchronous PI controllers (c) $x-y$ current control using stationary PI controllers (d) $x-y$ current control using synchronous resonant controller: Channel 1: i_x (0.5A/div), Channel 2: i_y (0.5A/div), Channel 3: phase- $a1$ current (0.5A/div), Horizontal: Time(40ms/div).

and the results are shown in Fig 3.9(c). It is observed that the harmonic suppression capability is almost identical to the synchronous frame PI controllers. This shows that here the reference frame has little impact in terms of the dead-time compensation (the dominant dead-time harmonic in (Jones *et al.*, 2009) is the 3rd, while here the dominant harmonics are at higher frequencies, the 5th and the 7th). The performance of the dead-time compensator using the resonant controller is shown in Fig. 3.9(d). Compared with stationary and synchronous PI control, the resonant controller is able to provide much more effective compensation of the 5th and the 7th harmonics, which are in essence eliminated. The performance is good despite the small value of the gains used. This shows the superiority of the resonant dead-time compensator over those based on PI controllers. It is worth noting that an improvement of total harmonic distortion (THD) is also observed with the dead-time compensation (THD values are given in the headings of current spectra). However, the improvement is small because the THD is dominated by the high order switching related harmonics, which largely depend on the choice of the pulse width modulation method (Dujic *et al.*, 2010).

The same set of tests is repeated for the machine operating at +250 rpm, and the results are shown in Fig. 3.10. Again, synchronous (Fig. 3.10(b)) and stationary (Fig.3.10(c)) PI controllers show similar but limited harmonic suppression capability, while the resonant controller (Fig. 3.10(d)) exhibits a far superior performance.

The dynamic performance of the dead-time compensator is tested by reversing the speed of the machine from +500 rpm to -500 rpm. As shown in Fig. 3.11, the addition of the dead-time compensator does not affect the speed control (d - q current control) of the machine, and the system remains stable. It should be emphasised that the resonant controller only suppresses the 5th and the 7th order dead-time harmonics, so a small amount of fundamental frequency component due to the inherent machine/converter asymmetry appears in the steady state x - y currents.

Fig. 3.12 shows the performance of the dead-time compensator when the machine's load torque is varied. The six-phase machine is at first loaded with 50% of the rated torque using the dc motor coupled to the machine. At $t = 1.0$ s, the load torque is removed. Small oscillations in x - y currents can be observed during transient due to the controller's limited response speed. Nevertheless, the controller is able to suppress the harmonics during steady state. Some small oscillations are again present in steady state as a result of the inherent machine/converter asymmetry.

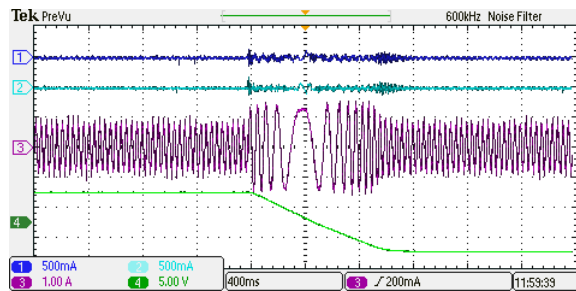


Fig. 3.11. Experimental results showing speed reversal (+500 rpm to -500 rpm) of the machine in no-load operation with resonant dead time compensator activated: Channel 1: i_x (0.5A/div), Channel 2: i_y (0.5A/div), Channel 3: phase- $a1$ current (1.0A/div), Channel 4: speed (500rpm/div), Horizontal: Time (400ms/div).

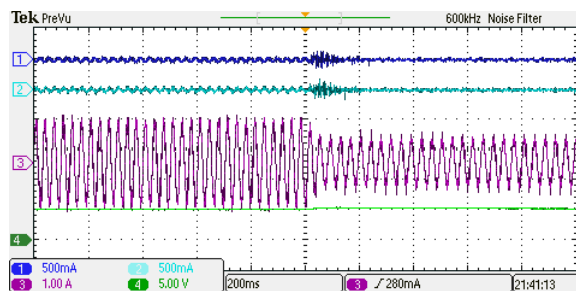


Fig. 3.12. Experimental results showing machine operating at +500 rpm with load torque removed at $t = 1.0$ s: Channel 1: i_x (0.5A/div), Channel 2: i_y (0.5A/div), Channel 3: phase- $a1$ current (1.0A/div), Channel 4: speed (500rpm/div), Horizontal: Time (200ms/div).

3.4.3. Asymmetry Compensation

This section shows the results of the machine/converter asymmetry compensation using PI controller in different reference frames for x - y current control. As discussed above, depending on the type of the asymmetry, fundamental frequency x - y currents will appear in the synchronous, anti-synchronous or both reference frames. It is expected that the synchronous PI controllers can eliminate the synchronous component, and the anti-synchronous PI controller will be able to compensate the anti-synchronous component. By observing the performance of the PI controllers, the type of components present in the x - y currents can be concluded upon. Four types of PI

controllers, all shown in Fig. 3.5 (stationary, synchronous, anti-synchronous and dual-synchronous reference frame PI controllers), are discussed in this section.

In order to suppress the harmonics due to the dead-time effect, the resonant dead time compensator is activated in parallel with the PI controllers. PI controllers' gains are tuned in the following manner: the ratio of K_p / K_i is chosen to be equal to L_{ls_xy}/R_{xy} to cancel out the dominant pole of the x - y plane. In order to show a clearer effect of the reference frame and reduce the interference with the dead-time compensator, a small value of K_p is chosen, i.e. $K_p = 1$. Cross-coupling effect is reduced by adding terms $-\omega_s L_{ls_xy} i_{ys}$ and $+\omega_s L_{ls_xy} i_{xs}$ to the outputs of the x - and y -controllers, respectively, using measured currents. It should be noted that, when dual PI controllers are used, these terms are unable to provide cross-coupling decoupling, since terms from synchronous and anti-synchronous controllers cancel each other. More sophisticated decoupling approaches, such as for example the use of complex PI (Lascu *et al.*, 2007), can overcome this problem; this is however beyond the scope of this study.

In order to show the effect of asymmetry on phase currents in different windings, the currents of phase- $a1$ and phase- $a2$ are shown further on. The inherent asymmetry in the machine/converter is investigated first. The machine runs without load with the set speed of +500 rpm using IRFOC. Fig. 3.13(a) shows the x - y , phase- $a1$ and phase- $a2$ currents when x - y current control is not implemented (except for the dead time compensator, which eliminates dead-time related 5th and 7th harmonics). The ripples in the x - y currents are mainly due to the machine/converter asymmetry and noise. From the figure, the inherent asymmetry is small in no-load operation. Fig. 3.13(b) and 3.13(c) show the results when synchronous PI and anti-synchronous PI x - y current controllers are used. By comparing the fundamental frequency component in x - y currents, it is found that anti-synchronous PI provides better compensation than the synchronous PI

controller (which provides hardly any improvement). This indicates that the inherent asymmetries in this machine mainly produce anti-synchronous x - y currents.

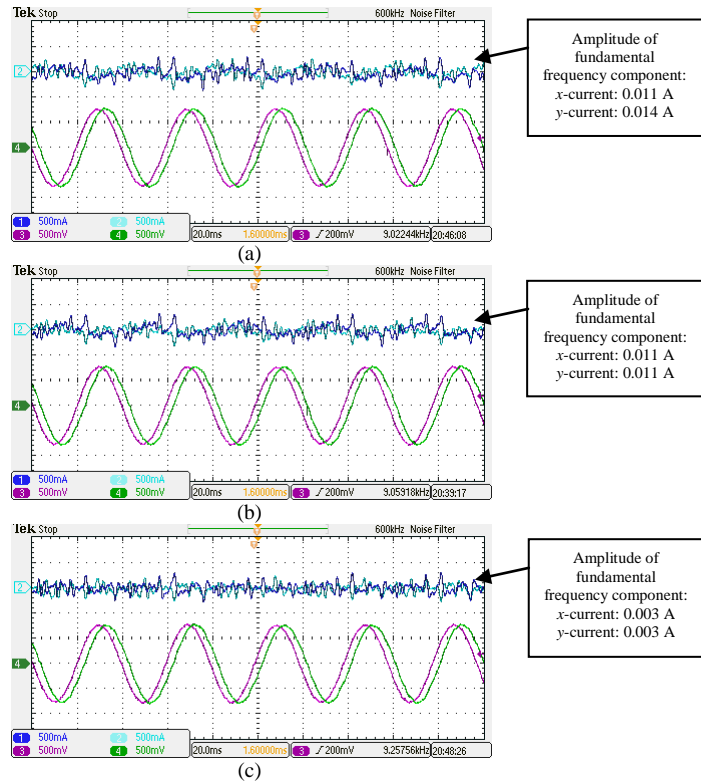


Fig. 3.13. Experimental results showing the inherent machine asymmetry, when machine runs at +500 rpm without load, with (a) no x - y current control, and with x - y current control using (b) synchronous PI (c) anti-synchronous PI control: Channel 1: i_x (0.05A/div), Channel 2: i_y (0.05A/div), Channel 3: phase- $a1$ current (0.5A/div), Channel 4: phase- $a2$ current (0.5A/div), Horizontal: Time (20ms/div). (Markers for Channel 1 and Channel 3 have been overlapped by markers from Channel 2 and Channel 4, respectively).

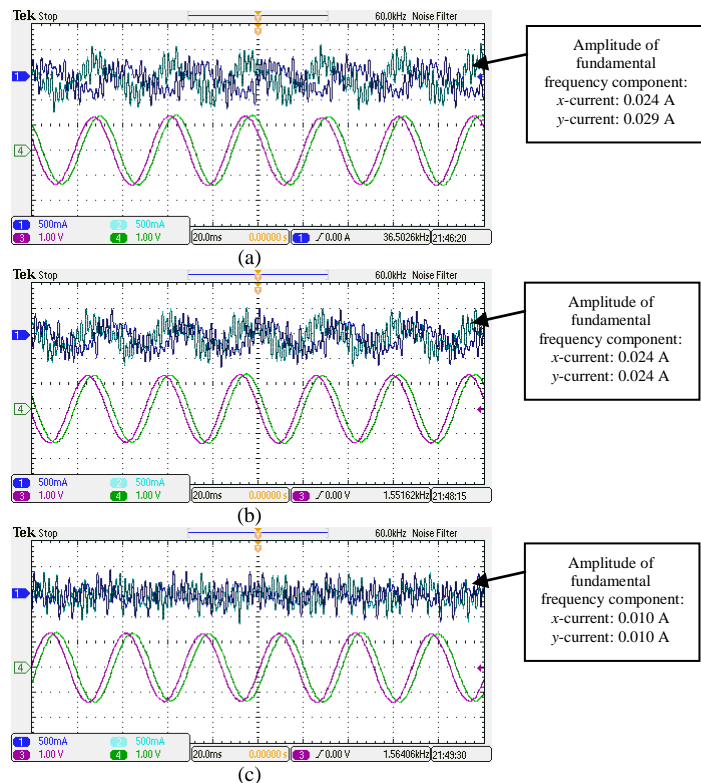


Fig. 3.14. Experimental results showing the inherent machine asymmetry, when machine runs at +500 rpm with 50% rated load, with (a) no x - y current control, and with x - y current control using (b) synchronous PI (c) anti-synchronous PI control: Channel 1: i_x (0.05A/div), Channel 2: i_y (0.05A/div), Channel 3: phase- $a1$ current (1.0A/div), Channel 4: phase- $a2$ current (1.0A/div), Horizontal: Time (20ms/div). (Markers for Channel 1 and Channel 3 have been overlapped by markers from Channel 2 and Channel 4, respectively).

Fig. 3.14 shows the effect of machine loading by applying 50% of the rated torque to the machine, while keeping the speed at +500 rpm. Compared to Fig. 3.13, the amplitude of x - y currents has increased because of the increase in the phase currents. The impact of adding the synchronous and anti-synchronous PI controllers can be observed in Fig. 3.14(b) and 14(c), respectively. Similar to the no-load case in Fig. 3.13, anti-synchronous PI controllers provide better performance, confirming that the inherent asymmetry caused x - y currents are predominantly of anti-synchronous type.

In order to verify the discussion in Section 3.3, three types of asymmetry are emulated next, by adding external resistors $R_{external}$ in series with the stator windings. For Case (A), stator resistance in phases $a1$, $b1$ and $c1$ is increased by 5.7Ω . For Case (B), only the resistance in phase- $a1$ is increased by 5.7Ω . For Case (C), resistors of 5.7Ω are added in phase- $a1$ and phase- $a2$. Since the inherent asymmetry is much smaller than the emulated asymmetry, its effect can be considered now as negligible.

The experimental results are shown in Fig. 3.15. To facilitate the comparison, results for different types of asymmetry are placed in three separate columns, as indicated with the legend on the top of Fig. 3.15. Each row shows the results for one particular PI current control method in the x - y plane. The speed is kept at +500 rpm. For simplicity, the machine is operated without load. The first row shows the results when only d - q currents are controlled and no x - y current control is provided. This is done by setting the x - y voltage references to zero. The scenario would have been perfectly sufficient for the control of the drive had the inverter and the machine been ideal, as explained in (Jones *et al.*, 2009) in conjunction with a five-phase machine. It can be observed that the different types of asymmetry introduce x - y currents that are different not only in their magnitudes, but also in the phase relation between x - y currents. By observing the lead-lag relation between the x - y currents, the presence of synchronous and/or anti-synchronous component can be deduced. For Case (A), y -current leads x -

current, indicating that the x - y currents are mainly rotating in the anti-synchronous direction. The opposite can be observed for Case (C), where x -current is leading y -current. For Case (B), there is no obvious lead or lag relation between the x - and y -current, which implies that synchronous and anti-synchronous components of comparable magnitude are present. These observations show that the emulated asymmetries closely resemble those described in Section 3.3.

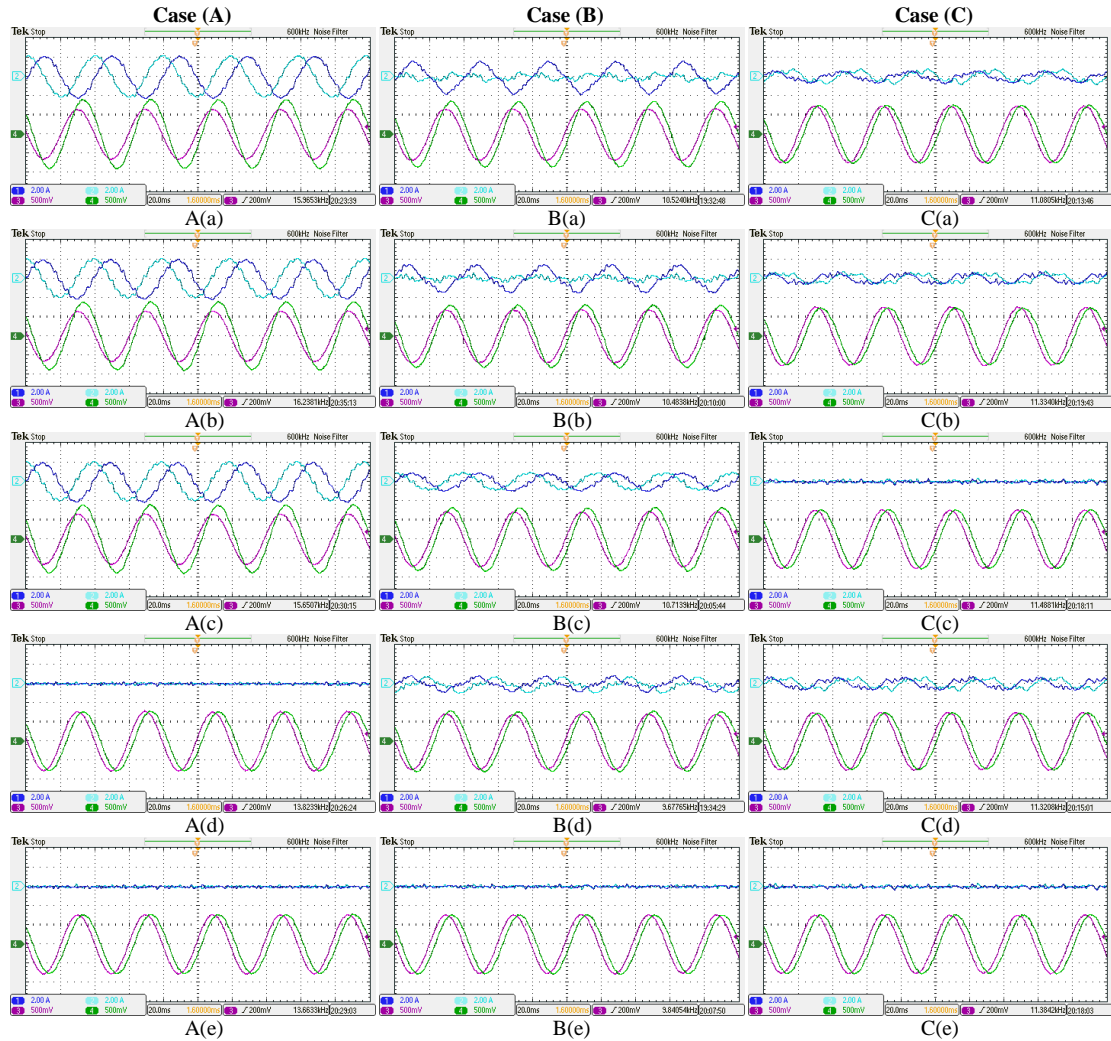


Fig. 3.15. Experimental results showing asymmetry compensation effect (a) without x - y current control (x - y voltage references set to zero), and with x - y current control using (b) stationary PI (c) synchronous PI (d) anti-synchronous PI, and (e) dual PI controllers for Cases (A), (B) and (C): Channel 1: i_x (0.2A/div), Channel 2: i_y (0.2A/div), Channel 3: phase- $a1$ current (0.5A/div), Channel 4: phase- $a2$ current (0.5A/div), Horizontal: Time (20ms/div). (Markers for Channel 1 and Channel 3 have been overlapped by markers of Channel 2 and Channel 4, respectively).

Row (b) shows the results when stationary PI controllers are used to suppress the x - y currents. Since all the x - y currents appear as ac quantities in the stationary reference frame, there is practically no improvement over the case without x - y current control. This is partly due to the fact that the controllers have been tuned with low bandwidth.

Increasing controllers' gain would undoubtedly improve the performance, but full compensation of the x - y currents cannot be achieved. Row (c) shows the performance of synchronous PI controllers. For Case (A), the synchronous PI controllers are unable to compensate the anti-synchronous x - y currents, since they appear as ac quantities with frequency of $2\omega_s$ to the synchronous PI controllers. For Case (B), the synchronous PI controllers are capable of suppressing the synchronous x - y current components. However, the uncompensated anti-synchronous component still flows in the machine, so the phase currents remain unbalanced. In Case (C), the x - y currents appear as dc component to the synchronous PI controller and hence can be fully compensated.

The effect of anti-synchronous PI control is seen in row (d) of Fig. 3.15. It can be observed that the anti-synchronous PI controller is capable of eliminating the x - y currents in Case (A) but not in Case (C) due to the fact that x - y currents only contain anti-synchronous component in Case (A), and only synchronous component in Case (C). For Case (B), the anti-synchronous PI controllers only provide partial suppression of the asymmetrical currents, and the synchronous x - y current components remain unsuppressed. Row (e) shows the performance of the dual PI controllers. Since both synchronous and anti-synchronous PI controllers are present, x - y currents can be effectively compensated in all the three cases. This shows that the dual PI controllers are naturally capable of eliminating any x - y currents caused by the machine/converter asymmetry. Dual PI controllers are actually equivalent to a resonant controller in the stationary reference frame, with resonant frequency equal to the fundamental frequency.

On the basis of the presented results, it can be concluded that the x - y current control based on a dual PI or resonant controllers is the best choice in terms of the machine/converter asymmetry compensation. The use of dual PI controller can also be useful to allow fault-tolerant control of the machine, as demonstrated in (Tani *et al.*, 2012) and will be discussed in Chapter 5 later. Nevertheless, the results also show that if

the type of asymmetry is known, it is possible to achieve the same performance with just a single PI controller per axis in the correct reference frame.

3.5. Conclusion

The chapter shows that the x - y currents in an asymmetrical six-phase machine can be physically interpreted as circulating currents between the two three-phase windings of the machine. By using this concept, the relation between the type of asymmetry in the machine/converter and the currents in the x - y plane has been established. Subsequently, two important aspects of the x - y current control, i.e. asymmetries and dead-time compensation, have been discussed. For dead-time compensation, a resonant controller implemented in the anti-synchronous reference frame shows the best performance, as proven on the basis of experimental results.

In terms of the asymmetry compensation, it is shown that the inherent machine/converter asymmetry produces x - y currents that rotate at fundamental frequency. The x - y currents can, however, rotate in the synchronous, anti-synchronous or both directions, depending on the type of the asymmetry present. The effectiveness of asymmetry compensation using PI controllers hence depends on the reference frame in which the control is implemented. Full compensation for all the possible cases is achievable only with the dual PI controllers (i.e. pairs in both synchronous and anti-synchronous reference frames). The validity of the discussion is verified by experimental results.

Chapter 4

OPERATION WITH SERIES-CONNECTED MACHINE-SIDE CONVERTERS

4.1. Introduction

Multiphase variable-speed drive systems with back-to back converter configuration utilise typically a multiphase two-level or three-level voltage source converter (VSC) at the machine side (Levi *et al.*, 2007). Multiphase generator studies have concentrated on the use of standard n -phase VSCs or diode rectifiers, depending on the machine type, with n converter legs connected in parallel to the dc-link. Such a topology where two parallel three-phase VSCs drive a six-phase wind energy system is shown in Fig. 4.1(a). This is at the same time the typical structure of an asymmetrical

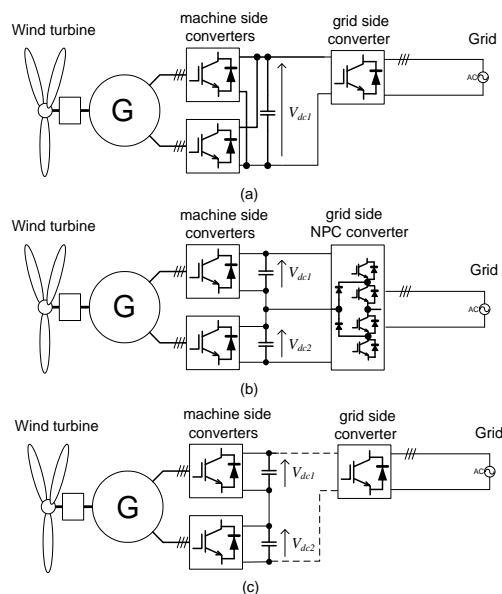


Fig. 4.1. Six-phase generation system with (a) parallel machine-side converters, (b) series machine-side converters with dc-link midpoint connection and (c) series machine-side converter without dc-link midpoint connection.

six-phase machine when used in a variable-speed drive system.

In (Duran *et al.*, 2011), a unique converter topology was introduced for an asymmetrical six-phase permanent magnet synchronous generator. The topology uses two three-phase machine-side converters which are connected in series to form a cascaded dc-link. A three-level neutral point clamped (NPC) converter was used as the grid-side converter in a back-to-back manner, with a connection to the dc-link midpoint, as shown in Fig. 4.1(b). In this configuration, the dc-link midpoint voltage can be controlled by the grid-side NPC converter, such that the two dc-link capacitor voltages are always balanced. The topology of Fig. 4.1(b) is equally applicable to the variable-speed drives and can be used in conjunction with both permanent magnet synchronous and induction machines. The series-connected machine-side topology means that the individual dc-link voltages (V_{dc1} and V_{dc2} in Fig. 4.1(b)) of the six-phase system need only be equal to 50% of the total required dc voltage, achieving a higher total dc-link voltage ($V_{dc1}+V_{dc2}$) for the same voltage rating of the converters. The dv/dt of the common-mode voltage (CMV), which is known to be a main cause of leakage currents in high power applications, is therefore halved as well. The total number of the semiconductor switches of the machine-side converter for a six-phase machine with two-level VSCs is equal to what is required for a three-level three-phase VSC. The elevated dc-link voltage in this series-connected topology reduces the current rating and the cable size for the given power, hence giving a potential overall capital cost reduction.

Although the voltage of the converters is halved in the series connection, it should be noted that the voltage stress within the machine can still reach a value up to the total dc-link voltage (V_{dc}). Nevertheless, since not the whole machine is under this maximum voltage stress, the overall insulation requirement is expected to be lower than that of a higher-voltage machine designed with phase voltage rating based on the full

V_{dc} voltage. As a matter of fact, part of the voltage stress can be reduced via proper choice of the PWM technique, as discussed later in Section 4.3.

Although the topology of (Duran *et al.*, 2011) is potentially interesting, the three-wire connection shown in Fig. 4.1(b) can be uneconomical if the dc-link is long and the grid-side converter is located far apart. While this may or may not be relevant for variable-speed drive applications, it would be relevant in offshore wind farms with a dc-offshore grid and high voltage direct current (HVDC) transmission to the onshore grid-side converter (Liserre *et al.*, 2011). Offshore wind farms are currently promoted by some countries' policies (Sun *et al.*, 2012) and manufacturers (e.g. RePower (Wu *et al.*, 2011)) due to the better wind resources and absence of the visual impact. Newly designed offshore wind farms require higher powers and better reliability, which makes them suitable for the utilisation of multiphase generators. If the wind farm distance to the shore is above a certain break-even distance (typically around 70 kilometres (Wu *et al.*, 2011)), the use of HVDC transmission becomes more favourable and the three-wire topology of Fig. 4.1(b) is not adequate. For this reason, the topology in (Duran *et al.*, 2011) can be modified, to eliminate the need for the dc-link midpoint connection to the grid side, as shown in Fig. 4.1(c). This provides a favourable arrangement for remote offshore wind generation with dc-offshore grid. This chapter is dedicated to the investigation of the operation of an asymmetrical six-phase induction machine with series connected machine-side converters as in Fig. 4.1(c).

Since the grid-side converter can no longer control the voltage of the dc-link midpoint, the voltage drifting becomes a problem for this topology unless the dc-link voltages can be controlled from the machine side. Fortunately, the additional degrees of freedom of the six-phase machine allow the voltage balancing using an additional controller. It should be noted that the additional degrees of freedom of a multiphase machine have been used in the past for various specific aims (e.g., torque enhancement

with low-order stator current harmonic injection, development of fault-tolerant control algorithms for post-fault operation, independent control of a multitude of series-connected multiphase machines using a single voltage source converter (Levi *et al.*, 2007). However, there is no evidence that the capacitor voltage balancing has ever been attempted before by utilising these additional degrees of freedom.

The concept of cascading converters to achieve elevated dc link voltage is of course not new, and it has been reported in several works (Ng *et al.*, 2008; Parker *et al.*, 2011; Gjerde *et al.*, 2012; Gjerde and Undeland, 2012; Olsen *et al.*, 2012; Xiang-Jun, *et al.*, 2012; Yuan *et al.*, 2012; Parker *et al.*, 2013). However, such solutions usually require specially designed machines or customised converters. When diode-based rectifiers are used, the applicability is restricted to synchronous generators. The topology discussed here uses standard three-phase VSCs which provide advantages in terms of economy and technology maturity. Moreover, the use of VSCs allows the topology to be used also with induction machines, in both motoring and generating mode.

This chapter is organised as follows: Section 4.2 presents an overall description of the system, including the topology, induction machine model and control structure. Section 4.3 analyses the merits and demerits of the topology and the dc-link voltage drifting issue. Detailed derivation of the dc-link voltage controller is given in Section 4.4. The theoretical development is supported using simulation and experimental results, provided in Section 4.5. Finally, concluding remarks are given in Section 4.6.

4.2. System Description

4.2.1. System Topology

In this study, the machine is an asymmetrical six-phase squirrel-cage induction machine with two isolated neutral points, driven by two three-phase two-level VSCs

which are connected in series to form a cascaded dc-link. Since the focus of the discussion is on the machine-side converters, a three-phase two-level VSC is considered as the grid-side converter in this study, for the sake of simplicity. However, it should be emphasised that the grid-side converter is not restricted to the two-level VSC and, as already noted, more advanced converters, such as multilevel neutral-point clamped (NPC) converters, can also be used.

4.2.2. Induction Machine Model

Using the VSD technique, the machine model can be decoupled into three orthogonal subspaces, denoted as α - β , x - y and zero-sequence subspaces. For machines with distributed windings, only α - β components contribute to the useful electromechanical energy conversion, while x - y and zero-sequence components only produce losses. These x - y current components represent the additional degrees of freedom, referred to previously. Power invariant decoupling transformation is used again to convert the phase variables of the stator (a_1, b_1, c_1, a_2, b_2 and c_2) and rotor windings into α - β and x - y variables (Levi *et al.*, 2007a), as discussed in Chapter 3:

$$[T] = \frac{1}{\sqrt{3}} \begin{bmatrix} \alpha & 1 & -\frac{1}{2} & -\frac{1}{2} & \frac{\sqrt{3}}{2} & -\frac{\sqrt{3}}{2} & 0 \\ \beta & 0 & \frac{\sqrt{3}}{2} & -\frac{\sqrt{3}}{2} & \frac{1}{2} & \frac{1}{2} & -1 \\ x & 1 & -\frac{1}{2} & -\frac{1}{2} & -\frac{\sqrt{3}}{2} & \frac{\sqrt{3}}{2} & 0 \\ y & 0 & -\frac{\sqrt{3}}{2} & \frac{\sqrt{3}}{2} & \frac{1}{2} & \frac{1}{2} & -1 \end{bmatrix} \quad (4.1)$$

Zero-sequence components are omitted from the consideration (and are therefore not included in (4.1)) since the machine has two isolated neutral points. Two pairs of real variables that result after application of (4.1) onto phase quantities (α - β and x - y) can be combined into the corresponding space vectors (Levi *et al.*, 2007a).

A rotational transformation is applied next to transform the α - β variables into a synchronously rotating reference frame (d - q), suitable for vector control:

$$[D] = \begin{matrix} d \\ q \\ x \\ y \end{matrix} \begin{bmatrix} \cos \theta_s & \sin \theta_s & & \\ -\sin \theta_s & \cos \theta_s & & \\ & & 1 & \\ & & & 1 \end{bmatrix} \quad (4.2)$$

The transformation of d - q variables in (4.2) is identical as in the case of a three-phase system. The second pair of variables (x - y) is not rotationally transformed since the equations for these variables do not contain stator-to-rotor coupling (x - y quantities do not contribute to the electromagnetic torque and hence electromechanical energy conversion). In (4.2) θ_s is the angle of the rotational transformation for the stator. Assuming that the electrical angular speed of the machine is ω_r and the reference frame is rotating at an arbitrary speed ω (so that $\theta_s = \int \omega dt$), the model of the induction machine can be described using the following voltage and flux equations in the d - q plane (indices s and r indicate stator and rotor quantities, respectively; motoring convention for the positive stator current flow is used):

$$\begin{aligned} v_{ds} &= R_s i_{ds} + d\psi_{ds} / dt - \omega \psi_{qs} \\ v_{qs} &= R_s i_{qs} + d\psi_{qs} / dt + \omega \psi_{ds} \\ 0 &= R_r i_{dr} + d\psi_{dr} / dt - (\omega - \omega_r) \psi_{qr} \\ 0 &= R_r i_{qr} + d\psi_{qr} / dt + (\omega - \omega_r) \psi_{dr} \end{aligned} \quad (4.3)$$

$$\begin{aligned} \psi_{ds} &= (L_{ls} + L_m) i_{ds} + L_m i_{dr} \\ \psi_{qs} &= (L_{ls} + L_m) i_{qs} + L_m i_{qr} \\ \psi_{dr} &= (L_{lr} + L_m) i_{dr} + L_m i_{ds} \\ \psi_{qr} &= (L_{lr} + L_m) i_{qr} + L_m i_{qs} \end{aligned} \quad (4.4)$$

where R_s and R_r are stator and rotor resistances, while L_{ls} , L_{lr} and L_m are stator and rotor leakage and magnetising inductances, respectively. Additional stator equations, which describe the machine in the x - y plane, are:

$$\begin{aligned} v_{xs} &= R_s i_{xs} + d\psi_{xs} / dt \\ v_{ys} &= R_s i_{ys} + d\psi_{ys} / dt \end{aligned} \quad (4.5)$$

$$\begin{aligned} \psi_{xs} &= L_{ls} i_{xs} \\ \psi_{ys} &= L_{ls} i_{ys} \end{aligned} \quad (4.6)$$

For a machine with p pole pairs, the electromagnetic torque solely depends on the d - q components and is given with:

$$T_e = pL_m [i_{dr}i_{qs} - i_{ds}i_{qr}] \quad (4.7)$$

Finally, the equation of the rotor motion is:

$$T_e - T_m = J \frac{d\omega_m}{dt} \quad (4.8)$$

where ω_m is the rotor mechanical speed, J is the inertia, and T_m is the mechanical (prime mover or load) torque.

4.2.3. Control Structure

Based on the VSD model, the six-phase induction machine is controlled using indirect rotor flux oriented control (IRFOC). The rotor flux angle, required for the rotational transformation (4.2), is calculated on the basis of the conventional indirect orientation principles, using slip frequency ω_{sl}^* .

$$\theta_s = \int (p\omega_m + \omega_{sl}^*) dt \quad (4.9)$$

$$\omega_{sl}^* = \frac{1}{\tau_r} \frac{i_{qs}^*}{i_{ds}^*} \quad (4.10)$$

Due to the additional degrees of freedom, instead of using just two PI controllers for the d - q current control, two extra current controllers are required for the x - y current control. The schematic of the machine-side current control is shown in Fig. 4.2. There are various control schemes that can be used for the x - y current control in multiphase machines as discussed in Chapter 3. Here, an anti-synchronous reference frame, as elaborated in Chapter 3, is used for the x - y PI current controllers since it allows an easy implementation of the dc-link voltage balancing control. It should be emphasised here that instead of the exponential form shown in Fig. 3.3, the matrix form of rotational transformation, $[D]$ is used here for convenience. Superscript $'$ is added to the matrix $[D]$ and x - y currents in Fig. 4.2 to differentiate them from those based on equation (4.2).

Detailed explanation of the dc-link voltage balancing controller using PI current controllers in anti-synchronous reference frame is postponed for Section 4.4. The d -axis current reference (i_{ds}^*) is set at a constant value to provide the rated rotor flux and the q -axis current reference (i_{qs}^*) is provided by either a maximum power point tracking (MPPT) controller, based on the optimal torque control method (Wu *et al.*, 2011) when operating as a generator, or by a PI speed controller in motoring mode. It is worth mentioning here that the dead-time compensator proposed in Chapter 3 is not used here for simplicity. Since the dc-link practically decouples the grid-side converter from the machine-side converters and the total dc-link voltage is controlled by the grid side converter, the grid-side converter can be conveniently represented by a controllable current source in the simulation (and a constant voltage supply in the experiment). The current source (voltage supply) only operates to maintain the overall dc-link voltage at a constant level, and will therefore not be discussed in detail here.

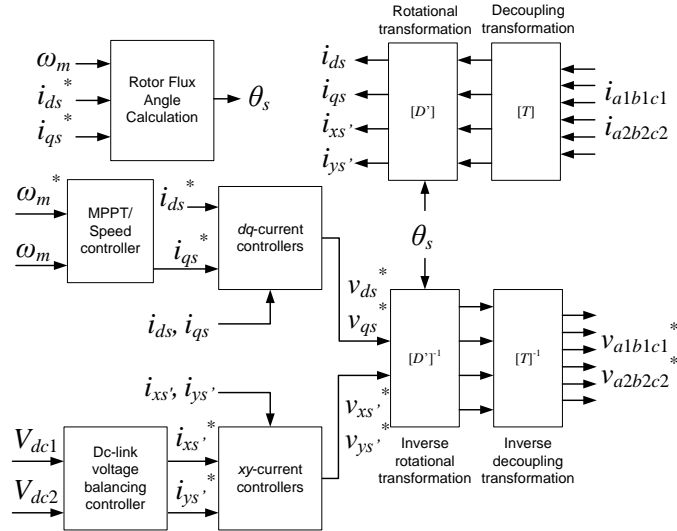


Fig. 4.2. General structure of the machine-side controllers.

4.3. Analysis of Series-Converter Topology

4.3.1. Merits and Demerits of the Topology

The topology of Fig. 4.1(c) combines an asymmetrical six-phase induction machine with cascaded machine-side converters. The series connection of the

converters elevates the dc-link voltage, thus reducing the current rating and losses for a given dc-link voltage level. In generating mode, the higher generating voltage also eases the step-up voltage process to the transmission level.

The cascaded dc-links also allow supplying each set of three-phase windings with halved dc-link voltage (Fig. 4.1(c)). This lowers the dc-link voltage ($V_{dc1} = V_{dc1} = V_{dc}/2$) and allows the use of switching devices with lower voltage ratings. The reduced dc-link voltage also halves the dv/dt of the common-mode voltage (CMV) for each winding, which now has steps of $V_{dc1}/3 = V_{dc}/6$, compared to the value of $V_{dc}/3$ in three-phase machines, for a given V_{dc} value.

As with other transformerless converter topologies (Yuan *et al.*, 2012; Olsen *et al.*, 2012), one major challenge for this topology is the machine's insulation requirement. In this topology, the upper and lower dc-link voltages (referenced to the dc-link midpoint) are $V_{dc}/2$ and 0 for VSC1 and 0 and $-V_{dc}/2$ for VSC2. Hence, while the voltage within each set of three-phase windings is restricted to $V_{dc}/2$, the voltage stress between the two sets of windings can reach V_{dc} .

Nevertheless, not all parts of the machine are subjected to this maximum voltage stress. In particular, the voltage difference between neutral points of the two sets of windings actually varies depending on the switching state, as summarised in Table 4.1. Switching states are expressed in decimal form of the six digit binary number $S_{a1} S_{b1} S_{c1} S_{a2} S_{b2} S_{c2}$, where S_i denotes the switching condition of the converter leg for phase i , with 0 indicating the bottom switch turned on and 1 indicating the top switch turned on. Redundant states are given in bold.

As shown in Table 4.1, the neutral-to-neutral voltage varies from 0 to as high as V_{dc} , depending on the switching state. By selecting a suitable PWM method, this voltage can be limited to lower values. PWM methods that use the switching state 56 (111000), as does the 24-sector SVPWM (Marouani *et al.*, 2008), should be avoided, as they exert

large voltage stress (V_{dc}) on the windings. The PWM using double zero-sequence injection (Bojoi *et al.*, 2002) is used throughout this paper, in both simulations and experiments, since this method does not apply switching state 56 (111000). As a matter of fact, only switching states that produce 0.333, 0.5 and 0.667 V_{dc} are used in this PWM method, as it will be seen later in the experimental results. The presence of redundant states suggests the possibility of further reducing the voltage stress using special space vector PWM techniques which restrict selection of certain switching states (Duran *et al.*, 2013). This is however beyond the scope of this study and is not discussed further.

Table 4.1. Neutral-to-neutral voltage for different switching states.

Neutral-to-neutral voltage (p.u. of V_{dc})	Switching states
1.0	56(111000)
0.833	24(011000), 40(101000), 48(110000), 57(111001), 58(111010), 60(111100)
0.667	8(001000), 16(010000), 25(011001), 26(011010), 28(011100), 32(100000), 41(101001), 42(101010), 44(101100), 49(110001), 50(110010), 52(110100), 59(111011), 61(111101), 62(111110)
0.500	0(000000), 9(001001), 10(001010), 12(001100), 17(010001), 18(010010), 20(010100), 27(011011), 29(011101), 30(011110), 33(100001), 34(100010), 36(100100), 43(101011), 45(101101), 46(101110), 51(110011), 53(110101), 54(110110), 63(111111)
0.333	1(000001), 2(000010), 4(000100), 11(001011), 13(001101), 14(001110), 19(010011), 21(010101), 22(010110), 31(011111), 35(100011), 37(100101), 38(100110), 47(101111), 55(110111)
0.167	3(000011), 5(000101), 6(000110), 15(001111), 23(011111), 39(110111)
0	7(000111)

Since not every part of the machine winding requires the insulation to withstand the maximum voltage stress of V_{dc} , it is possible to relax the insulation requirements by a proper machine design. For instance, slot sharing between conductors from different sets of windings should be avoided. Hence, as noted, even though the insulation requirement is high, it can be comparatively less than in a similar machine designed with phase voltage rating based on full V_{dc} voltage.

4.3.2. Dc-Link Voltage Drift

In the considered topology, the dc-link midpoint at the machine side is not accessible by the grid-side converter any more, while the total dc-link voltage control is

performed by the grid-side converter. There is no guarantee whatsoever that the dc-link voltages (V_{dc1} and V_{dc2} in Fig. 4.1(c)) will always be balanced. It is thus necessary to control the dc-link voltages at the machine side using the machine-side converters, to avoid dc-link voltage drift. In order to analyse the dc-link voltage balancing issue, the system is simplified by representing each VSC as a controlled current source, as shown in Fig. 4.3.

By using Kirchhoff's current law for points W and Z, the machine-side converters' currents can be written as:

$$I_{dc1} = -I_{dc3} - I_{cap1} \quad I_{dc2} = -I_{dc3} - I_{cap2} \quad (4.11)$$

The currents I_{dc1} and I_{dc2} consist of two components: a common component ($-I_{dc3}$) and a differential component (I_{cap1} and I_{cap2}). At any time instant, the common current component will be drawn from both the machine-side converters, while the instantaneous difference between the converters' currents and the common current will be supplemented by each of the converter's capacitors. Ideally, the two sets of machine windings are identical, so the average converter current should be the same despite the spatial difference. The average capacitor currents should thus also be the same.

The dc-link voltage balancing depends on the active power balancing between the two converters. The equations for the active power of the machine-side converters are:

$$\begin{aligned} P_1 &= I_{dc1} V_{dc1} \\ P_2 &= I_{dc2} V_{dc2} \end{aligned} \quad (4.12)$$

During steady state, the average converters' currents will be equal. Hence,

$$\frac{P_1}{P_2} = \frac{V_{dc1}}{V_{dc2}} \quad (4.13)$$

If the grid-side converter provides perfect control, the total dc-link voltage will be maintained at a constant value of V_{dc} . Each individual dc-link voltage is expressed as

a sum of its ideal balanced value ($V_{dc}/2$) and a deviation from the ideal value (ΔV_{dc1} and ΔV_{dc2}). Since the sum of two dc-link voltages is equal to V_{dc} , the voltage deviations must be equal but of opposite sign, i.e. $\Delta V_{dc1} = -\Delta V_{dc2}$. Hence the power equation (4.13) can be written as:

$$\frac{P_1}{P_2} = \frac{(V_{dc}/2) + \Delta V_{dc1}}{(V_{dc}/2) - \Delta V_{dc1}} \quad (4.14)$$

Rearranging (4.14), the voltage deviation can be expressed as a function of the active powers:

$$\Delta V_{dc1} = \left(\frac{P_1 - P_2}{P_1 + P_2} \right) \frac{V_{dc}}{2} \quad (4.15)$$

From (4.15) it follows that any asymmetry in the system will cause dc-link voltage drifting unless some voltage balancing mechanism is included in the control scheme.

4.4. Dc-Link Voltage Balancing Control

4.4.1. Dc-Link Voltage Balancing Using x - y Currents

Based on the analysis in Section 4.3, it is obvious that additional control needs to be provided by the machine-side converters to ensure the dc-link voltages are always balanced.

This can be achieved using the additional degrees of freedom provided by the x - y currents, so that the torque and flux production of the machine remains unaffected. Since the dc-link voltage unbalance is found to be a result of active power imbalance, it is necessary to first identify the relation between the x - y currents and the active power difference between the two windings. With the VSD model, the quantities in the two pairs of windings are not related, while the powers of the two three-phase windings now need to be controlled separately. In order to achieve separate power control with the

VSD model, it is insightful to at first establish the relationship between d - q - x - y components in the VSD model and the d_1 - q_1 - d_2 - q_2 components in the double- dq model, already considered in Chapter 3, which enables separate formulation of winding powers.

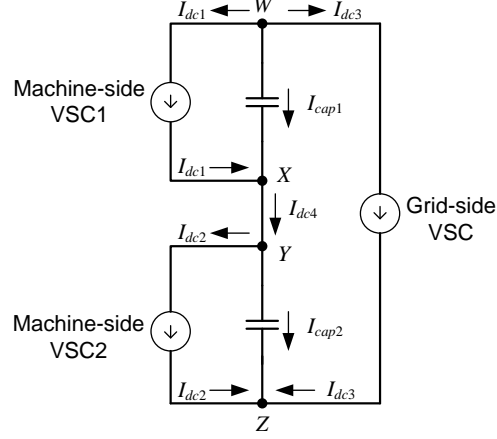


Fig. 4.3. Simplified circuit diagram for generation system with series-connected dc-links.

By applying equation (3.1) - (3.4) from Chapter 3 onto the stator currents, the stator currents based on double- dq model can be obtained as:

$$\begin{aligned}
 i_{\alpha s1} &= \sqrt{\frac{2}{3}} \left(i_{\alpha s1} - \frac{1}{2} i_{\beta s1} - \frac{1}{2} i_{\gamma s1} \right) \\
 i_{\alpha s2} &= \sqrt{\frac{2}{3}} \left(\frac{\sqrt{3}}{2} i_{\alpha s2} - \frac{\sqrt{3}}{2} i_{\beta s2} \right) \\
 i_{\beta s1} &= \sqrt{\frac{2}{3}} \left(\frac{\sqrt{3}}{2} i_{\beta s1} - \frac{\sqrt{3}}{2} i_{\gamma s1} \right) \\
 i_{\beta s2} &= \sqrt{\frac{2}{3}} \left(\frac{1}{2} i_{\alpha s2} + \frac{1}{2} i_{\beta s2} - i_{\gamma s2} \right)
 \end{aligned} \tag{4.16}$$

Comparison of (4.16) with (4.1) shows that:

$$\begin{aligned}
 i_{\alpha s} &= \sqrt{\frac{1}{2}} (i_{\alpha s1} + i_{\alpha s2}) & i_{\beta s} &= \sqrt{\frac{1}{2}} (i_{\beta s1} + i_{\beta s2}) \\
 i_{\gamma s} &= \sqrt{\frac{1}{2}} (i_{\alpha s1} - i_{\alpha s2}) & i_{\gamma s} &= \sqrt{\frac{1}{2}} (-i_{\beta s1} + i_{\beta s2})
 \end{aligned} \tag{4.17}$$

This is in essence the same as (3.7), but for the specific case of stator currents.

For control purposes, it is more useful to have the control variables in the d - q synchronous reference frame, so that they appear as dc quantities and can hence be easily dealt with using PI controllers. As discussed in Chapter 3, the frame of reference has significant effect on this matter, and is investigated here.

For the double- dq model, the currents in the synchronously rotating frame are:

$$\begin{aligned}
i_{ds1} &= i_{\alpha s1} \cos \theta_s + i_{\beta s1} \sin \theta_s \\
i_{ds2} &= i_{\alpha s2} \cos \theta_s + i_{\beta s2} \sin \theta_s \\
i_{qs1} &= -i_{\alpha s1} \sin \theta_s + i_{\beta s1} \cos \theta_s \\
i_{qs2} &= -i_{\alpha s2} \sin \theta_s + i_{\beta s2} \cos \theta_s
\end{aligned} \tag{4.18}$$

For the VSD model, using the conventional rotational transformation defined in (4.2), the following is obtained:

$$\begin{aligned}
i_{ds} &= \sqrt{1/2}(i_{ds1} + i_{ds2}) \\
i_{qs} &= \sqrt{1/2}(i_{qs1} + i_{qs2}) \\
i_{xs} &= \sqrt{1/2}[(i_{ds1} - i_{ds2})\cos \theta_s - (i_{qs1} - i_{qs2})\sin \theta_s] \\
i_{ys} &= \sqrt{1/2}[(-i_{ds1} + i_{ds2})\sin \theta_s + (-i_{qs1} + i_{qs2})\cos \theta_s]
\end{aligned} \tag{4.19}$$

As can be seen from (4.19), the resulting x - y components are not dc quantities. Hence, an alternative transformation matrix is introduced,

$$[D'] = \begin{matrix} d \\ q \\ x' \\ y' \end{matrix} \begin{bmatrix} \cos \theta_s & \sin \theta_s & & \\ -\sin \theta_s & \cos \theta_s & & \\ & & \cos \theta_s & -\sin \theta_s \\ & & \sin \theta_s & \cos \theta_s \end{bmatrix} \tag{4.20}$$

which rotates the x - y components in the inverse (anti-) synchronous direction. With this alternative rotational transformation, a more suitable form of x - y components (denoted as x' - y' components) can be obtained:

$$\begin{aligned}
i_{ds} &= \sqrt{1/2}(i_{ds1} + i_{ds2}) \\
i_{qs} &= \sqrt{1/2}(i_{qs1} + i_{qs2}) \\
i_{xs'} &= \sqrt{1/2}(i_{ds1} - i_{ds2}) = \sqrt{1/2}\Delta i_{ds} \\
i_{ys'} &= \sqrt{1/2}(i_{qs2} - i_{qs1}) = -\sqrt{1/2}\Delta i_{qs}
\end{aligned} \tag{4.21}$$

Transformed x' - y' components are now both dc signals and represent the difference between the d - q components of the two windings. Controlling $i_{xs'}$ to be positive will make i_{ds1} greater than i_{ds2} , while positive $i_{ys'}$ makes i_{qs1} smaller than i_{qs2} , and vice versa. Thus, power drawn from the two windings can be controlled by the proper injection of $i_{xs'}$ - $i_{ys'}$ currents. Moreover, since the d - q components are dc quantities, x' - y' components will also be dc quantities, which allows the use of simple

PI controllers. It is also worth noting that, from (4.21), injecting $i_{xs}'-i_{ys}'$ changes the difference between $i_{ds1}-i_{qs1}$ and $i_{ds2}-i_{qs2}$ but does not change the overall flux and torque currents ($i_{ds}-i_{qs}$). Hence the injection of $i_{xs}'-i_{ys}'$ currents will not affect the overall operation of the machine.

During generation, active power is injected into the dc-link and the torque current is negative (assuming positive rotational direction). When ΔV_{dc1} is positive, Δi_{qs} should be positive to reduce the power injected by the VSC1, and vice versa. Hence, the dc-link voltage balancing controller can be constructed using a PI controller with ΔV_{dc1} as input. Since i_{ys}' and Δi_{qs} have opposite polarity, the output of the PI controller should be inverted (multiplied by -1), as in Fig. 4.4.

4.4.2. Voltage Balancing in Motoring Mode

The derivation of the dc-link voltage balancing controller has been based on the machine operation in the generating mode. The applicability of the same controller structure in the motoring mode is therefore addressed here.

During motoring operation in positive rotational direction, the machine consumes active power from the dc-link and the torque producing current is positive. When ΔV_{dc1} is positive, positive Δi_{qs} should be imposed so that VSC1 consumes more active power than VSC2, and thus reduces ΔV_{dc1} . Since Δi_{qs} again has the same polarity as ΔV_{dc1} , the same controller structure can be applied during motoring mode as well.

When the machine rotates in the negative direction in motoring mode, the sign of torque producing current becomes negative. In this case, positive ΔV_{dc1} requires a negative Δi_{qs} for voltage balancing. For the proper operation of the dc-link voltage balancing controller, the negative sign in Fig. 4.4 will have to be replaced by a positive sign. This consideration does not apply in generation, since the rotation of a generator is usually confined to a single direction.

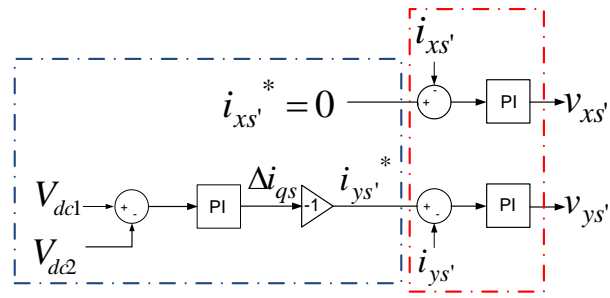


Fig. 4.4. Structure of the x' - y' current controllers (dotted box on the right) and dc-link voltage balancing controller (dotted box on the left).

4.5. Simulation and Experimental Results

In order to verify the dc-link voltage balancing controller performance, experimental tests are conducted on a low-power asymmetrical six-phase induction machine mentioned in Chapter 3. The six-phase machine is configured with two isolated neutral points. Each of the two three-phase windings is connected to a custom-made multiphase two-level VSC, configured for three-phase operation. The dc-links of the two VSCs are cascaded in series, and connected to a dc-power supply (Sorensen SGI 600-25) which maintains the overall dc-link voltage at 300 V. A 7.5 kW dc machine is coupled to the six-phase machine and is controlled using ABB DCS800 in torque mode to provide loading of the six-phase machine.

The whole control algorithm for the six-phase machine is implemented using dSpace DS1006 system. Switching frequency of 5 kHz and current sampling frequency of 10 kHz are used. Dead time of 6 μ s is integrated in the VSC hardware. Machine phase currents and dc-link voltages are measured (using the LEM sensors embedded in the VSCs) through dSpace DS2004 ADC module and displayed on oscilloscope via the dSpace DS2101 DAC module. Hence the current traces shown later are the filtered current waveforms, without the switching ripples. Overall configuration of the experimental setup is shown in Fig. 4.5 and the detailed list of converter and control parameters is given in Table 4.2 (machine and converter parameters are as in Table 3.1).

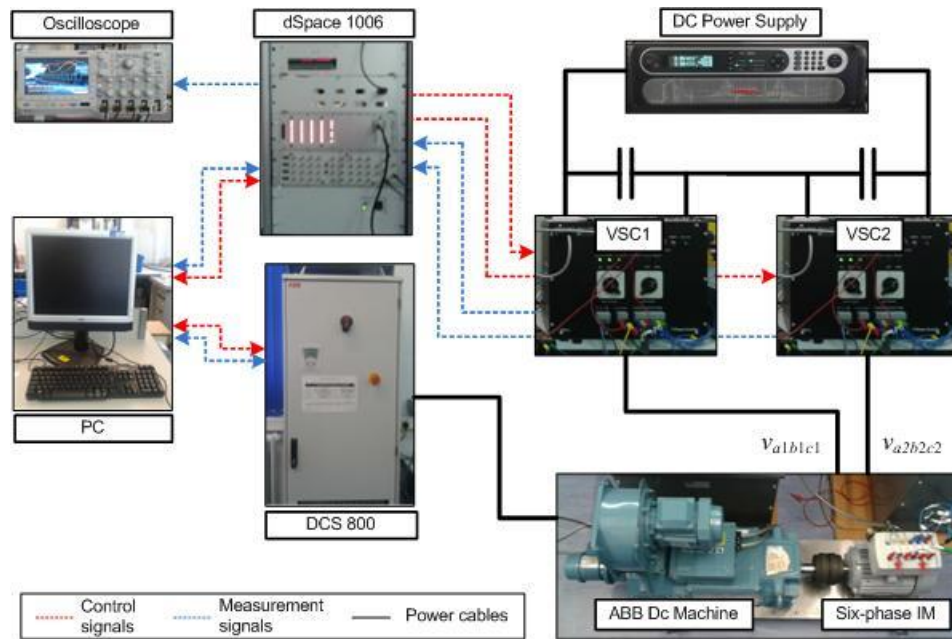


Fig. 4.5. Experimental setup for the series-converter topology in motoring mode.

Table 4.2 Experiment and simulation parameters.

Controller Parameters		
$f_{switching} = 5 \text{ kHz}$	$f_{sampling} = 10 \text{ kHz}$	
<i>d-q</i> current controllers:	$K_p = 60$	$K_i = 8000$
<i>x'-y'</i> current controllers:	$K_p = 50$	$K_i = 2500$
Speed controller:	$K_p = 0.02$	$K_i = 0.02$
Dc-link voltage balancing controller:	$K_p = 1.0$	$K_i = 2.0$

Due to the lack of means for grid connection, experimental results apply only to operation in the motoring mode. However, as maintained from the beginning, and as discussed in Section 4.4, the capacitor voltage balancing controller is of the same structure in both motoring and generating applications. All the parameters used for the simulation are identical to those in the experimental setup (except for the machine's inertia and machine's inherent asymmetries, which were obtained via trial and error for simulation purpose).

In what follows the experimental results are shown first, together with Matlab/Simulink simulation results, for the motoring mode of operation. The study is then complemented with simulation results for the generating mode.

4.5.1. Experimental Verification in the Motoring Mode

The machine is controlled in motoring mode, using IRFOC with closed-loop speed control. Only the *d-q* current controllers are initially used, without any *x-y* current

control (x - y voltage references are set to zero). Fig. 4.6 shows the experimental results when the machine operates at 500 rpm without load.

The dc-link voltages are not equal due to the inherent asymmetries that exist in the converters and the machine. VSC2 is driven into saturation (over-modulation region) by the low dc-link voltage and produces low order harmonics in phase voltages, which cause flow of x - y currents. The uncontrolled x - y currents produce additional power losses and distort the current waveform, causing the difference in the amplitudes of the currents in windings 1 and 2.

The same operating condition is simulated using Matlab/Simulink and the results are shown in Fig. 4.7. Inherent asymmetry in the machine/converter is emulated by adding external resistance $R_{external} = 2.8\Omega$ in phases $a1b1c1$ (the value was found via trial and error, so that a close agreement with the experimental findings is obtained). Other than the value of $R_{external}$, all parameters used in the simulation are identical to those used in the actual experiment. The simulated currents closely resemble the experimental results, confirming the accuracy of the simulator.

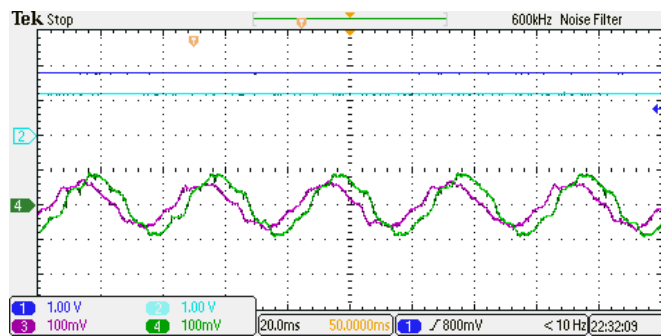


Fig. 4.6. Experimental results for no-load operation at 500 rpm, with only d - q current controllers: Channel 1: V_{dc1} (100V/div), Channel 2: V_{dc2} (100V/div), Channel 3: phase- $a1$ current (1A/div), Channel 4: phase- $a2$ current (1A/div), Horizontal: Time (20ms/div). (Note that markers for Channels 1 and 3 have been overlapped by markers for Channels 2 and 4, respectively).

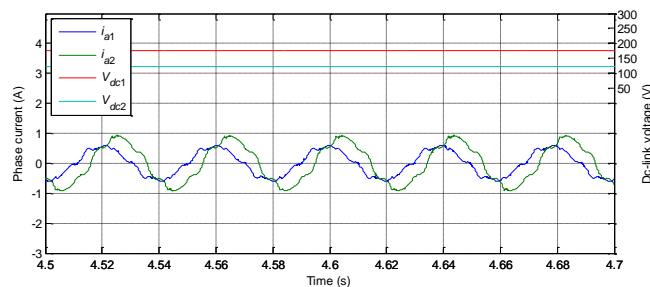


Fig. 4.7. Simulation results for no-load operation at 500 rpm, with only d - q current controllers.

The same test is repeated for the machine running at 250 rpm, when a larger dc-link voltage drift is observed. Fig. 4.8 shows the experimental results where the phase currents are more distorted than in the previous case, because VSC2 is in deeper saturation due to the larger dc-link voltage imbalance. Again, simulated results in Fig. 4.9 show good correlation with the experimental findings.

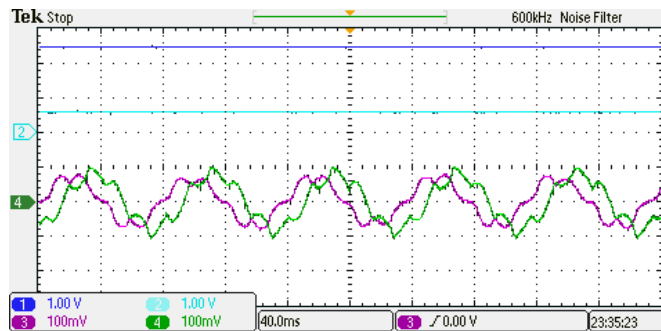


Fig. 4.8. Experimental results for no-load operation at 250 rpm, with only d - q current controllers: Channel 1: V_{dc1} (100V/div), Channel 2: V_{dc2} (100V/div), Channel 3: phase- $a1$ current (1A/div), Channel 4: phase- $a2$ current (1A/div), Horizontal: Time (20ms/div). (Markers for Channels 1 and 3 have been overlapped by markers for Channels 2 and 4, respectively).

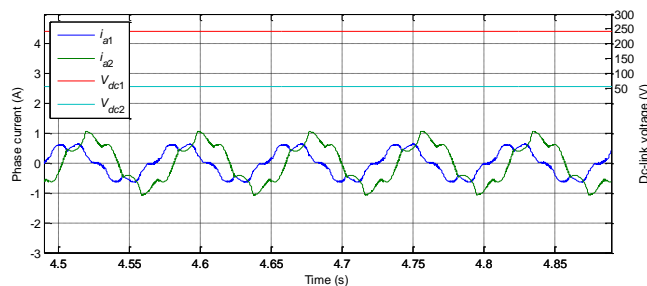


Fig. 4.9. Simulation results for no-load operation at 250 rpm, with only d - q current controllers.

Figs. 4.10 and 4.11 show the experimental and simulation results when anti-synchronous PI x '- y ' current controllers are activated with x '- y ' current references set to zero. Since one of the VSCs is now in saturation, the x '- y ' current controllers, which are designed to operate in the linear modulation region, are unable to fully suppress the x '- y ' currents and only a slight improvement in terms of the current distortion is obtained. Dc-link voltages remain unbalanced in this case, since the active powers consumed by the two VSCs are still not balanced.

Figs. 4.12 and 4.13 show the activation of dc-link voltage balancing controller at $t = 1.0$ s ($t = 5.0$ s in Fig. 4.13), when the machine is running at 500 rpm without load. As predicted by the theoretical considerations, the dc-link voltages converge and stay balanced after the activation of the controller. Figs. 4.14 and 4.15 show that the currents

for phases $a1$ and $a2$ become much more balanced and are less distorted because the x - y currents are now under control and the dc-link voltages are controlled to achieve VSC operation in the linear region. Slight distortion is still observable due to the dead-time effect of the converter. The same procedure is repeated for operation at 250 rpm without load, Figs. 4.16 and 4.17. A slower convergence is observed, since the same controller gains and limits are used, while the dc-link voltage difference is now larger.

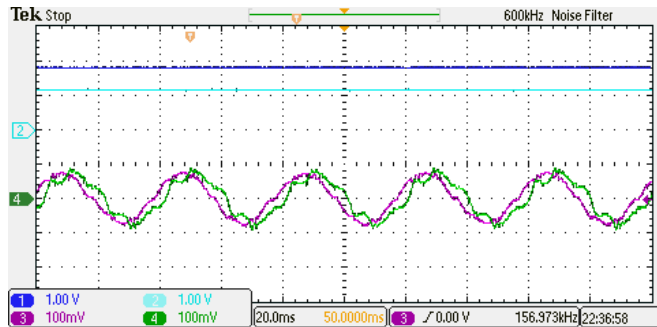


Fig. 4.10. Experimental results for no-load operation at 500 rpm, with d - q and x '- y ' current controllers activated: Channel 1: V_{dc1} (100V/div), Channel 2: V_{dc2} (100V/div), Channel 3: phase- $a1$ current (1A/div), Channel 4: phase- $a2$ current (1A/div), Horizontal: Time (20ms/div). (Markers for Channels 1 and 3 have been overlapped by markers for Channels 2 and 4, respectively).

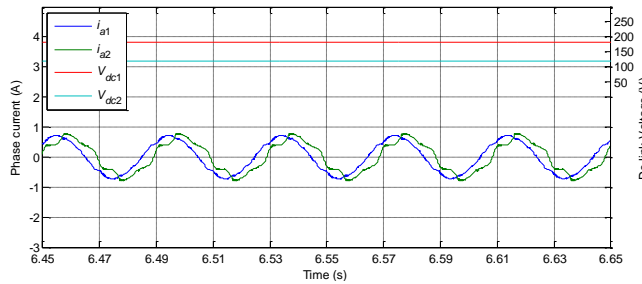


Fig. 4.11. Simulation results for no-load operation at 500 rpm, with d - q and x '- y ' current controllers activated.

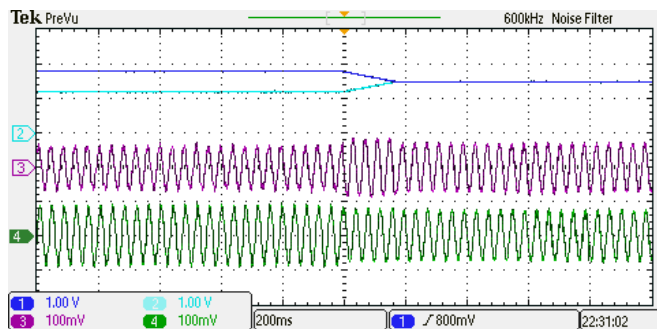


Fig. 4.12. Experimental results for no-load operation at 500 rpm, showing the activation of the dc-link voltage balancing controller at $t = 1.0$ s: Channel 1: V_{dc1} (100V/div), Channel 2: V_{dc2} (100V/div), Channel 3: phase- $a1$ current (1A/div), Channel 4: phase- $a2$ current (1A/div), Horizontal: Time (200ms/div). (Markers for Channels 1 and 2 are overlapped).

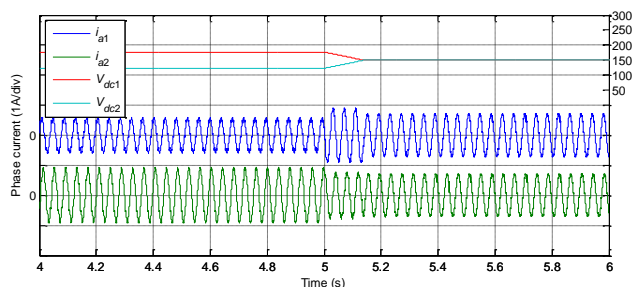


Fig. 4.13. Simulation results for no-load operation at 500 rpm, showing the activation of the dc-link voltage balancing controller at $t = 5.0$ s.

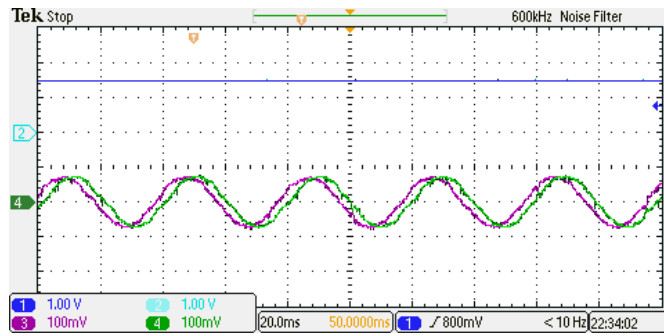


Fig. 4.14. Experimental results for no-load operation at 500 rpm, with dc-link voltage balancing controller activated: Channel 1: V_{dc1} (100V/div), Channel 2: V_{dc2} (100V/div), Channel 3: phase- $a1$ current (1A/div), Channel 4: phase- $a2$ current (1A/div), Horizontal: Time (20ms/div). (Markers for Channels 1 and 3 have been overlapped by markers for Channels 2 and 4, respectively).

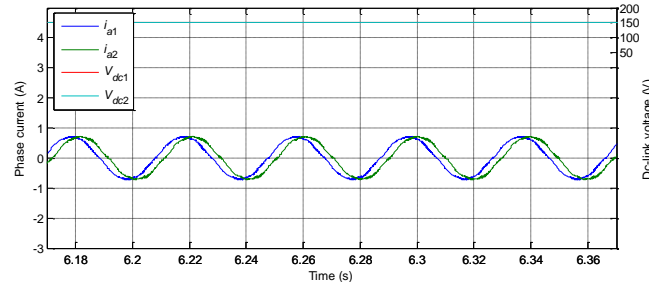


Fig. 4.15. Simulation results for no-load operation at 500 rpm, with dc-link voltage balancing controller activated (V_{dc1} and V_{dc2} are overlapped).

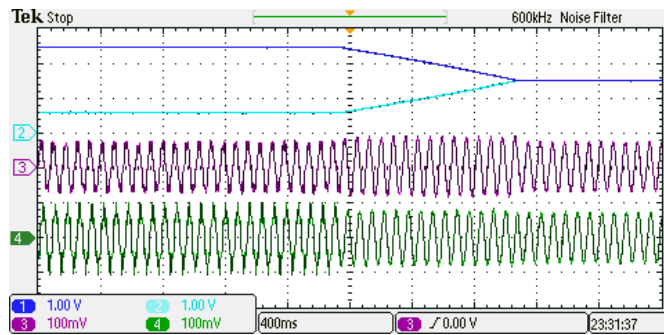


Fig. 4.16. Experimental results for no-load operation at 250 rpm, showing the activation of dc-link voltage balancing controller at $t = 1.0$ s: Channel 1: V_{dc1} (100V/div), Channel 2: V_{dc2} (100V/div), Channel 3: phase- $a1$ current (1A/div), Channel 4: phase- $a2$ current (1A/div), Horizontal: Time (400ms/div). (Markers for Channels 1 and 2 are overlapped).

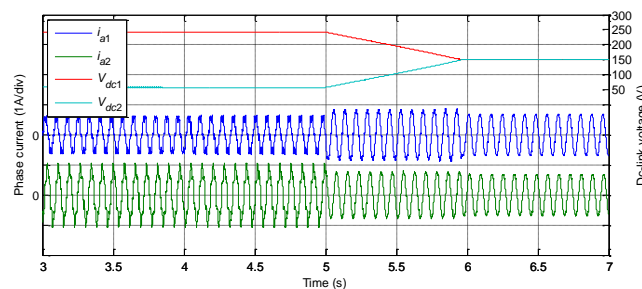


Fig. 4.17. Simulation results for no-load operation at 250 rpm, showing the activation of dc-link voltage balancing controller at $t = 5.0$ s.

Next, the performance of the dc-link voltage balancing controller is evaluated with the machine in variable-speed operation. Fig. 4.18 shows the performance of the dc-link voltage balancing controller when the speed reference increases from 100 rpm to 250 rpm at $t = 1.2$ s, and then to 500 rpm at $t = 2.2$ s ($t = 4.2$ s and $t = 5.2$ s in the corresponding simulation study in Fig. 4.19). It is evident that the dc-link voltages are

kept at equal values during the whole transient operation. Performance of the system under sudden load torque variation is also evaluated in Figs. 4.20 and 4.21. A torque command is first given to the DCS800, such that the dc-machine provides 0.5 p.u of the rated torque to the six-phase machine. Using IRFOC, the six-phase machine is able to maintain the speed at 250 rpm. At $t = 1.6$ s ($t = 4.6$ s in Fig. 4.21), the load torque is removed by reducing the torque command to zero. A speed overshoot is observed together with the current amplitude reduction, as a result of the load torque variation. Nevertheless, the dc-link voltages are kept at equal values throughout this process, showing that the dc-link voltage balancing controller is unaffected by the sudden load torque variation.

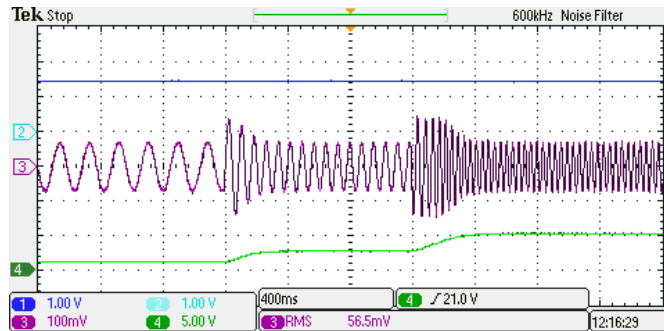


Fig. 4.18. Experimental results for speed variation from 100rpm to 250rpm to 500rpm under no-load conditions with dc-link voltage balancing controller activated: Channel 1: V_{dc1} (100V/div), Channel 2: V_{dc2} (100V/div), Channel 3: phase- $a1$ current (1A/div), Channel 4: speed (500rpm/div), Horizontal: Time (400ms/div). (Markers for Channels 1 and 2 are overlapped).

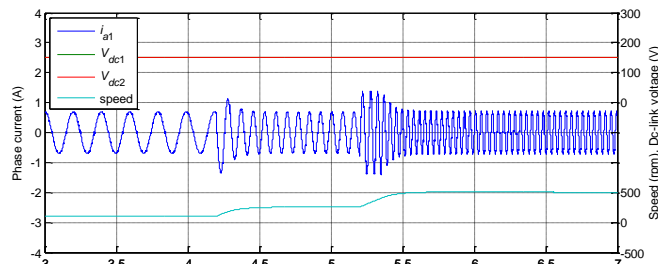


Fig. 4.19. Simulation results for speed variation from 100 rpm to 250 rpm to 500 rpm (V_{dc1} and V_{dc2} are overlapped).

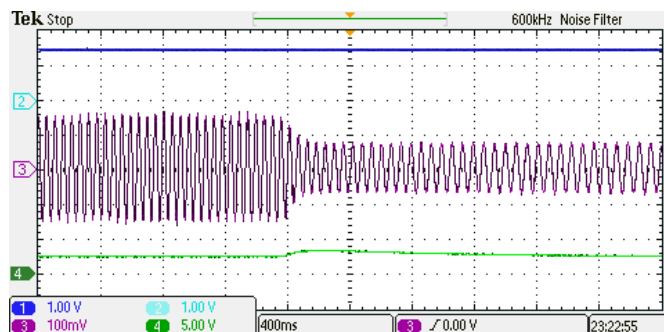


Fig. 4.20. Experimental results for machine unloading at 250 rpm, with dc-link voltage balancing controller activated: Channel 1: V_{dc1} (100V/div), Channel 2: V_{dc2} (100V/div), Channel 3: phase- $a1$ current (1A/div), Channel 4: speed (500rpm/div), Horizontal: Time (400ms/div). (Markers for Channels 1 and 2 are overlapped).

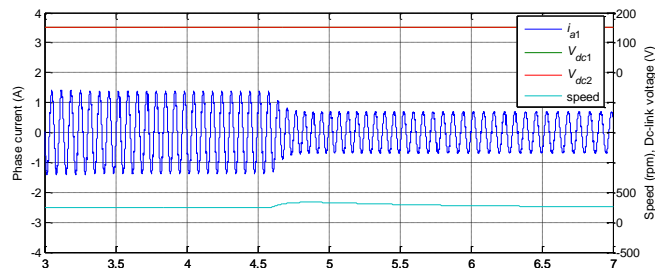


Fig. 4.21. Simulation results for machine unloading at 250 rpm, with dc-link voltage balancing controller activated (V_{dc1} and V_{dc2} are overlapped).

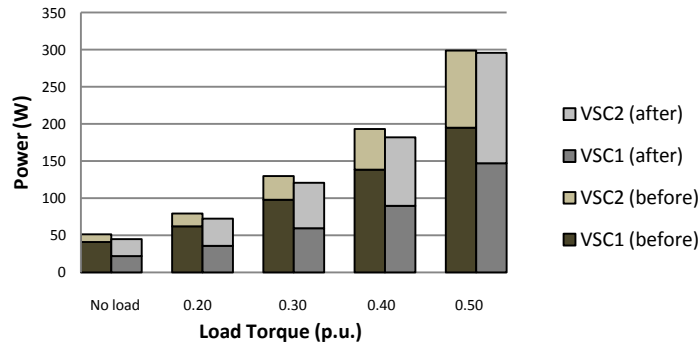


Fig. 4.22. Comparison of active powers, consumed by each VSC, before (left bars) and after (right bars) activation of the dc-link voltage balancing controller, when the machine operates at 250 rpm with different load torque.

Based on (4.15), it is obvious that the dc-link unbalance is a result of power unbalance between the two windings. Fig. 4.22 shows the comparison of active power supplied to VSC1 and VSC2 before and after the activation of dc-link voltage balancing controller. The results show that the power consumed by each VSC (and hence each winding of the machine) is highly unbalanced before compensation. The compensation restores power balance between the two VSCs. This is accompanied by a slight reduction of total power, which is due to the reduction of loss producing harmonics associated with the saturation of one of the VSCs under unbalanced capacitor voltage. The imbalance in powers, apart from causing unbalanced capacitor voltages, may also require derating of the machine to avoid overloading of one of the windings/converters.

It is worth noting that the unbalance is in this case caused by inherent asymmetries in the machine windings/converters, manifested in the form of small differences in the per-phase resistances. As the load increases, the difference in RI^2 power losses in these resistances becomes marginal; hence power unbalance decreases with increasing load torque.

4.5.2. Operation at Lower Switching Frequency

The experimental results given so far were obtained for 5 kHz switching frequency. Since the topology is aimed at high power applications, experimental results for the operation of the system with a lower switching frequency of 1 kHz are presented next. Operating conditions are the same as for 5 kHz switching frequency, except that the PI controller gains have been reduced to ensure stable operation. Fig. 4.23 shows the

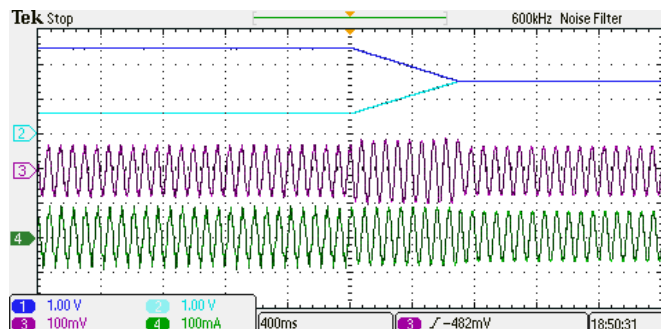


Fig. 4.23. Experimental results for no-load operation at 250 rpm showing the activation of dc-link voltage balancing controller at $t = 1.0\text{s}$ (switching frequency = 1 kHz): Channel 1: V_{dc1} (100V/div), Channel 2: V_{dc2} (100V/div), Channel 3: phase- $\alpha 1$ current (1A/div), Channel 4: phase- $\alpha 2$ current (1A/div), Horizontal: Time (400ms/div). (Markers for Channels 1 and 2 are overlapped).

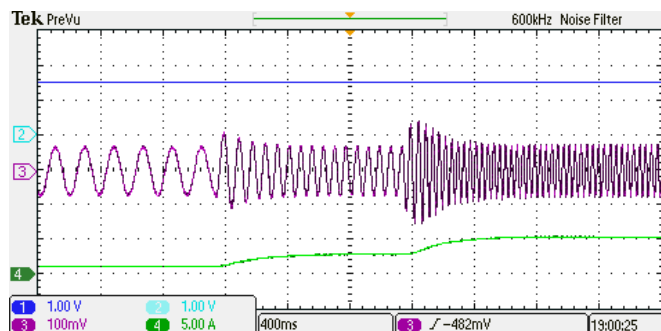


Fig. 4.24. Experimental results for speed variation from 100rpm to 250rpm to 500rpm under no-load conditions with dc-link voltage balancing controller activated (switching frequency = 1 kHz): Channel 1: V_{dc1} (100V/div), Channel 2: V_{dc2} (100V/div), Channel 3: phase- $\alpha 1$ current (1A/div), Channel 4: speed (500rpm/div), Horizontal: Time (400ms/div). (Markers for Channels 1 and 2 are overlapped).

activation of the dc-link voltage balancing controller and Fig. 4.24 shows the operation of the system under varying speed. While the dynamics of the system differ slightly, the results show that the dc-link voltage controller can still balance the dc-link voltage despite the reduction in the switching frequency.

4.5.3. Experimental Results – CMV and Neutral-to-Neutral Voltage

This sub-section shows the experimental results for common-mode voltage and neutral-to-neutral voltage in the series-converter topology. The results are obtained for the motoring mode without load, with dc-link voltage balancing controller activated.

The overall dc-link voltage is 300 V. Fig. 4.25 shows the common-mode voltage for winding 1. This voltage is measured as the neutral point voltage of winding 1 with respect to the dc-link mid-point. Zoomed-in view of the voltage waveform shows that the CMV changes in steps of 50V ($V_{dc}/6$), which agrees with discussion in Section 4.3.

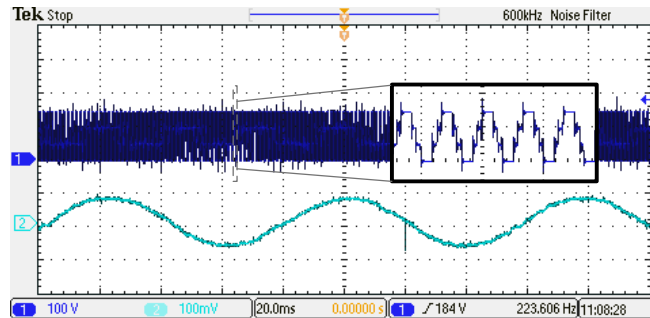


Fig. 4.25. Experimental results for the machine running at 250rpm without load with dc-link voltage balancing controller activated: Channel 1: CMV for winding 1 (100V/div), Channel 2: phase-a1 current (1A/div).

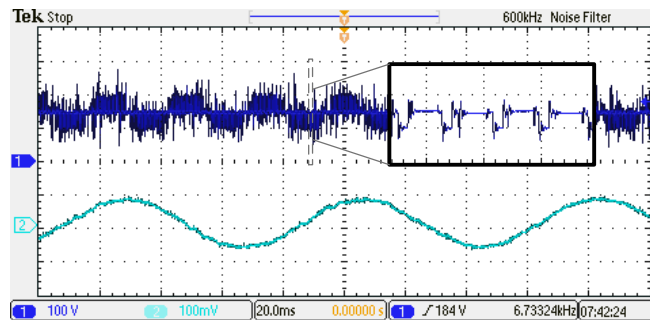


Fig. 4.26. Experimental results for the machine running at 250rpm without load with dc-link voltage balancing controller activated: Channel 1: Neutral-to-neutral voltage (100V/div), Channel 2: phase-a1 current (1A/div).

Fig. 4.26 shows the neutral-to-neutral voltage of the machine under the same operating condition. It is observed that the neutral-to-neutral voltage is around 0.333, 0.5 and 0.667 V_{dc} , since the PWM method used does not utilise states that give neutral-to-neutral voltage of 0, 0.166, 0.833 and 1.0 V_{dc} (as stated in Section 4.3). The dv/dt is also reduced since the steps are $V_{dc}/6$.

4.5.4. Simulations in Generating Mode

By comparing the experimental and simulation results presented in sub-section 4.5.1, it can be concluded that the Matlab/Simulink simulator gives an accurate representation of the actual system. Here, investigations using the same simulator are presented to verify the operation of the system in generating mode. In the simulation, the total dc-link voltage is maintained at 600 V and the generator is subjected to a

varying wind speed profile, shown in Fig. 4.27. All simulation results are shown from $t = 2.0$ s onwards, when the machine has reached a steady-state operating point at rated wind speed.

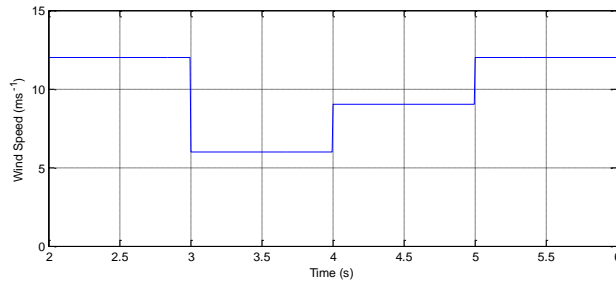


Fig. 4.27. Wind speed variation used for simulating the system in generating mode of operation.

An additional resistance $R_{external} = 2.8 \Omega$ is added again in phases $a1b1c1$ to emulate the winding asymmetry. Fig. 4.28 shows the unbalanced dc-link voltage when the generator is controlled using only the d - q current controllers, with no dc-link voltage balancing control. The phase currents under this operating condition are unbalanced, with current amplitudes in winding 1 lower than those in winding 2 (Fig. 4.29). This is the result of the non-zero x - y currents that, according to (4.21), lead to the current asymmetry. Since the voltage drift in this case is not severe enough to saturate the VSCs, the distortions in phase currents are less significant. Remaining distortion is caused by the uncontrolled x - y currents and the uncompensated dead-time effect.

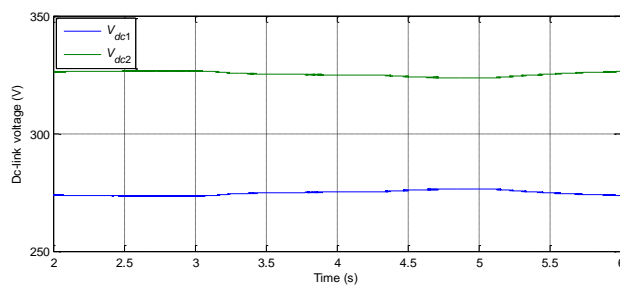


Fig. 4.28. Dc-link voltages under varying wind speed, with no dc-link voltage balancing controller.

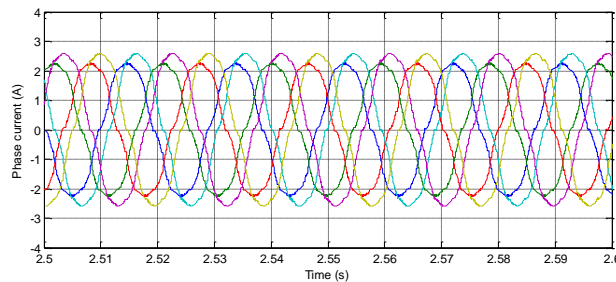


Fig. 4.29. Phase currents for generating operation without dc-link voltage balancing controller.

The same test is then repeated but with the dc-link voltage balancing controller activated. Fig. 4.30 shows that the dc-link voltages are now balanced and are kept at the equal level. The phase currents in Fig. 4.31 still show different amplitudes but now the currents in winding 1 are higher than those in the winding 2. This is so because, in order to achieve dc-link voltage balancing, more active power needs to be generated in winding 1 to compensate for the larger copper loss due to the additional resistance R . Even though the dc-link voltage balancing controller injects non-zero steady-state x - y currents, the amount of these circulating currents is lower than those in the previous case (with uncontrolled x - y currents) and this reduces the current waveform distortion. The injection of these steady-state x - y currents, caused by the generator asymmetries, produces additional stator winding losses. Fig. 4.32 shows the d - q currents under the varying wind speed conditions. The flux producing current is maintained at a constant level, while torque producing current is varied to follow the MPPT operation. The flux and torque operation of the generator is practically unaffected by the dc-link voltage balancing controller. The simulation results for the generating mode show that, with the dc-link voltage balancing controller, the generator is able to operate with proper flux and torque control.

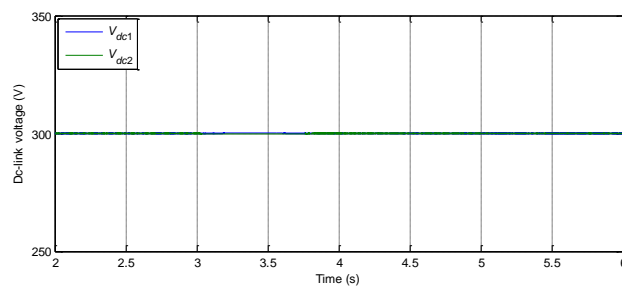


Fig. 4.30. Dc-link voltages under varying wind speed, with dc-link voltage balancing controller (V_{dc1} and V_{dc2} are overlapped).

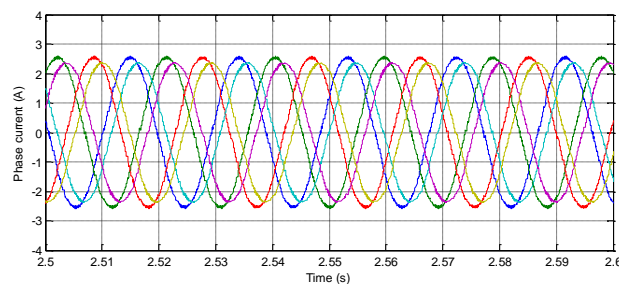


Fig. 4.31. Phase currents for generating operation with dc-link voltage balancing controller.

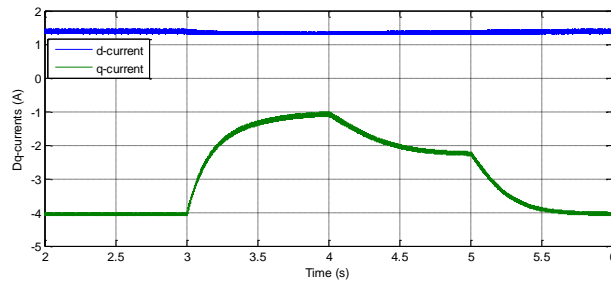


Fig. 4.32. D - q currents for generating operation with dc-link voltage balancing controller.

4.6. Conclusion

This chapter discusses the viability of an asymmetrical six-phase energy conversion system with cascaded machine-side converters and presents a method for the voltage balancing of the dc-link midpoint. The topology and the concept are equally applicable to both variable-speed drive and generation applications.

The series connection of the converters halves the individual dc-link voltages and the common-mode voltage's dv/dt . However, the voltage shifting between the two isolated neutral points can prevent the use of low voltage machines unless specific PWM techniques are employed. The system is believed to be well-suited to remote offshore wind farms with HVDC connection, where elevation of the dc-link voltage and the use of only two cables for the grid-side connection can reduce the overall infrastructure cost, but there is a potential problem with the drift of the dc-link midpoint voltage. This work overcomes this limitation by developing a dc-link voltage balancing controller that uses the x - y currents to unbalance the winding currents in order to balance the power sharing between the two sets of three-phase windings. This represents an entirely new way of exploiting the existence of additional degrees of freedom, available in multiphase machines, which has never been reported before. Simulation and experimental results confirm that it is possible to accurately control the dc-link midpoint voltage and to operate the machine in variable-speed mode in both motoring and generation.

Chapter 5

POST-FAULT CONTROL

5.1. Introduction

One of the most important advantages of a multiphase machine compared to its three-phase counter-part is its fault tolerant capability. Hence, a great amount of work has been dedicated to this area of the research, addressing different aspects of the topic. From the literature, it has been shown that better fault tolerance can be achieved via special machine design (Bianchi *et al.*, 2008; Barcaro *et al.*, 2010; Barcaro *et al.*, 2011; Vaseghi *et al.*, 2011), as well as through the use of power electronic converters with special topologies (Parker *et al.*, 2011; Ruba *et al.*, 2012; Wang *et al.*, 2012; Parker *et al.*, 2013). Nevertheless, the majority of research on fault tolerant control of multiphase machines focuses on the post-fault control of the most practical and common machine-converter topology, i.e. a star connected n -phase induction machine fed with n -leg VSC. The discussion presented in this chapter follows the latter, investigating the post-fault operation of an asymmetrical six-phase induction machine with star connected stator windings.

For a six-phase machine fed with a six-leg VSC, two common stator configurations are available: two three-phase windings with two isolated neutrals and single six-phase winding with single isolated neutral. For the two neutrals connection, the zero-sequence currents cannot flow. This reduces the number of controllable

currents and requires only four current controllers to fully control the machine. Thus, investigations on the control of six-phase machine are normally based on this configuration (Bojoi *et al.*, 2003b; Levi *et al.*, 2007a). Compared to the two neutrals case, single neutral point connection offers an extra degree of freedom since there are now five instead of four controllable currents. While this additional degree of freedom increases the number of required current controllers, it provides better controllability during fault. As a result, discussion of fault tolerant control of a six-phase machine usually uses this configuration (Zhao and Lipo, 1996a; Zhao and Lipo, 1996b; Kianinezhad *et al.*, 2008; Fnaiech *et al.*, 2010). To date, a unified discussion and comparison of the two configurations have not been reported.

Compared with the fault-tolerant control studies available in the literature, the study presented here seeks to provide additional contributions in the following aspects:

- 1) The post-fault control is derived using normal decoupling transformation, instead of the reduced order decoupling transformation (Zhao and Lipo, 1996a; Zhao and Lipo, 1996b; Ryu *et al.*, 2006; Kianinezhad *et al.*, 2008; Guzman *et al.*, 2011), which allows the use of the same controller structure as in the healthy operation. Such control has been discussed in (Locment *et al.*, 2008; Tani *et al.*, 2012), but not for an asymmetrical six-phase machine.
- 2) The effect of fault on the leg-to-phase voltage relation is investigated, and its influence on the performance of linear (PI) current controller is discussed. Subsequently, two different current control methods utilising dual PI controllers are compared.
- 3) Finally, a unified analysis of post-fault control of the six-phase machine, considering both single and two isolated neutrals, is presented. Results show that the same controller structure is applicable for both configurations, requiring only minor alterations. Quantitative comparisons between the two, in terms of the

achievable torque and stator winding losses under different modes of post-fault control, are presented as well.

The content of the chapter is organised in the following manner: Section 5.2 first discusses the effect of the single open-circuit fault on the machine equations. Here, full-order decoupling transformation is used, as opposed to the reduced order decoupling transformation. The machine equations form the basis on which the post-fault control is developed. Section 5.3 derives the current references for two modes of operation: minimum stator losses and maximum torque operation. Subsequently, the suitable current control methods, using PI controllers, are discussed in Section 5.4. Finally, Section 5.5 presents the experimental results for verification of the theoretical discussion presented in the earlier part of the chapter.

5.2. Machine Equations

Before deriving the current references and selecting the suitable current controller, it is first necessary to examine the effect of an open-circuit fault on the machine equations. As in the healthy case, the faulted machine should be described using a set of decoupled variables, by applying a suitable decoupling transformation on the machine equations. When one of the machine phases suffers from an open-circuit fault, the current in the faulted phase will be zero and the machine is considered to have lost one degree of freedom. To reflect this loss of degree of freedom, some works suggested the use of different reduced order decoupling transformations (Zhao and Lipo, 1996a; Zhao and Lipo, 1996b; Ryu *et al.*, 2006; Kianinezhad *et al.*, 2008; Guzman *et al.*, 2011). Although fault tolerant control can be realised, the reduced order decoupling transformation changes the machine parameters and significant modifications to the control structure become necessary.

In (Locment *et al.*, 2008; Apsley, 2010; Tani *et al.*, 2012), it was shown that the normal (full-order) decoupling transformation could be applied to the faulted machine for fault tolerant control. Using the normal transformation, the machine parameters remain unchanged by the fault, and the torque and flux of the machine will still be controlled by the α - β (or d - q) current components. The reduction in the machine's number of degrees of freedom due to a fault is reflected by having non-controllable x - y currents. Nevertheless, the discussions presented in the literature focus only on the α - β machine equations. Here, the effect of the fault on the full set of machine equations (α - β , x - y and zero-sequence) is investigated, to give a complete view on the operation of the machine during the single open-circuit fault.

5.2.1. Machine Equations for Healthy Operation

For convenience, the machine equations and notations explained in earlier chapters are partly repeated here. Using the VSD model, the machine phase variables $[\lambda_k]$ are related to the stationary frame variables $[\lambda_{\alpha\beta\gamma}]$ via decoupling transformation

$[T]$:

$$[\lambda_{\alpha\beta\gamma}] = [T] \cdot [\lambda_k] \quad (5.1)$$

where

$$\begin{aligned} [\lambda_k] &= [\lambda_{a1} \quad \lambda_{b1} \quad \lambda_{c1} \quad \lambda_{a2} \quad \lambda_{b2} \quad \lambda_{c2}]^T \\ [\lambda_{\alpha\beta\gamma}] &= [\lambda_{\alpha} \quad \lambda_{\beta} \quad \lambda_x \quad \lambda_y \quad \lambda_{0+} \quad \lambda_{0-}]^T \end{aligned} \quad (5.2)$$

$$[T] = \frac{1}{\sqrt{3}} \begin{bmatrix} 1 & -\frac{1}{2} & -\frac{1}{2} & \frac{\sqrt{3}}{2} & -\frac{\sqrt{3}}{2} & 0 \\ 0 & \frac{\sqrt{3}}{2} & -\frac{\sqrt{3}}{2} & \frac{1}{2} & \frac{1}{2} & -1 \\ 1 & -\frac{1}{2} & -\frac{1}{2} & -\frac{\sqrt{3}}{2} & \frac{\sqrt{3}}{2} & 0 \\ 0 & -\frac{\sqrt{3}}{2} & \frac{\sqrt{3}}{2} & \frac{1}{2} & \frac{1}{2} & -1 \\ 1 & 1 & 1 & 0 & 0 & 0 \\ 0 & 0 & 0 & 1 & 1 & 1 \end{bmatrix} \quad (5.3)$$

with λ representing arbitrary machine variables (voltage v , current i or flux ψ).

For an induction machine with distributed windings and negligible mutual leakage inductance between the stator windings, the stator equations in terms of the stationary reference frame variables are:

$$\begin{aligned}
v_{\alpha s} &= (R_s + L_s \cdot \frac{d}{dt})i_{\alpha s} + L_{ms} \cdot \frac{d}{dt}i_{\alpha r} \\
v_{\beta s} &= (R_s + L_s \cdot \frac{d}{dt})i_{\beta s} + L_{ms} \cdot \frac{d}{dt}i_{\beta r} \\
v_{xs} &= (R_s + L_{ls} \frac{d}{dt})i_{xs} \\
v_{ys} &= (R_s + L_{ls} \frac{d}{dt})i_{ys} \\
v_{0+s} &= (R_s + L_{ls} \frac{d}{dt})i_{0+s} \\
v_{0-s} &= (R_s + L_{ls} \frac{d}{dt})i_{0-s}
\end{aligned} \tag{5.4}$$

while the rotor equations are

$$\begin{aligned}
0 &= (R_r + L_r \cdot \frac{d}{dt})i_{\alpha r} + \omega_r L_r i_{\beta r} + L_{ms} \cdot \frac{d}{dt}i_{\alpha s} + \omega_r L_{ms} i_{\beta s} \\
0 &= (R_r + L_r \cdot \frac{d}{dt})i_{\beta r} - \omega_r L_r i_{\alpha r} + L_{ms} \cdot \frac{d}{dt}i_{\beta s} - \omega_r L_{ms} i_{\alpha s}
\end{aligned} \tag{5.5}$$

where $L_s = L_{ls} + L_{ms}$, $L_r = L_{lr} + L_{ms}$ and ω_r is the rotor electrical speed. Subscripts s and r are used to represent the stator and rotor variables respectively. The reference frames for both the stator and rotor variables are assumed here to be fixed to the stator for convenience.

For a machine with distributed windings, only the α - β components contribute to flux and torque production, while the remaining components do not provide useful electromechanical energy conversion. Rotational transformation $[D]$ is used to transform α - β components into the synchronous reference frame d - q components (θ_s is the rotational transformation angle).

$$[\lambda_d \quad \lambda_q]^T = [D][\lambda_\alpha \quad \lambda_\beta]^T \tag{5.6}$$

with

$$[D] = \begin{bmatrix} \cos \theta_s & \sin \theta_s \\ -\sin \theta_s & \cos \theta_s \end{bmatrix} \tag{5.7}$$

By obtaining the rotor flux angle according to (4.9) and (4.10), indirect rotor flux oriented control (IRFOC) is achieved. For a more compact representation, the α - β and x - y components can be written in the space vector form, same as (3.8) in Chapter 3:

$$\begin{aligned}\bar{\Lambda}_{\alpha\beta} &= \lambda_\alpha + j\lambda_\beta \\ \bar{\Lambda}_{xy} &= \lambda_x + j\lambda_y\end{aligned}\quad (5.8)$$

Consequently, the rotational transformation can be expressed in a complex exponential form

$$[D] = e^{-j\theta_s} \quad (5.9)$$

An overview of the control structure for IRFOC of a six-phase induction machine is shown in Fig. 5.1. For a healthy six-phase machine, the references for i_{xs} , i_{ys} , i_{0+s} and i_{0-s} are usually set to zero to minimise stator copper losses.

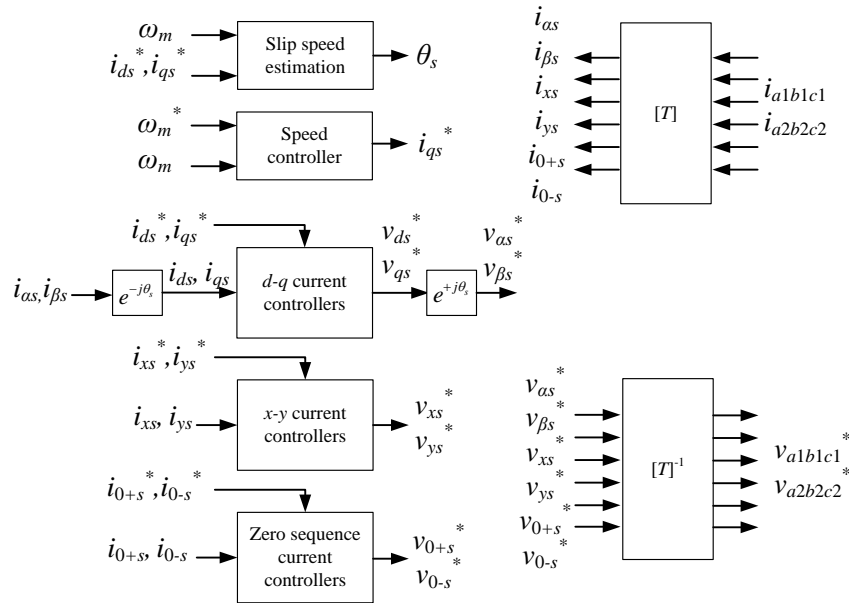


Fig. 5.1. Control structure for IRFOC of a six-phase induction machine.

Regardless of the neutral point connection (single or two isolated neutrals), the same controller structure can be used, with an exception that for the two isolated neutrals case, the zero-sequence current controllers can be disabled by setting $v_{0+s}^* = v_{0-s}^* = 0$, since i_{0+s} and i_{0-s} cannot flow.

5.2.2. Machine Equations for Post-Fault Operation

The fault considered here is an open-circuit fault that disconnects one of the VSC's leg from the machine. It is assumed that the machine winding remains healthy during the fault.

When the open-circuit fault occurs, the corresponding phase current becomes zero, and the machine loses one degree of freedom. As mentioned earlier, to minimise changes to the control, it is better to retain the same decoupling transformation ($[T]$ in this case), so that the same controller structure can be used.

5.2.2.1. Effect of Fault on Machine Equations

If the transformation of the machine equations from the phase variables to the stationary variables is analysed, it is obvious that (5.4)-(5.5) need not be changed because the machine is undamaged by the fault. The main effect of the open-circuit fault is on the currents, where α , β , x , y , $0+$ and $0-$ components are no longer mutually independent due to the loss of one degree of freedom. Hence, it is necessary to find out the currents' relationship during the fault and the subsequent effects on the machine equations.

For the purpose of discussion, it is assumed that the open-circuit fault occurs in phase- $c2$, such that i_{c2} is zero. The α , x and $0+$ currents, which do not contain phase- $c2$ term, remain unaffected by this fault. However, the equations for β , y and $0-$ currents are affected and become:

$$\begin{aligned} i_{\beta s} &= \frac{1}{\sqrt{3}} \left(\frac{\sqrt{3}}{2} i_{b1s} - \frac{\sqrt{3}}{2} i_{c1s} + \frac{1}{2} i_{a2s} + \frac{1}{2} i_{b2s} \right) \\ i_{ys} &= \frac{1}{\sqrt{3}} \left(-\frac{\sqrt{3}}{2} i_{b1s} + \frac{\sqrt{3}}{2} i_{c1s} + \frac{1}{2} i_{a2s} + \frac{1}{2} i_{b2s} \right) \\ i_{0-s} &= \frac{1}{\sqrt{3}} (i_{a2s} + i_{b2s}) \end{aligned} \quad (5.10)$$

These are general expressions that are valid regardless of how the neutral points are configured.

Two Isolated Neutrals

For two isolated neutrals, the phase currents in each three-phase winding must sum to zero ($i_{0+s} = i_{0-s} = 0$). Hence when $i_{c2s} = 0$, $i_{a2s} = -i_{b2s}$, (5.10) is simplified to

$$\begin{aligned} i_{ys} &= -i_{\beta s} \\ i_{0-s} &= 0 \end{aligned} \quad (5.11)$$

Since $i_{0+s} = i_{0-s} = 0$ and $i_{\beta s}$ is not independent from i_{ys} , the machine practically has only three degrees of freedom (α , β and x) during the single open-circuit fault.

Note that there are no changes in the equations for the α - β and x components (5.4). Also, the zero-sequence voltage equations in (5.4) can be discarded because $i_{0+s} = i_{0-s} = 0$. However, as i_{ys} and $i_{\beta s}$ are not mutually independent any more, the stator y -equation is now:

$$v_{ys} = (R_s + L_{ls} \frac{d}{dt}) \cdot i_{ys} = -(R_s + L_{ls} \frac{d}{dt}) \cdot i_{\beta s} \quad (5.12)$$

Single Isolated Neutral

If the machine is configured with a single neutral point, the following relation can be derived:

$$\begin{aligned} i_{0-s} &= \frac{1}{\sqrt{3}}(i_{a2s} + i_{b2s}) = i_{\beta s} + i_{ys} \\ i_{0+s} &= -i_{0-s} \end{aligned} \quad (5.13)$$

The main difference compared with the two-neutral points case is that i_{ys} is now an independent variable, giving the system four degrees of freedom (α , β , x and y).

The machine equations for the α - β and x - y components remain the same as in (5.4) and (5.5). Due to the single neutral connection, neutral point currents can now flow. They are, however, dependent on $i_{\beta s}$ and i_{ys} due to the fault, as shown in (5.13). As a result, the corresponding stator voltage equations are now:

$$\begin{aligned} v_{0+s} &= (R_s + L_{ls} \frac{d}{dt})i_{0+s} = (R_s + L_{ls} \frac{d}{dt})(i_{\beta s} + i_{ys}) \\ v_{0-s} &= (R_s + L_{ls} \frac{d}{dt})i_{0-s} = -(R_s + L_{ls} \frac{d}{dt})(i_{\beta s} + i_{ys}) \end{aligned} \quad (5.14)$$

5.2.2.2. Effect on Torque Equation

The post-fault torque equation can be obtained by considering the following phase variable equation:

$$T_e = p [i_{ks}]^T \cdot \frac{d}{d\theta_r} [L_{sr}] \cdot [i_{kr}] \quad (5.15)$$

where p is the number of pole pairs, θ_r is the rotor angle and $[L_{sr}]$ is the stator-to-rotor mutual inductance matrix.

Since the machine is not damaged, $[L_{sr}]$ is considered to be unaffected by the fault. This also implies that even though i_{c2s} cannot flow, voltage can still be induced in phase- $c2$ (as a form of back EMF) due to the variation in rotor currents.

By applying decoupling transformation to the equation, the torque equation during the fault is identical as for the healthy machine.

$$T_e = pL_{ms}(i_{\beta r} \cdot i_{cs} - i_{cr} \cdot i_{\beta s}) \quad (5.16)$$

This is actually the similar conclusion drawn by (Locment *et al.*, 2008; Apsley, 2010; Tani *et al.*, 2012).

5.2.2.3. Conclusions on Post-fault Machine Equations

Three important conclusions can be drawn from the post-fault machine equations based on the transformed model:

- 1) The α - β equations, which are responsible for flux and torque production, remain unchanged even after the fault. Hence, no modifications on the machine parameters are required in the implementation of FOC, unlike in (Zhao and Lipo, 1996a; Zhao and Lipo, 1996b; Ryu *et al.*, 2006; Kianinezhad *et al.*, 2008), where reduced order transformations are used.
- 2) The y - or zero-sequence components are no longer independent during the fault, as dictated by (5.12) and (5.14). For a healthy machine, these current components are independent and usually controlled to zero for loss minimisation. However, during the open-circuit fault, they are coupled to the α - β components. Attempt to control them to zero will cause disruption to the α - β current regulation, which manifests as torque and speed oscillations. Hence, the current references need to be adapted during the fault.

3) The torque equation remains unaffected during the fault, as indicated in (5.16).

Thus, for smooth torque during the fault, the α - β stator current references should take the following form:

$$\begin{aligned} i_{\alpha s}^* &= I_{\alpha\beta s} \cos(\theta_s + \delta) \\ i_{\beta s}^* &= I_{\alpha\beta s} \sin(\theta_s + \delta) \end{aligned} \quad (5.17)$$

with δ being the angle between stator current and rotor flux space vectors.

Based on (5.17), the space vector of the post-fault α - β stator current reference is

$$\vec{I}_{\alpha\beta s}^* = I_{\alpha\beta s} e^{+j(\theta_s + \delta)} \quad (5.18)$$

This means that $\vec{I}_{\alpha\beta s}^*$ contains only positive sequence component and forms a circular trajectories in the α - β reference frame, just like in the case of a healthy machine.

5.3. Derivation of Post-fault Current References

5.3.1. Derating Factor

If the faulted machine is to generate rated flux and torque, the phase currents will increase above their rated values. Prolonged operation with such over rated phase currents is hazardous as it may violate the thermal limit of both the machine and the power electronic converter. Hence, for continuous post-fault operation, the machine should be “derated”, i.e. run below the rated values. This is not a problem for applications like traction and offshore wind generation, where operation at rated power is not compulsory and the capability to continue under fault conditions is highly valued.

To illustrate the amount of derating required, a variable termed “derating factor”, a , is considered in the following discussion. The derating factor is the factor by which the flux and torque currents ($I_{\alpha\beta s}$) need to be scaled down for derated operation. This

variable is defined as the ratio of the post-fault α - β (or d - q) currents' magnitude to the pre-fault current magnitude (rated stator phase current rms is denoted with I_{sn}):

$$a = \frac{I_{\alpha\beta,post-fault}}{I_{\alpha\beta,n}} = \frac{I_{dq,post-fault}}{I_{\alpha\beta,n}} = \frac{I_{dq,post-fault}}{\sqrt{6}I_{sn}} \quad (5.19)$$

A derating factor of 1 implies that the machine is not derated and is producing rated flux and torque. For any value $a < 1$, the machine operates with lower-than-rated flux and torque producing current, and is considered to be derated. While the α - β current magnitude is important in determining the flux and torque of the machine, it is however the phase current amplitude that needs to be limited. Thus, a ‘‘threshold derating factor’’, a_o , is defined here as the derating factor required to keep the maximum post-fault phase current equal to the rated value. The relation between the maximum peak post-fault phase current and the rated phase current is hence given by

$$a_o = a \frac{\sqrt{2}I_{sn}}{\max(i_{phase,post-fault})} = \frac{I_{dq,post-fault}}{\sqrt{3} \max(i_{phase,post-fault})} \quad (5.20)$$

Since the post-fault machine equations have identical form as in the pre-fault case, the torque equation can be expressed in terms of the d - q currents, assuming RFOC, as:

$$T_e = p \frac{L_{ms}^2}{L_r} i_{ds} i_{qs} \quad (5.21)$$

When the fault happens, it may be necessary to derate the machine by reducing the i_{ds} and i_{qs} , to keep the maximum phase current within the acceptable limits. If both i_{ds} and i_{qs} are scaled down by factors a_d and a_q respectively, the achievable torque in terms of rated torque is given by:

$$T_{e_post_fault} = a_d a_q T_{en} \quad (5.22)$$

The achievable torque in derated operation depends on how i_{ds} and i_{qs} are scaled down. Here, it is suggested to keep i_{ds} at rated value, and only derate i_{qs} (i.e., $a_d = 1$ and

$a_q < 1$) to keep the phase current amplitude at rated:

$$T_{e_post_fault} = a_q T_{en} \quad (5.23)$$

The influence of a_q on the overall reduction of the d - q current magnitude (which is also the derating factor, a) is given with

$$a = \sqrt{\frac{i_{dsn}^2 + a_q^2 \cdot i_{qsn}^2}{i_{dsn}^2 + i_{qsn}^2}} \quad (5.24)$$

The expressions (5.23) and (5.24) indicate that the achievable torque during post-fault operation depends on the ratio i_{dsn}/i_{qsn} . For a special case of $i_{dsn}/i_{qsn} = 0$, applicable to a permanent magnet machine, the post-fault torque varies linearly with a . For an induction machine, the variation in torque is non-linear when the machine is derated, with a higher i_{dsn}/i_{qsn} ratio giving a more rapid reduction in achievable torque. This will be confirmed later by the experimental results.

5.3.2. Modes of Operation

While the α - β (d - q) stator currents determine the flux and torque of the machine, the other current components provide additional degrees of freedom which define the mode of post-fault operation. For this purpose, the x - y currents are defined in the following general form:

$$i_{xs}^* = K_1 i_{\alpha s}^* + K_2 i_{\beta s}^* \quad (5.25a)$$

$$i_{ys}^* = K_3 i_{\alpha s}^* + K_4 i_{\beta s}^* \quad (5.25b)$$

The values of K_1 , K_2 , K_3 and K_4 can be chosen based on the desired modes of operation.

In this chapter, two different modes of operation are considered, i.e.:

1) Minimum Losses (Min Loss)

Coefficients are selected to minimize the stator winding loss, which is defined as

$$\begin{aligned} P_{loss} &= R_s (i_{a1s}^2 + i_{b1s}^2 + i_{c1s}^2 + i_{a2s}^2 + i_{b2s}^2 + i_{c2s}^2) \\ &= R_s (i_{\alpha s}^2 + i_{\beta s}^2 + i_{xs}^2 + i_{ys}^2 + i_{0+s}^2 + i_{0-s}^2) \end{aligned} \quad (5.26)$$

This is equivalent to minimizing $(i_{xs}^2 + i_{ys}^2 + i_{0+s}^2 + i_{0-s}^2)$, i.e. the sum of the squared current components that do not contribute to flux and torque production.

This is one of the most commonly reported post-fault operation, such as in (Zhao and Lipo, 1996a; Zhao and Lipo, 1996b; Apsley, 2010; Tani *et al.*, 2012).

2) Maximum Torque (Max Torque)

Coefficients are selected to produce the largest $I_{\alpha\beta}$ (hence the maximum torque) with the maximum phase current amplitude maintained at the rated value. This is equivalent to finding the coefficients that give the highest value of a_o .

For applications such as offshore wind generator, this allows the generator to maximise its generated power after fault. This mode of operation is relatively less discussed in the literature. However, as can be observed later, this mode of operation actually gives equivalent results as the equalised phase current method (Fu and Lipo, 1994; Kianinezhad *et al.*, 2008; Apsley, 2010).

The phase currents are related to the VSD variables via the inverse decoupling transformation $[T]^{-1}$:

$$[i_{ks}] = [T]^{-1} \cdot [i_{\alpha\beta\gamma s}] \quad (5.27)$$

The relationship between stator phase and α - β currents can be obtained by substituting (5.11) and (5.25) or (5.13) and (5.25), for two and single isolated neutral points, respectively, into (5.27) and rearranging the expression. Hence for *two isolated neutrals*:

$$\begin{bmatrix} i_{a1s}^* \\ i_{b1s}^* \\ i_{c1s}^* \\ i_{a2s}^* \\ i_{b2s}^* \end{bmatrix} = \frac{1}{\sqrt{3}} \begin{bmatrix} 1+K_1 & 0 \\ -\frac{1}{2}(1+K_1) & \sqrt{3}-\frac{1}{2}K_2 \\ -\frac{1}{2}(1+K_1) & -\sqrt{3}-\frac{1}{2}K_2 \\ \frac{\sqrt{3}}{2}(1-K_1) & -\frac{\sqrt{3}}{2}K_2 \\ -\frac{\sqrt{3}}{2}(1-K_1) & \frac{\sqrt{3}}{2}K_2 \end{bmatrix} \cdot \begin{bmatrix} i_{\alpha s}^* \\ i_{\beta s}^* \end{bmatrix} \quad (5.28)$$

while for a *single isolated neutral*:

$$\begin{bmatrix} i_{a1s}^* \\ i_{b1s}^* \\ i_{c1s}^* \\ i_{a2s}^* \\ i_{b2s}^* \end{bmatrix} = \frac{1}{\sqrt{3}} \begin{bmatrix} 1+K_1-K_3 & -1+K_2-K_4 \\ -\frac{1}{2}-\frac{K_1}{2}+\left(\frac{\sqrt{3}}{2}+1\right)K_3 & \frac{\sqrt{3}}{2}-1-\frac{K_2}{2}-\left(\frac{\sqrt{3}}{2}+1\right)K_4 \\ -\frac{1}{2}-\frac{K_1}{2}+\left(\frac{\sqrt{3}}{2}-1\right)K_3 & -\frac{\sqrt{3}}{2}-1-\frac{K_2}{2}+\left(\frac{\sqrt{3}}{2}-1\right)K_4 \\ \frac{\sqrt{3}}{2}-\frac{\sqrt{3}K_1}{2}+\frac{3K_3}{2} & \frac{3}{2}-\frac{\sqrt{3}K_2}{2}+\frac{3K_4}{2} \\ -\frac{\sqrt{3}}{2}+\frac{\sqrt{3}K_1}{2}+\frac{3K_3}{2} & \frac{3}{2}+\frac{\sqrt{3}K_2}{2}+\frac{3K_4}{2} \end{bmatrix} \begin{bmatrix} i_{\alpha s}^* \\ i_{\beta s}^* \end{bmatrix} \quad (5.29)$$

The relationship between the coefficients and the threshold derating factor can be obtained by iteratively varying the coefficients, based on (5.28) and (5.29). Fig. 5.2 shows the plot of a_o against K_1 and K_2 , for the machine with two isolated neutrals. The coefficients and threshold derating factors that define different modes of post-fault operation with different neutral point configurations are summarized in Table 5.1. Using the coefficients listed in Table 5.1, the theoretical mean stator winding losses for different modes of post-fault operation can be calculated based on (5.26). The losses, normalised with respect to the stator winding loss of the healthy machine, are given in Table 5.2.

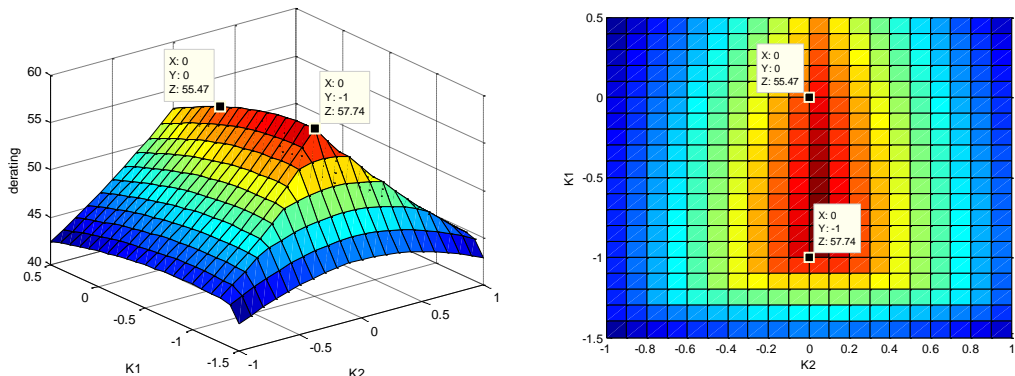


Fig. 5.2. Threshold derating factor (in %) as a function of K_1 and K_2 , for asymmetrical six-phase induction machine with two isolated neutrals.

Table 5.1. Summary of coefficients for different modes of post-fault operation (open-circuit fault in phase-c2)*.

Neutrals	Mode	K_1	K_2	K_3	K_4	a_o
Two, isolated	Max Torque	-1	0	0	-1	0.577
	Min Loss	0	0	0	-1	0.555
Single, isolated	Max Torque	-0.295	-0.754	-0.209	-0.641	0.694
	Min Loss	0	0	0	-0.5	0.536

*Coefficients K_3 and K_4 are fixed (see (8)), for the machine with two isolated neutrals and this is indicated by using shaded cells.

Table 5.2. Normalised mean stator winding losses for different modes of post-fault operation.

Neutrals	Mode	Mean Stator Losses (p.u.)
-	Single VSC	2.00
Two, isolated	Max Torque	2.00
	Min Loss	1.50
Single, isolated	Max Torque	1.73
	Min Loss	1.37

For a six-phase machine, it has been suggested that a simple fault tolerant operation can be achieved by taking advantage of the windings' modularity. In an event of fault, the whole three-phase winding containing the fault can be excluded, such that the six-phase machine is operating as a three-phase machine, controlled with essentially single three-phase VSC (Shamsi-Nejad *et al.*, 2008). This mode is referred to as "single VSC" mode here and will be compared against other modes of post-fault operation in later part of the chapter.

All the discussions and derivations so far were based on the open-circuit fault in phase-*c2*. Using the same principles, machine equations can be obtained for fault in phase-*a1*. Instead of having coupling between β , y and 0^- components, the coupling now exists between α , x and 0^+ components. Corresponding coefficients for post-fault operation can be obtained from Table 5.1, by swapping β with α , y with x and 0^- with 0^+ components. The results are shown in Table 5.3. Note that the result obtained for Max Torque mode of single isolated neutral case is identical to the one given in (Fu and Lipo, 1994).

Table 5.3. Summary of coefficients for different modes of post-fault operation (open-circuit fault in phase-*a1*)^{*}.

Neutrals	Mode	K_1	K_2	K_3	K_4	a_o
Two, isolated	Max Torque	-1	0	0	-1	0.577
	Min Loss	-1	0	0	0	0.555
Single, isolated	Max Torque	-0.641	-0.209	-0.754	-0.295	0.694
	Min Loss	-0.5	0	0	0	0.536

^{*} Coefficients K_1 and K_2 are fixed for the machine with two isolated neutrals and this is indicated by using shaded cells.

Due to the symmetry of the phases within each three-phase winding, the results in Table 5.1 and 5.3 can be made readily applicable to other phases by reordering the phase sequence. For fault that occurs in phase-*a1*, *b1* or *c1*, post-fault strategy for

phase- $a1$ can be adopted; for fault in phase- $a2$, $b2$ or $c2$, the strategy developed for phase- $c2$ can be used with corresponding phase rearrangement.

5.4. Current Control Methods

Following the derivation of post-fault current references, it is necessary to select the suitable current control method to implement these current references. This section hence studies the suitable current control methods based on linear (PI) controllers.

5.4.1. Leg-to-Phase Voltage Transformation

5.4.1.1. Healthy Case

During healthy operation, the phase voltages of a six-phase machine with star connected stator windings can be related to the converter's leg voltages via a constant transformation matrix:

$$[v_s] = [A] \cdot [v_o] \quad (5.30)$$

where

$$\begin{aligned} [v_s] &= [v_{a1s} \quad v_{b1s} \quad v_{c1s} \quad v_{a2s} \quad v_{b2s} \quad v_{c2s}]^T \\ [v_o] &= [v_{a1o} \quad v_{b1o} \quad v_{c1o} \quad v_{a2o} \quad v_{b2o} \quad v_{c2o}]^T \end{aligned} \quad (5.31)$$

where v_s is the phase voltage of the stator winding, while v_o is the leg voltage, which is the voltage at the output of one converter leg with respect to an arbitrary reference point O . For simplicity, the point O is assumed to be the dc-link midpoint, so that the dc-component in the leg voltage and the neutral point voltages (v_{n1o} and v_{n2o}) will be zero.

The transformation matrix $[A]$ depends on the stator windings' connection. For machine with star connected stator windings, the leg voltage v_o is the sum of phase voltage v_s and the neutral point voltage v_{no} . The neutral point voltage is the sum of leg voltages divided by the number of connected legs. From these relations, the matrix $[A]$

can be obtained. For a six-phase machine with two and with single isolated neutral, the transformation matrices are:

Two isolated neutrals:

$$[A] = \frac{1}{3} \begin{bmatrix} 2 & -1 & -1 & 0 & 0 & 0 \\ -1 & 2 & -1 & 0 & 0 & 0 \\ -1 & -1 & 2 & 0 & 0 & 0 \\ 0 & 0 & 0 & 2 & -1 & -1 \\ 0 & 0 & 0 & -1 & 2 & -1 \\ 0 & 0 & 0 & -1 & -1 & 2 \end{bmatrix} \quad (5.32)$$

Single isolated neutral:

$$[A] = \frac{1}{6} \begin{bmatrix} 5 & -1 & -1 & -1 & -1 & -1 \\ -1 & 5 & -1 & -1 & -1 & -1 \\ -1 & -1 & 5 & -1 & -1 & -1 \\ -1 & -1 & -1 & 5 & -1 & -1 \\ -1 & -1 & -1 & -1 & 5 & -1 \\ -1 & -1 & -1 & -1 & -1 & 5 \end{bmatrix} \quad (5.33)$$

When current control is implemented using voltage source converter (VSC), the outputs of the current controllers are the phase voltage references, as shown in Fig. 5.1.

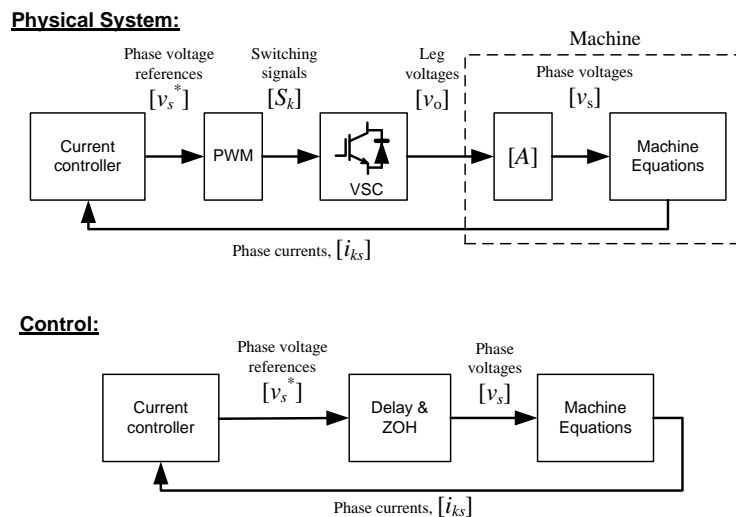


Fig. 5.3. Relation between controller's outputs and the actual phase voltages from physical system's and control's perspective.

Since the machine is fed with an n -leg VSC, the phase voltages are actually controlled indirectly by the manipulation of converter's leg voltages. This is realised through three stages: pulse-width modulator, voltage source converter and the

transformation matrix $[A]$ (due to the physical connection of the machine windings). From the control's perspective, the three stages can be simplified and represented by a delay and zero-order hold (ZOH) as shown in Fig. 5.3, to represent the delay due to computation and PWM. Neglecting the delay and ZOH block, it can be observed that the actual phase voltages change linearly with the controller's outputs (phase voltage references). This linear relation between the actual and commanded phase voltage forms the basis on which current control can be realised using linear (PI) controllers.

5.4.1.2. Disturbance Voltage during Post-fault Operation

However, during the fault, since the faulted stator winding is left floating, the constant relationship between phase and leg voltages (defined by $[A]$) is no longer valid. The faulted phase is no longer controllable by the VSC, and the phase voltage is equal to its stator back EMF ($v_{c2s} = E_{c2s}$). This part of the chapter hence derives the relation between the actual and reference phase voltages of the machine during fault.

Several assumptions are used to simplify the discussion. Firstly, zero-sequence injection is not used since its validity remains questionable for a faulted machine. Second, ideal operation of the VSC is assumed. Lastly, the derivations are based on the low frequency components of the voltage/currents, with the higher frequency components due to the switching of VSC ignored.

The actual phase voltages during post-fault operation can still be expressed as the sum of phase voltage references and the respective neutral point voltages (v_{n1o} and v_{n2o}).

$$[v_s] = \begin{bmatrix} v_{a1o} - v_{n1o} \\ v_{b1o} - v_{n1o} \\ v_{c1o} - v_{n1o} \\ v_{a2o} - v_{n2o} \\ v_{b2o} - v_{n2o} \\ E_{c2s} \end{bmatrix} = \begin{bmatrix} v_{a1s}^* - v_{n1o} \\ v_{b1s}^* - v_{n1o} \\ v_{c1s}^* - v_{n1o} \\ v_{a2s}^* - v_{n2o} \\ v_{b2s}^* - v_{n2o} \\ E_{c2s} \end{bmatrix} \quad (5.34)$$

The neutral point voltages are $v_{n1o} = v_{n2o} = v_{no}$ for single neutral point, and $v_{n1o} = 0$ for two neutral points.

The determination of neutral point voltages is explained next. Consider first the case with two isolated neutrals and an open-circuit fault in phase- $c2$. Fig. 5.4 shows the schematics of the three-phase winding 2 for the faulted machine. Winding 1 is isolated from winding 2 and hence not illustrated here. Each phase winding can be sufficiently represented by a Thevenin equivalent circuit, consisting of back EMF source and an equivalent RL branch.

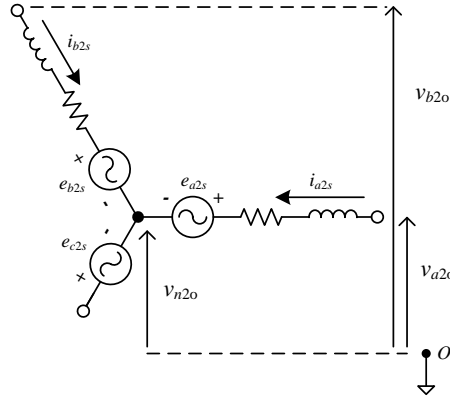


Fig. 5.4. Schematic representation of winding 2 (phase- $a2b2c2$) with single open-circuit fault in phase- $c2$ winding.

The leg voltages for phase- $a2$ and $b2$ are given by

$$\begin{aligned} v_{a2o} &= v_{n2o} + \left(R + L \frac{d}{dt}\right) \cdot i_{a2o} + E_{a2s} \\ v_{b2o} &= v_{n2o} + \left(R + L \frac{d}{dt}\right) \cdot i_{b2o} + E_{b2s} \end{aligned} \quad (5.35)$$

Since $i_{b2o} + i_{a2o} = 0$ and $E_{a2s} + E_{b2s} + E_{c2s} = 0$ (detailed derivations are given in Appendix C), the sum of the two equations in (5.35) gives

$$v_{a2o} + v_{b2o} = 2v_{n2o} - E_{c2s} \quad (5.36)$$

Neglecting converter nonlinearity and high frequency voltage components, the leg voltages (v_{ko}) are equivalent to the commanded phase voltage references (v_{ks}^*).

With that in mind and with $v_{0+s}^* = v_{0-s}^* = 0$, the phase voltage references are :

$$v_{a2s}^* + v_{b2s}^* = -v_{c2s}^* \quad (5.37)$$

By substituting (5.37) into (5.36) and rearranging, the neutral point voltage of winding 2 can be obtained as

$$v_{n2o} = \frac{1}{2}(-v_{c2s}^* + E_{c2s}) \quad (5.38)$$

Using the similar concept as described above, but taking into account all the six phases, the neutral point voltage for single neutral point case can be obtained as

$$v_{no} = \frac{1}{5}(-v_{c2s}^* + E_{c2s}) \quad (5.39)$$

By substituting (5.38) or (5.39) into (5.34), and then applying the decoupling transformation $[T]$, relation between the actual and commanded phase voltages can be obtained as summarised in Table 5.4. The results show that leg-to-phase voltage transformation during fault introduces disturbance voltage v_{dis} to the α - β plane. When linear controllers are used for α - β current regulation, the presence of such disturbance needs to be considered and compensated.

Table 5.4. Summary of leg-to-phase voltage relations for asymmetrical six-phase machine with two and single Isolated neutral.

Two isolated neutrals	Single isolated neutral
$\begin{bmatrix} v_{\alpha s} \\ v_{\beta s} \\ v_{xs} \\ v_{ys} \\ v_{0+s} \\ v_{0-s} \end{bmatrix} = \begin{bmatrix} v_{\alpha s}^* \\ v_{\beta s}^* \\ v_{xs}^* \\ v_{ys}^* \\ v_{0+s}^* \\ v_{0-s}^* \end{bmatrix} + \begin{bmatrix} 0 \\ v_{dis} \\ 0 \\ -v_{dis} \\ 0 \\ 0 \end{bmatrix}$	$\begin{bmatrix} v_{\alpha s} \\ v_{\beta s} \\ v_{xs} \\ v_{ys} \\ v_{0+s} \\ v_{0-s} \end{bmatrix} = \begin{bmatrix} v_{\alpha s}^* \\ v_{\beta s}^* \\ v_{xs}^* \\ v_{ys}^* \\ v_{0+s}^* \\ v_{0-s}^* \end{bmatrix} + \begin{bmatrix} 0 \\ v_{dis}' \\ 0 \\ -v_{dis}' \\ -\frac{v_{dis}'}{2} \\ \frac{v_{dis}'}{2} \end{bmatrix}$
with	with
$v_{dis} = -\frac{\sqrt{3}}{2}(-v_{c2s}^* + E_{c2s})$	$v_{dis}' = -\frac{2\sqrt{3}}{5}(-v_{c2s}^* + E_{c2s})$

It should be emphasised here that the presence of this disturbance due to the leg-to-phase voltage transformation depends on the type of decoupling transformation used. For instance, the disturbance voltage is not present for the reduced order transformation used in (Ryu *et al.*, 2008). Nevertheless, because of the choice of the transformation,

there appear to be asymmetries related to the resistance term of the transformed machine equations. As a result, feedforward compensation has to be provided in order to obtain good α - β current regulation.

5.4.1.3. Effect on Current Controllers

As shown in the previous subsection, the fault introduces additional disturbance voltage, v_{dis} into the machine equations. For the specific case of two isolated neutrals configuration, with open-circuit fault in phase- $c2$, the disturbance appears in the β - and y -axis equations. The presence of v_{dis} in β -axis equation introduces a negative sequence voltage component ($\vec{V}_{\alpha\beta-}$) in the α - β plane. In order to regulate the currents to their references, the current controller must be able to compensate this negative sequence component. For a single PI controller in synchronous (d - q) reference frame used in conventional current control method, this is beyond the natural capability of the controller so the current regulation will not be good.

Keeping in mind that the discussion here focuses on the use of linear (PI) controller for fault-tolerant control, two current control methods that provide good α - β current regulation are discussed here.

Method 1 (Fig. 5.5)

If v_{dis} can be reduced, the negative sequence component in α - β plane will diminish, and single synchronous PI controller can easily regulate the α - β currents to their references. This can be achieved by regulating the x - y currents to their references using dual PI controllers of Chapter 3.

For the case of open-circuit fault in phase- $c2$, the y -current reference has to be set as $i_{ys}^* = -i_{\beta s}^*$, while x -current reference can be set based on desired mode of post-fault operation, as listed in Table 5.1. This is similar to the current control approach reported in (Tani *et al.*, 2012). Albeit being relatively straight-forward in terms of

implementation, one peculiarity remains: the number of controlled variables (i.e. the stator currents) remained the same before and after the fault, despite the loss of a degree of freedom. This issue was not addressed in (Tani *et al.*, 2012), but can be explained by taking into consideration the presence of v_{dis} .

There is no doubt that an open-circuit fault reduces the number of controllable currents by one. However, the fault also introduces the disturbance voltage v_{dis} as an additional degree of freedom. From the inverse decoupling transformation, v_{c2s}^* can be obtained as:

$$v_{c2s}^* = \frac{1}{\sqrt{3}}(-v_{\beta s}^* - v_{ys}^*) \quad (5.40)$$

Based on (5.40), the disturbance voltage v_{dis} is found to be dependent on β - and y -current controller outputs, i.e.:

$$v_{dis} = -\frac{1}{2}(v_{\beta s}^* + v_{ys}^*) - \frac{\sqrt{3}}{2}E_{c2s} \quad (5.41)$$

The y -current controller (together with β -current controller) then operates by reducing v_{dis} , to a value small enough so that $i_{\beta s}$ can be regulated to its reference, so that eventually $i_{ys} = i_{ys}^* = -i_{\beta s}^*$.

Method 2 (Fig. 5.6)

Since the negative sequence component is the main cause of poor α - β current regulation, an alternative approach is to modify the α - β current controllers to compensate the negative sequence component, $\vec{V}_{\alpha\beta-}$. An additional PI controller, implemented in the anti-synchronous direction, can be used for this purpose. Using this method, α - β and x -current are controlled using dual PI controllers. Since the y -current is not controllable, the y -current controller can be disabled, by setting $v_{ys}^* = 0$.

Due to the different approaches adopted, the two methods produce different VSC leg voltages and machine neutral point voltage. Compared with Method 2, Method 1 will yield significantly smaller fundamental frequency component in the neutral point voltage of the faulted winding because of the controller's contribution in minimising the disturbance voltage. The experimental verifications of these two current control methods are presented in subsequent section.

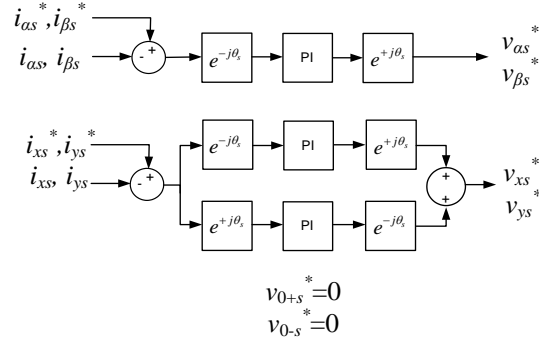


Fig. 5.5. Current controllers for control of a six-phase induction machine with two isolated neutrals, using Method 1.

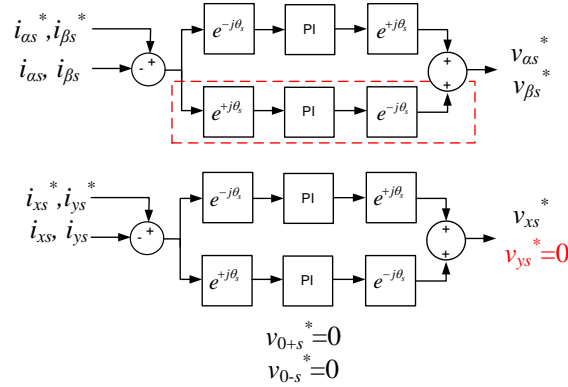


Fig. 5.6. Current controllers for control of a six-phase induction machine with two isolated neutrals, using Method 2.

5.5. Experimental Results and Discussions

This section shows the experimental results for verifying the theoretical discussion presented in the previous parts of this chapter. Tests are conducted again on the same prototype asymmetrical six-phase induction machine used in Chapter 3 and 4. The machine is controlled in speed control mode with IRFOC. A dc machine, controlled using ABB DCS800 drive, is coupled to the six-phase machine and functions as a variable load. Speed measurement is done using a tachogenerator attached to the dc-

machine. Since the test rig does not contain torque sensor, torque measurement is not possible and is hence omitted from discussion.

A six-leg VSC is used to control the six-phase machine. Switching frequency is selected as 2 kHz, and the currents are sampled at twice the switching frequency. Carrier-based pulse-width modulation is used, without any zero-sequence injection. The control is implemented using DS1006 dSpace system with ControlDesk control environment. Experimental data, displayed in this section, are obtained by using the data capture function in ControlDesk and processed using Matlab.

5.5.1. Verification of the Current Control Methods

Based on the discussion presented in Section 5.4, the two current control methods discussed are tested on the asymmetrical six-phase machine configured with two-isolated neutrals. Initially, the machine is operated in healthy condition, at a constant speed of 500 rpm with 50% rated torque. Fig. 5.7 shows the steady state α - β - x - y components of the stator voltage references and currents for the healthy machine. As expected, the α - β currents are regulated to follow a circular trajectory, with x - y currents controlled at zero to minimize losses.

To emulate the open-circuit fault, connection of phase- $c2$ is open-circuited. The faulted machine is then regulated at a constant speed of 500 rpm with 50% load, using the post-fault current control methods shown in Figs. 5.5 and 5.6. For convenience, the Min Loss mode of operation is chosen. Figs. 5.8 and 5.9 show the steady state α - β and x - y components of the stator voltage references and currents for a faulted machine, controlled using Method 1 and Method 2, respectively. The steady state neutral point voltage and its FFT spectrum for the two control methods are shown in Fig. 5.10.

It can be observed that the voltage references generated by the two methods are very different. For Method 1, non-zero y -voltage reference (Fig. 5.8 (b)) is produced by the y -current controller to reduce the disturbance voltage. As seen in Fig. 5.10, the

fundamental frequency component in the neutral point voltage for Method 1 is significantly smaller than that of Method 2. As a result, good regulation of α - β currents is possible using synchronous PI controller in α - β plane. Moreover, with the disturbance voltage reduced, the negative sequence component in the α - β plane becomes negligible, such that α - β voltages references in Method 1 still span a circular trajectory (Fig. 5.8(a)).

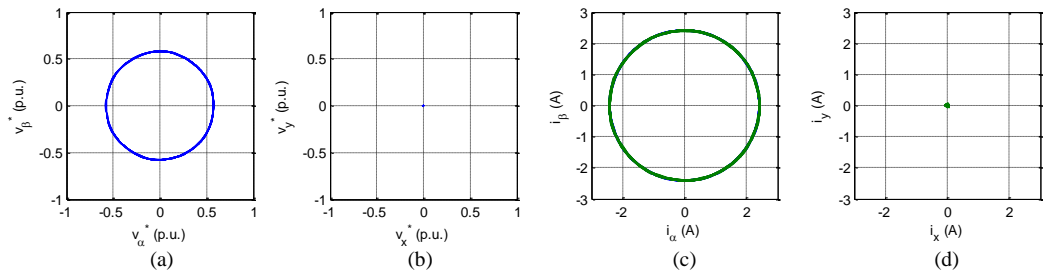


Fig. 5.7. Steady state stator (a) α - β voltage references, (b) x - y voltage references, (c) α - β currents and (d) x - y currents trajectories, for healthy asymmetrical six-phase machine controlled using IRFOC. The machine is operating with 50% rated load at a constant speed of 500 rpm.

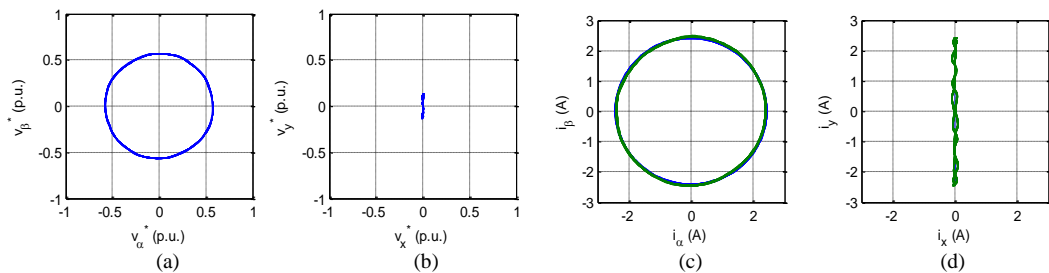


Fig. 5.8. Steady state (a) α - β voltage references, (b) x - y voltage references, (c) α - β currents and (d) x - y currents trajectories, for faulted asymmetrical six-phase machine controlled using Method 1. The machine is operating with 50% rated load at a constant speed of 500 rpm.

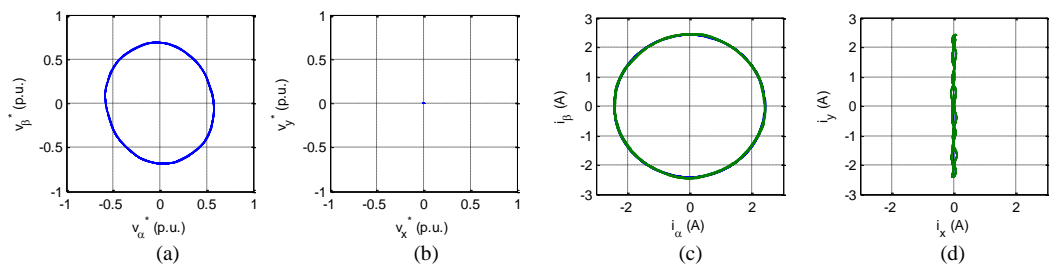


Fig. 5.9. Steady state (a) α - β voltage references, (b) x - y voltage references, (c) α - β currents and (d) x - y currents trajectories, for faulted asymmetrical six-phase machine controlled using Method 2. The machine is operating with 50% rated load at a constant speed of 500 rpm.

For Method 2, the y -voltage reference is zero (Fig. 5.9(b)) since the y -current controller is disabled. As seen in Fig. 5.10(b), the neutral point voltage contains a significant fundamental frequency component, which in turn produces disturbance voltage in the form of a negative sequence voltage in the α - β plane. Nevertheless, good current regulation is still obtained by the use of a dual PI controller, which is able to compensate the negative sequence α - β voltages. As seen in Fig. 5.9(a) the resultant α - β

voltage reference generated by the controller spans an elliptical trajectory, suggesting the presence of a significant negative sequence component.

The dynamics of different control approaches are seen in Figs. 5.11-5.13. Fig. 5.11 shows the speed and d - q currents for the case of a healthy machine without load. When the machine speed changes from -500 rpm to 500 rpm, the torque producing current (i_{qs}) changes accordingly, while the flux producing current (i_{ds}) remains at a constant value. Good decoupling of d - q current control can be observed.

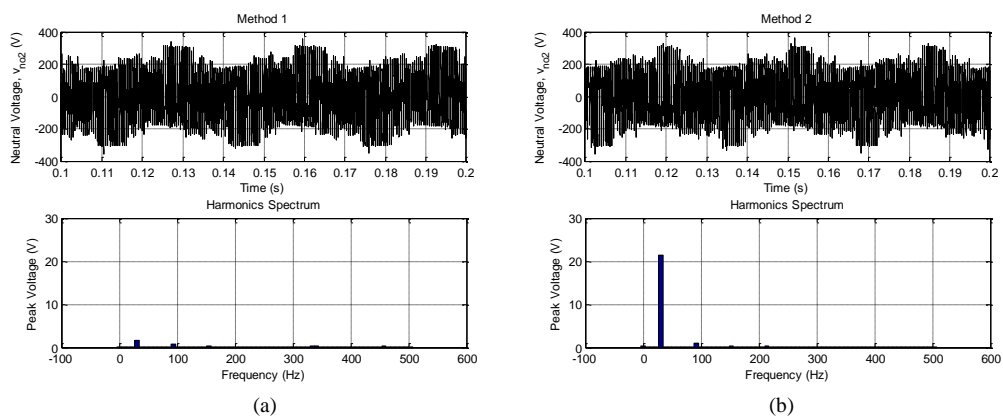


Fig. 5.10. Comparison of steady state neutral point voltage and its FFT spectrum for a faulted asymmetrical six-phase machine controlled using (a) Method 1 and (b) Method 2.

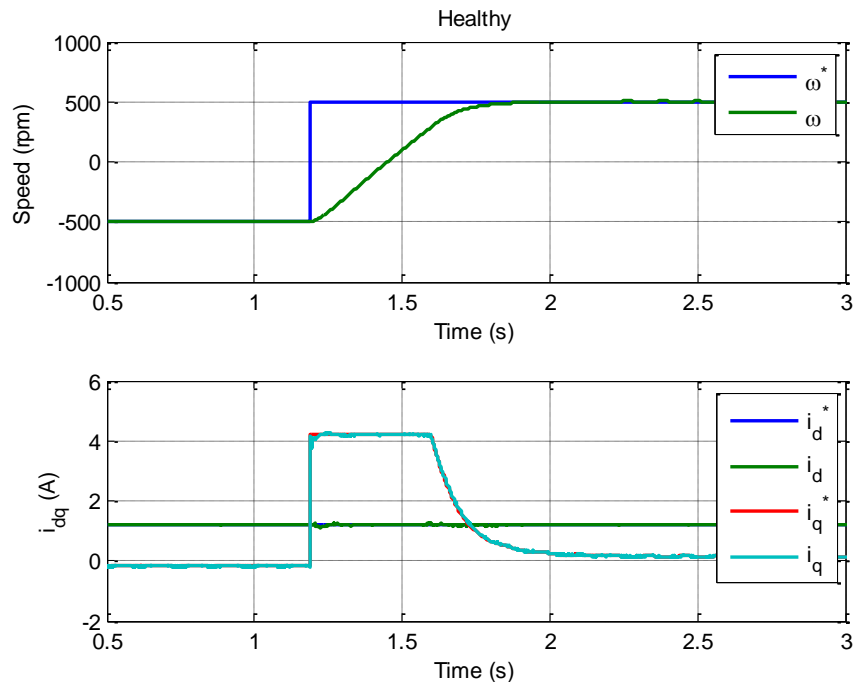


Fig. 5.11. Speed (top) and d - q currents (bottom) variation during no-load speed reversal from -500 rpm to 500 rpm, for healthy six-phase machine controlled using IRFOC.

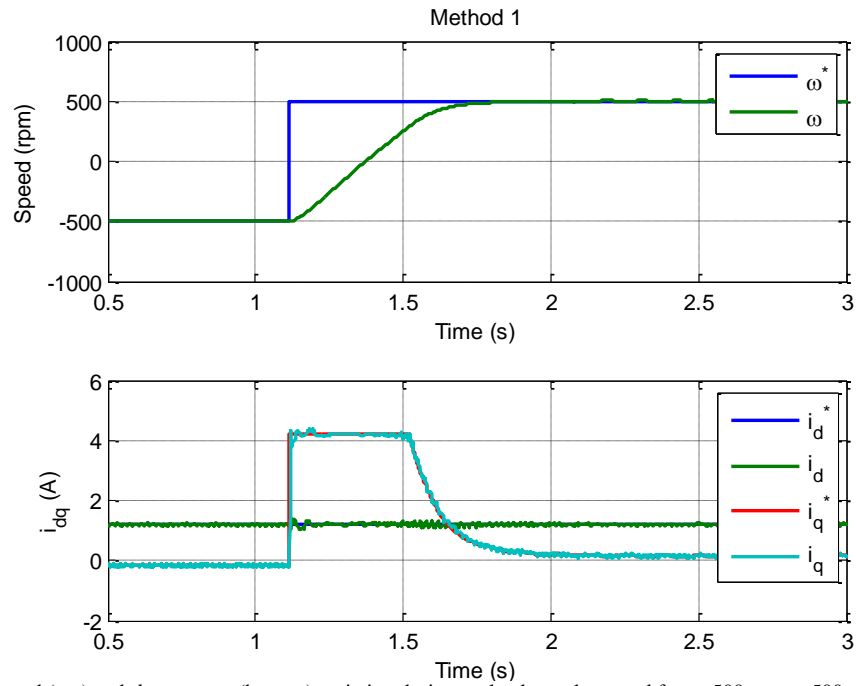


Fig. 5.12. Speed (top) and d - q currents (bottom) variation during no-load speed reversal from -500 rpm to 500 rpm, for faulted six-phase machine controlled using Method 1.

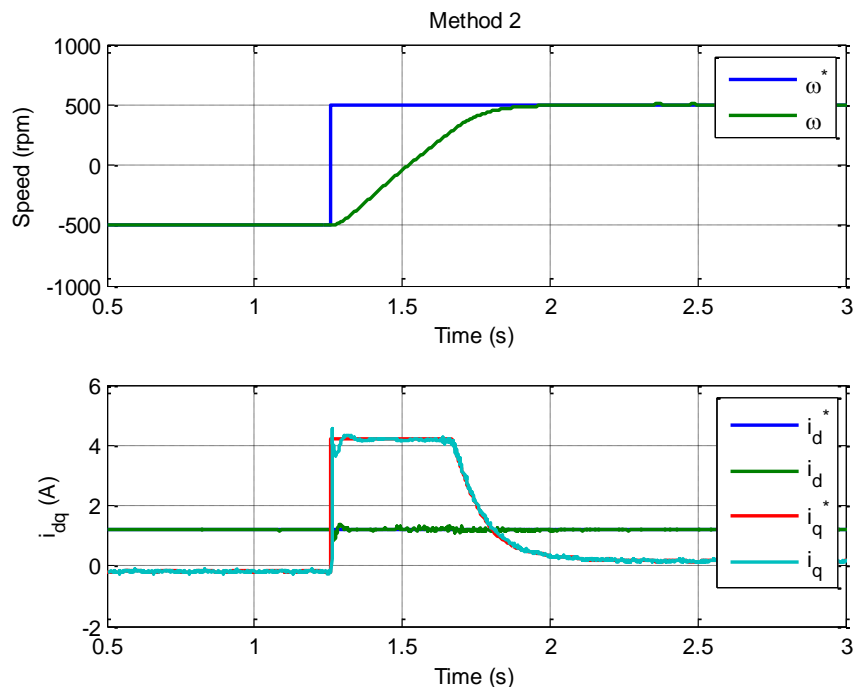


Fig. 5.13. Speed (top) and d - q currents (bottom) variation during no-load speed reversal from -500 rpm to 500 rpm, for faulted six-phase machine controlled using Method 2.

Figs. 5.12 and 5.13 show the same scenario, but for a faulted machine controlled with Method 1 and Method 2, respectively. As observed from the results, dynamic performance of the two approaches is very similar. Generally, good performance, in terms of the speed and current response, is obtained with both the methods.

The experimental results confirm the possible presence of a negative sequence component in the α - β plane, which is related to the neutral point voltage, during an

open-circuit fault. It is also shown that good current control can be achieved via two different approaches: by reducing the neutral point voltage oscillation, or by using dual PI controller for α - β current control. The two tested current control methods provide similar performance, even though the voltage references produced are different.

5.5.2. Comparison of Different Post-fault Operation Scenarios

Since the use of Method 1 has been reported before in (Tani *et al.*, 2012), the subsequent tests related to the comparison of different post-fault operation scenarios are conducted by using Method 2. The same controller structure as in Fig. 5.2(b) can be used for the single neutral case, with an exception that y -current controller should be enabled because i_{ys} is controllable in the single neutral case.

5.5.2.1. Healthy Operation

Fig. 5.14(a) shows the operation of the healthy asymmetrical six-phase machine when running at 250rpm without load. Synchronous PI current controllers (only the positive sequence part) are used for d - q current regulation, while dual PI controllers are used for controlling the x - y currents, with $i_{xs}^* = i_{ys}^* = 0$. As seen from the figure, the phase currents are a balanced set of sinusoidal signals, while the α - β current space vector describes a circular trajectory. The x - y currents are controlled to zero to minimize losses. Under such healthy operation, the machine's speed is regulated at 250 rpm, with slight oscillations caused by the mechanical imperfections.

5.5.2.2. Single Open-circuit Fault

Single open-circuit fault is emulated by removing the connection from VSC to phase- $c2$. Fig. 5.14(b) shows the corresponding operation of the machine without any modification to the current references and the controllers. Since i_{ys}^* is still set to zero, the controller tries to minimize i_{ys} . This causes the disruption of the β current due to the

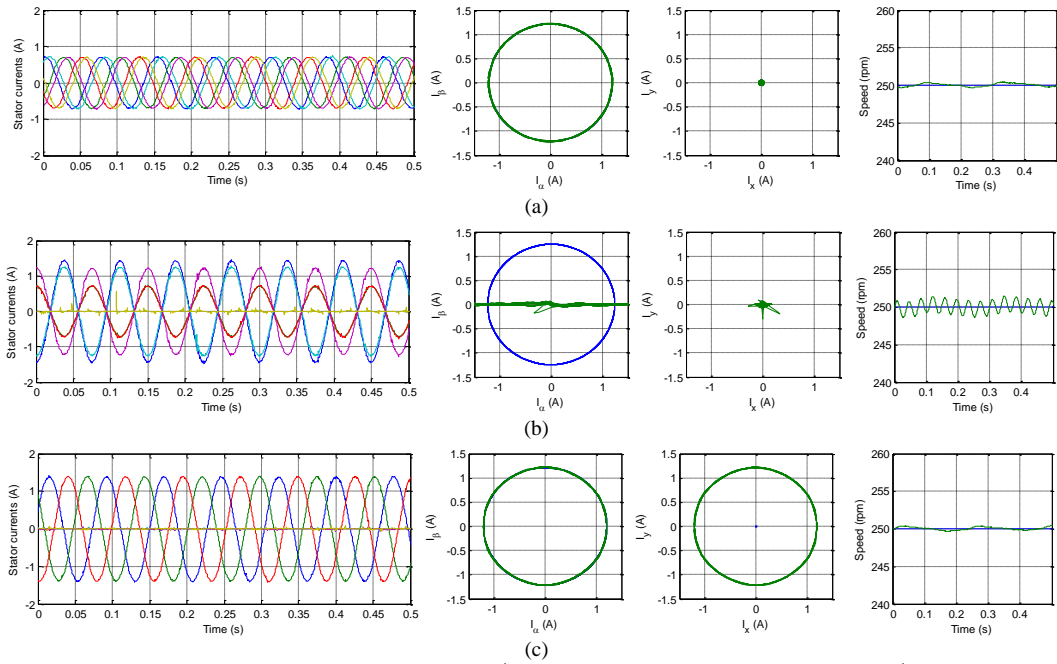


Fig. 5.141. Stator phase currents, α - β currents (blue trace= $i_{\alpha\beta}^*$; green trace= $i_{\alpha\beta}$), x - y currents (blue trace= i_{xy}^* , green trace= i_{xy}) and speed (blue trace= ω_m^* , green trace= ω_m) for (a) healthy machine and faulted machine (b) without modifications of current references ($i_x^* = i_y^* = 0$), (c) with 'single VSC' operation (winding- $a2b2c2$ disconnected). The machine is configured with two isolated neutrals and operates at 250 rpm without load.

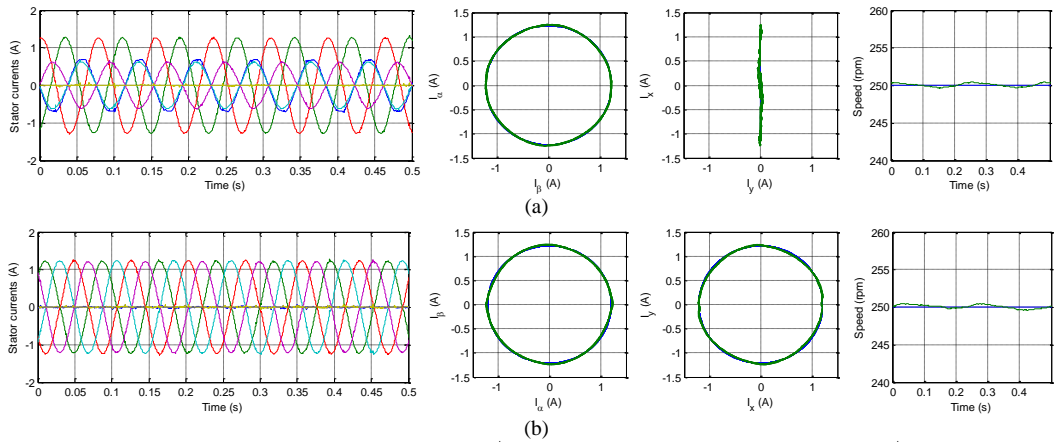


Fig. 5.15. Stator phase currents, α - β currents (blue trace= $i_{\alpha\beta}^*$; green trace= $i_{\alpha\beta}$), x - y currents (blue trace= i_{xy}^* , green trace= i_{xy}) and speed (blue trace= ω_m^* , green trace= ω_m) for faulted machine configured with two isolated neutrals, and controlled using (a) Min Loss and (b) Max Torque mode. The machine operates at 250 rpm without load.

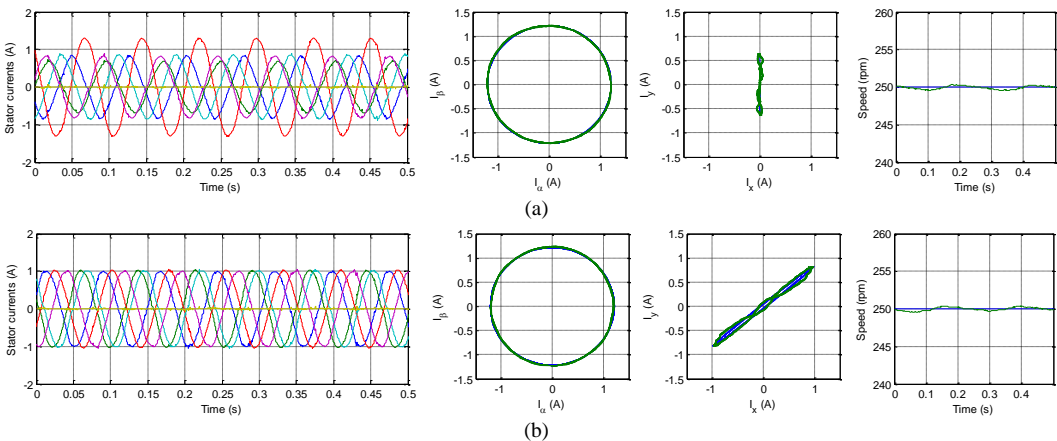


Fig. 5.16. Stator phase currents, α - β currents (blue trace= $i_{\alpha\beta}^*$; green trace= $i_{\alpha\beta}$), x - y currents (blue trace= i_{xy}^* , green trace= i_{xy}) and speed (blue trace= ω_m^* , green trace= ω_m) for faulted machine configured with single isolated neutral, and controlled using (a) Min Loss and (b) Max Torque mode. The machine operates at 250 rpm without load.

coupling between stator y - and β -components. Instead of being regulated to the proper reference, β -current is now almost zero. As a result of the improper control, the machine's speed shows significant oscillations.

Fig. 5.14(c) illustrates the case when the faulted machine operates with a single active VSC ("single VSC" mode). With connections to winding- $a2b2c2$ open-circuited, the machine is practically a three-phase machine with two degrees of freedom, and only the α - β currents can be controlled. Hence, the x - y current controllers are disabled by setting $v_{xs}^* = v_{ys}^* = 0$. The α - β currents now track their references well, producing a circular trajectory that is the same as in the healthy case. The machine now operates at constant speed identical to that of the healthy machine. Even though this provides a simple means of post-fault control, the phase current amplitude in the remaining phases has now doubled. As will be shown later, better performance in terms of achievable torque and stator losses can be obtained using post-fault control strategies discussed in Section 5.3.

5.5.2.3. Post-fault Operation (Two Isolated Neutrals)

Fig. 5.15 shows the post-fault operation of the machine, configured with two isolated neutrals. The α -, β - and x -currents are now regulated with dual PI controllers (using Method 2), while y - and zero-sequence current controllers are disabled ($v_{ys}^* = v_{0+s}^* = v_{0-s}^* = 0$).

Figures 5.15(a) and (b) show the Min Loss and Max Torque modes of post-fault operation, respectively. For the Min Loss mode, the phase currents in the remaining five phases have unequal amplitudes. For the Max Torque mode, currents only flow in four of the remaining five phases, and all have the same amplitude. It can be observed that the maximum phase current amplitude in Max Torque mode is slightly lower than that of the Min Loss mode, which is in agreement with the theoretical analysis in Section IV

(on the values of a_o). Despite the difference in phase current waveforms, both modes of operation have their α - β currents well regulated to the references and the machine's speed remains practically constant, as in the healthy case. The maximum phase current amplitudes for both modes are also lower than in the 'single VSC' mode, suggesting a better performance.

5.5.2.4. Post-fault Operation (Single Isolated Neutral)

The post-fault operation of the six-phase machine configured with single isolated neutral point is depicted in Fig. 5.16, with Figs. 5.16 (a) and (b) showing Min Loss and Max Torque mode, respectively. The controller structure is the same as used for the two neutrals case, except that all four α -, β -, x - and y -currents are controlled, and only the zero-sequence current controllers are disabled ($v_{0+s}^* = v_{0-s}^* = 0$).

Similar to the two neutrals case, the α - β currents are well regulated under both modes and the machine runs at constant speed without obvious oscillations. For the Min Loss mode, the phase currents in the remaining five phases have different amplitudes, with the maximum phase current amplitude slightly higher than in the previous subsection. On the other hand, operation in Max Torque mode yields phase currents of the same amplitude flowing in all the five remaining phases. The maximum phase current amplitude in this mode is found to be the lowest among all the discussed modes.

5.5.2.5. Derated Operation

So far, the results only show that different modes of post-fault operation can be achieved using the current references and controllers discussed in earlier parts of this chapter. Next, the performance in different modes is compared in terms of the achievable torque and stator losses.

Fig. 5.17 shows the relationship between the normalized maximum phase current amplitude and the normalized torque, obtained based on (5.20), (5.23) and

(5.24). With this plot, the achievable torque for different modes can be compared. As discussed earlier, the post-fault torque varies as the machine is derated. For the ‘single VSC’ mode, the maximum achievable torque at rated phase current is found to be only approximately 43% of its rated value. As emphasized in section 5.3, this depends on the ratio i_{dsn}/i_{qsn} of the machine, which in this case is 0.294. This also shows that the common perception that 50% of the rated torque remains for the ‘single VSC’ operation is only valid for permanent magnet machines.

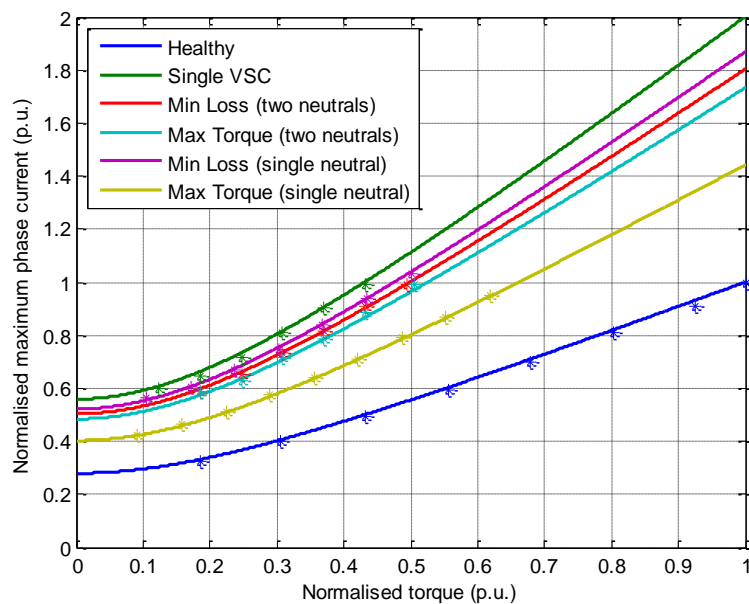


Fig. 5.17. Experimental (*) and theoretical (solid line) plot of the normalized maximum phase current against normalized torque for the asymmetrical six-phase induction machine operating under different post-fault operation modes ($i_{dsn}/i_{qsn} = 0.294$).

Better performance can be obtained if the machine is controlled in Min Loss or Max Torque mode with two isolated neutrals, giving around 50% and 53%, respectively. The improvement provided by Max Torque is only marginal compared to Min Loss mode and the advantage in terms of additional torque can be easily outweighed by the increase in stator losses, as discussed shortly. Finally, the achievable torque is significantly improved, to approximately 66% of the rated value, when operating in Max Torque mode with a single isolated neutral.

The normalized stator losses of the faulted machine under different operating modes are shown in Fig. 5.18. For all cases, the machine is operating at 500 rpm without load. The stator losses are calculated based on (5.26) and normalized using the

mean stator losses for the healthy case. The experimental results (dotted lines) are in full agreement with the theoretical mean (solid lines) values shown in Table 5.2. In terms of stator losses, Min Loss mode for the machine with single neutral gives the best performance. On the other hand, the Max Torque mode in configuration with two neutrals gives the worst performance, with the mean stator winding losses being twice higher than for the healthy case. This is the same as operating the faulted machine in ‘single VSC’ mode. For the machine configured with two isolated neutrals, Min Loss mode gives lower stator winding loss, which is 25% smaller than in the Max Torque mode. Considering that the difference of achievable torque between the two modes is small (only approximately 3%), Min Loss mode is more favourable mode of operation for the configuration with two neutrals.

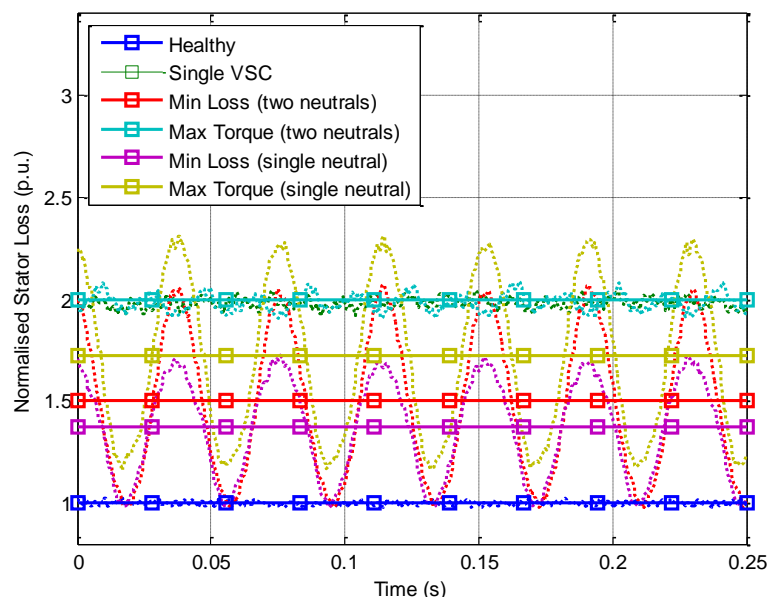


Fig. 5.18. Instantaneous (dotted lines) and theoretical mean (solid lines) of the normalised stator losses, for healthy and faulted asymmetrical six-phase induction machine under different modes of post-fault operation (the theoretical means for ‘single VSC’ and Max Torque (two neutrals) overlap).

Overall, the experimental results clearly show that, in an event of a fault, the single isolated neutral configuration is significantly better than the two isolated neutrals case, both in terms of achievable torque and stator loss minimization. Nevertheless, if configuration with two isolated neutrals is required, say, for safety or electrical isolation purposes, it is better to operate the machine under Min Loss mode.

5.6. Conclusion

This chapter presents the fault tolerant control of an asymmetrical six-phase induction machine in the event of an open-circuit fault. Effect of the fault on the machine equations is analyzed and the corresponding post-fault current references for minimum stator loss and maximum torque are determined. Investigation of the current control of the faulted machine also shows that the open-circuit fault can cause oscillation in neutral point voltage, which introduces additional disturbance voltage that is incapable of being fully compensated by regular linear (PI) controller in the synchronous reference frame. For an n -phase machine driven with n -leg VSC, this disturbance voltage appears as a new degree of freedom. By taking this voltage into consideration, good current regulation can be obtained using different current control methods that utilise dual PI controllers.

Finally, the performance of different modes of post-fault control on the machine configured with single and two isolated neutrals is compared and discussed. Results show that an asymmetrical six-phase machine, with single isolated neutral, provides significantly better performance in terms of fault tolerance than the two isolated neutrals configuration.

Chapter 6

CONCLUSIONS AND FUTURE WORK

6.1. Conclusions

In this thesis, several interesting aspects, related to the control of an asymmetrical six-phase induction machine, have been explored. In Chapter 3, possible ways of mitigating the machine/converter asymmetries and compensating the dead-time effects by means of x - y current control are detailed. By comparing the currents in double- dq model with the currents in VSD model, better understanding regarding the nature of the x - y currents has been obtained for the first time. From the analysis, it is found that the choice of the reference frame for PI controllers used to control the x - y current components has a profound impact on the effectiveness of the control in compensating the machine/converter asymmetries and dead-time effects. Understanding the possible types of asymmetry can help to predetermine the suitable PI controllers to be used. Dead-time compensation using resonant current controllers has also been successfully extended from three-phase machine onto six-phase machine, with its effectiveness validated using experimental results.

In Chapter 4, operation of an asymmetrical six-phase machine with series-connected machine-side converters has been analysed, with the potential merits and demerits of the topology discussed. One important problem of the structure is found to be the dc-link voltage balancing issue. Subsequently, a dc-link voltage balancing

controller, which is superimposed in a cascaded manner onto of the x - y current controllers, is proposed to handle the issue. The effectiveness of the proposed control and the feasibility of the topology are verified by simulation and experimental results. The use of x - y current controllers for this purpose represents an entirely new application of the additional degrees of freedom that exist in multiphase machines.

Finally, Chapter 5 presents studies on post-fault control of an asymmetrical six-phase machine, in an event of an open-circuit fault. Based on the full order decoupling transformation, different modes of post-fault operation are derived and compared. The analysis presented in Chapter 5 also highlights that the open-circuit fault can manifest itself as a disturbance voltage, which degrades the performance of the linear (PI) current controllers. As a way to mitigate this problem, two different current control methods based on PI controllers are suggested and compared. Finally, the comparison of post-fault performance between the six-phase machine configured with two isolated neutrals and that with a single isolated neutral is presented. It was found that the latter configuration provides significantly better performance than the former and is preferred except for applications that specifically require the configuration with two isolated windings.

As a summary, it can be stated that this thesis has provided additional and original contributions, as stated above, to the control of an asymmetrical six-phase induction machine. It is hoped that this additional knowledge can be utilised by future researchers to enhance the control and find more uses of multiphase machines in the real world applications.

6.2. Future Work

Beside the topics covered in this thesis, there remain some potentially important topics related to the control of multiphase machines which are still unexplored. Several possible directions for future research include:

- 1) Parameter estimation of multiphase machines

Although several works on this subject have been reported in the recent literature, there are still knowledge gaps in this area, which need to be filled. In particular, the parameter estimation methods, presented so far, have always been based on a fundamental assumption that the mutual leakage inductance between two three-phase windings of the machine is negligible, so that the stator leakage inductances in α - β and x - y planes are equal ($L_{ls_ \alpha\beta} = L_{ls_ xy}$). However, such assumption can only be valid for certain types of the winding structure. Hence, a more universal experimental approach of determining machine parameters, regardless of the winding structure, is yet to be reported. As accurate machine parameters are crucial, especially for high performance drives, parameter estimation for multiphase machine can be important topic for future research.

- 2) Extension of control concepts to machines with other phase number

The investigations presented in this thesis have been based solely on an asymmetrical six-phase induction machine. For the case of x - y current control methods and operation with series-connected converters, similar concepts should be applicable to other multiphase machines with multiple three-phase windings. It would be interesting to see how the control concepts could be extended to machines with, for example, nine or twelve phases

- 3) Post-fault control of multiphase machine with alternative winding configurations

The post-fault control studies presented in Chapter 5 are for a six-phase machine with star-connected stator windings. In some recent works, the fault-tolerance of machines with alternative winding configurations, such as delta or pentacle connections, has been investigated. The fault-tolerance of a six-phase machine with alternative winding configurations (such as an equivalent of the delta connection for a six-phase system) could be explored to provide a complete picture on the fault-tolerant capability of the machine.

4) Post-fault control of series-connected topology

Even though the series-connection topology presented in Chapter 4 appears to be an interesting and beneficial, the fault tolerance of the system has not been properly addressed. Based on the analysis presented in Chapter 4, it is anticipated that the topology does not perform well in the case of a fault. In an event of an open-circuit fault on one of the phases, the affected three-phase winding will be immediately reduced to a single phase system. The active power associated with the VSC of the faulted winding will then be oscillating at twice the fundamental frequency, due to the single phase operation of the faulted winding. Based on the understanding of the relation between active power and dc-link voltage, it is expected that oscillations will appear in dc-link voltage as well. Hence, the structure is not immediately fault-tolerant. It is expected that in order to mitigate the power oscillation problem, some modifications to the series-connection topology, such as the use of open winding configuration or parallel VSCs, are required. Thus, investigation on the post-fault control of the series-connection topology serves as an interesting subject for future study.

References

- Aboelhassan, M.O.E., Raminosoa, T., Goodman, A., De Lillo, L., Gerada, C., 2013. Performance evaluation of a vector-control fault-tolerant flux-switching motor drive. , 60(8), pp.2997–3006.
- Abdelkhalik, A., Masoud, M. and Barry, W., 2010. Eleven-phase induction machine: steady-state analysis and performance evaluation with harmonic injection. *IET Electric Power Applications*, 4(8), pp.670–685.
- Abdel-Khalik, A.S., Morsy, A. S., Ahmed, S., Massoud, A. M. 2013. Effect of stator winding connection on performance of five-phase induction machines. *IEEE Trans. on Industrial Electronics*, (EARLY ACCESS, d.o.i: 10.1109/TIE.2013.2242417).
- Abu-Rub, Holtz, J., Rodriguez, J., Baoming, G., 2010. Medium-voltage multilevel converters - state of the art, challenges, and requirements in industrial applications. *IEEE Trans. on Industrial Electronics*, 57(8), pp.2581–2596.
- Alberti, L. and Bianchi, N., 2012. Experimental tests of dual three-phase induction motor under faulty operating condition. *IEEE Trans. on Industrial Electronics*, 59(5), pp.2041–2048.
- Andresen, B. and Birk, J., 2007. A high power density converter system for the Gamesa G10x 4,5 MW wind turbine. In *Proc. European Conf. on Power Electronics and Applications EPE*. Aalborg, Denmark, CD-ROM..
- Apsley, J.M., 2010. Open-circuit fault mitigation for multiphase induction motors with a unified control structure. In *IET Int. Conf. on Power Electronics, Machines and Drives PEMD*. Brighton, UK, CD-ROM.
- Apsley, J. and Williamson, S., 2006. Analysis of multiphase induction machines with winding faults. *IEEE Trans. on Industry Applications*, 42(2), pp.465–472.
- Barcaro, M., Bianchi, N. and Magnussen, F., 2010. Analysis and tests of a dual three-phase 12-slot 10-pole permanent magnet motor. *IEEE Trans. on Industrial Applications*, 46(6), pp.2355–2362.
- Barcaro, M., Bianchi, N. and Magnussen, F., 2011. Six-phase supply feasibility using a PM fractional-slot dual winding machine. *IEEE Trans. on Industry Applications*, 47(5), pp.2042–2050.
- Barrero, F. Arahall, M. R., Gregor, R., Toral, S., Durán, Mario, J., 2009. A proof of concept study of predictive current control for VSI-driven asymmetrical dual three-phase AC machines. *IEEE Trans. on Industrial Electronics*, 56(6), pp.1937–1954.

- Barrero, F., Prieto, J., Levi, E., Gregor, R., Toral, S., Durán, M. J., Jones, M., 2011. An enhanced predictive current control method for asymmetrical six-phase motor drives. *IEEE Trans. on Industrial Electronics*, 58(8), pp.3242–3252.
- Baudart, F., Dehez, B., Matagne, E., Telteu-Nedelcu, D., Alexandre, P., Labrique, F., 2012. Torque control strategy of polyphase permanent-magnet synchronous machines with minimal controller reconfiguration under open-circuit fault of one phase. *IEEE Trans. on Industrial Electronics*, 59(6), pp.2632–2644.
- Bennett, J.W., Mecrow, B.C., Atkinson, D.J., Atkinson, G.J., 2011. Safety-critical design of electromechanical actuation systems in commercial aircraft. *IET Electric Power Applications*, 5(1), pp.37–47.
- Birk, J. and Andresen, B., 2007. Parallel-connected converters for optimizing efficiency, reliability and grid harmonics in a wind turbine. In *Proc. European Conf. on Power Electronics and Applications EPE*. Aalborg, Denmark, CD-ROM.
- Bodo, N., Levi, E. and Jones, M., 2013. Investigation of carrier-based PWM techniques for a five-phase open-end winding drive topology. *IEEE Trans. on Industrial Electronics*, 60(5), pp.2054–2065.
- Bojoi, R., 2002. *Analysis, design and implementation of a dual three-phase vector controlled induction motor drive*. Ph.D dissertation, Politecnico Di Torino, Italy.
- Bojoi, R., Tenconi, A., Profumo, F., Griva, G., Martinello, D., 2002. Complete analysis and comparative study of digital modulation techniques for dual three-phase AC motor drives. In *IEEE Power Electronics Specialists Conference PESC*. Cairns, Queensland, Australia: Ieee, pp. 851–857.
- Bojoi, R., Farina, F., Lazzari, M., Profumo, F., Tenconi, A., 2003a. Analysis of the asymmetrical operation of dual three-phase induction machines. In *IEEE Int. Electric Machines and Drives Conference IEMDC*. Madison, Wisconsin USA, pp. 429–435.
- Bojoi, R., Lazzari, M., Profumo, F., Tenconi, A., 2003b. Digital field-oriented control for dual three-phase induction motor drives. *IEEE Trans. on Industry Applications*, 39(3), pp.752–760.
- Bojoi, R., Profumo, F. and Tenconi, A., 2003c. Digital synchronous frame current regulation for dual three-phase induction motor drives. In *IEEE Conf. on Power Electronics Specialist PESC*. Acapulco, Mexico: Ieee, pp. 1475–1480.
- Bojoi, R., Farina, F., Griva, G., Profumo, F., Tenconi, A., 2005a. Direct torque control for dual three-phase induction motor drives. *IEEE Trans. on Industry Applications*, 41(6), pp.1627–1636.
- Bojoi, R., Griva, G., Bostan, V., Guerriero, M., Farina, F., Profumo, F., 2005b. Current control strategy for power conditioners using sinusoidal signal integrators in synchronous reference frame. *IEEE Trans. on Power Electronics*, 20(6), pp.1402–1412.

- Bojoi, R., Levi, E., Farina, F., Tenconi, A., Profumo, F., 2006. Dual three-phase induction motor drive with digital current control in the stationary reference frame. *IEE Proceedings - Electric Power Application*, 153(1), pp.129–139.
- Bojoi, R., Limongi, L. R., Profumo, F., Roiu, D., Tenconi, A., 2009. Analysis of current controllers for active power filters using selective harmonic compensation schemes. *IEEE Trans. on Electrical and Electronic Engineering*, 4(2), pp.139–157.
- Brisset, S., Vizireanu, D. and Brochet, P., 2008. Design and optimization of a nine-phase axial-flux PM synchronous generator with concentrated winding for direct-drive wind turbine. *IEEE Trans. on Industry Applications*, 44(3), pp.707–715.
- Bu, F., Huang, W., Hu, Y., Shi, K., 2012a. An integrated AC and DC hybrid generation system using dual-stator-winding induction generator with static excitation controller. *IEEE Trans. on Energy Conversion*, 27(3), pp.810–812.
- Bu, F., Huang, W., Hu, Y., Shi, J., Shi, K., 2012b. A stand-alone dual stator-winding induction generator variable frequency AC power system. *IEEE Trans. on Power Electronics*, 27(1), pp.10–13.
- Che, H.S., Duran, M. J., Hew, W. P., Rahim, N. A., Levi, E., Jones, M., 2012a. Dc-link voltage balancing of six-phase wind energy systems with series-connected machine-side converters and NPC grid-side converter. In *Annual Conference of IEEE Industrial Electronics Society IECON*. Montreal, Canada, pp. 3541–3546.
- Che, H.S., Hew, W. P., Rahim, N. A., Levi, E., Jones, M., Duran, M. J., 2012c. Current control of a six-phase induction generator for wind energy plants. In *International Power Electronics and Motion Control Conference, EPE-PEMC ECCE Europe*. Novi Sad, Serbia, CD-ROM.
- Che, H.S., Hew, W. P., Rahim, N. A., Levi, E., Jones, M., Duran, M. J., 2012b. A six-phase wind energy induction generator system with series-connected DC-links. In *IEEE Power Electronics for Distributed Generation Systems PEDG*. Aalborg, Denmark, pp. 26–33.
- Che, H.S., Duran, M.J., E. Levi, Jones, M., Hew, W.P., Rahim, N.A., 2013a Post-fault operation of an asymmetrical six-phase induction machine with single and two isolated neutral points. In *IEEE Energy Conversion Congress and Exposition, ECCE*, Denver, Colorado, USA. (Accepted)
- Che, H.S., Levi, E., Jones, M., Duran, M., Hew, W. P., Rahim, N.A., 2013b. Operation of a six-phase induction machine using series-connected machine-side converters. *IEEE Trans. on Industrial Electronics*, (EARLY ACCESS, d.o.i: 10.1109/TIE.2013.2248338).
- Che, H.S., Levi, E., Jones, M., Hew, W. P., Rahim, N. A., 2013c. Current control methods for an asymmetrical six- phase induction motor drive. *IEEE Trans. on Power Electronics*, (EARLY ACCESS, d.o.i: 10.1109/TPEL.2013.2248170)
- Di Gerlando, A., Foglia, G., Iacchetti, M. F., Perini, R., 2012. Analysis and test of diode rectifier solutions in grid-connected wind energy conversion systems employing

- modular permanent-magnet synchronous generators. *IEEE Trans. on Industrial Electronics*, 59(5), pp.2135–2146.
- Dordevic, O., Jones, M. and Levi, E., 2013a. A comparison of carrier-based and space vector PWM techniques for three-level five-phase voltage source inverters. *IEEE Trans. on Industrial Informatics*, 9(2), pp.609–619.
- Dordevic, O., Levi, E. and Jones, M., 2013b. A vector space decomposition based space vector PWM algorithm for a three-level seven-phase voltage source inverter. *IEEE Trans. on Power Electronics*, 28(2), pp.637–649.
- Dujic, D., Grandi, G., Jones, M., Levi, E., 2008. A space vector PWM scheme for multifrequency output voltage generation with multiphase voltage-source inverters. *IEEE Trans. on Industrial Electronics*, 55(5), pp.1943–1955.
- Duran, M.J., Kouros, S., Wu, B., Levi, E., Barrero, F., Alepuz, S., 2011. Six-phase PMSG wind energy conversion system based on medium-voltage multilevel converter. In *Proc. European Conference on Power Electronics and Applications EPE*. Birmingham, UK, p. CD-ROM.
- Duran, M.J., Riveros, J. A., Barrero, F., Guzmán, H., Prieto, J., 2012. Reduction of common-mode voltage in five-phase induction motor drives using predictive control techniques. *IEEE Trans. on Industry Applications*, 48(6), pp.2059–2067.
- Duran, M.J., Prieto, J., Barrero, F., Riveros, J. A., Guzman, H., 2013. Space vector PWM with reduced common-mode voltage for five-phase induction motor drives. *IEEE Trans. on Industrial Electronics*. (EARLY ACCESS, d.o.i: 10.1109/TIE.2012.2217719).
- Dwari, S. and Parsa, L., 2008. An optimal control technique for multiphase PM machines under open-circuit faults. *IEEE Trans. on Industrial Electronics*, 55(5), pp.1988–1995.
- Dwari, S. and Parsa, L., 2011. Fault-tolerant control of five-phase permanent-magnet motors with trapezoidal back EMF. *IEEE Trans. on Industrial Electronics*, 58(2), pp.476–485.
- Fnaiech, M.A., Betin, F., Capolino, G.-A., Fnaiech, F., 2010. Fuzzy logic and sliding-mode controls applied to six-phase induction machine with open phases. *IEEE Trans. on Industrial Electronics*, 57(1), pp.354–364.
- Fu, J.-R. and Lipo, T.A., 1994. Disturbance-free operation of a multiphase current-regulated motor drive with an opened phase. *IEEE Trans. on Industry Applications*, 30(5), pp.1267–1274.
- Gjerde, S.S., Olsen, P.K. and Undeland, T.M., 2012. A transformerless generator-converter concept making feasible a 100 kV low weight offshore wind turbine part II - The converter. In *IEEE Energy Conversion Congress and Exposition ECCE*. Raleigh, North Carolina, USA, pp. 253–260.

- Gjerde, S.S. and Undeland, T.M., 2012. A modular series connected converter for a 10 MW, 36 kV, transformer-less offshore wind power generator drive. *Energy Procedia*, 24, pp.68–75.
- Gonzalez, J., Ignacio, J., Birk, J., Andersen, B., 2006. *Method of operation of a converter system*. European patent EP1768223 A2.
- Grandi, G., Sanjeevikumar, P., Gritli, Y., Filippetti, F., 2012. Fault-tolerant control strategies for quad inverter induction motor drives with one failed inverter. In *Int. Conf. on Electrical Machines ICEM*. Marseille, France, pp. 959–966.
- Grandi, G., Gritli, Y., Filippetti, F., Rossi, C., 2011. Fault-tolerant operating analysis of a quad-inverter multiphase multilevel AC motor drive. In *IEEE Symposium on Diagnostics for Electrical Machines, Power Electronics & Drives SIBIRCON*. Bologna, Italy, pp. 126–132.
- Gregor, R., Barrero, F., Toral, S.L., Duran, M.J., Arahal, M.R., Prieto, J., Mora, J.L., 2010. Predictive-space vector PWM current control method for asymmetrical dual three-phase induction motor drives. *IET Electric Power Applications*, 4(1), p.26.
- Guerrero, J.M., Leetmaa, M., Briz, F., Zamarrón, A., Lorenz, R. D., 2005. Inverter nonlinearity effects in high-frequency signal-injection-based sensorless control methods. *IEEE Trans. on Industry Applications*, 41(2), pp.618–626.
- Guzman, H., Duran, M. J., Barrero, F., Toral, S., 2011. Fault-tolerant current predictive control of five-phase induction motor drives with an open phase. In *IECON 2011 - 37th Annual Conference of the IEEE Industrial Electronics Society*. Melbourne, Australia, pp. 3680–3685.
- Hadiouche, D., Razik, H. and Rezzoug, A., 2004. On the modeling and design of dual-stator windings to minimize circulating harmonic currents for VSI fed AC machines. *IEEE Trans. on Industry Applications*, 40(2), pp.506–515.
- Hadiouche, D., Baghli, L. and Rezzoug, A., 2006. Space-vector PWM techniques for dual three-phase AC machine: analysis, performance evaluation, and DSP implementation. *IEEE Trans. on Industry Applications*, 42(4), pp.1112–1122.
- Han, S.-H. Jo, T.-H., Park, J.-H., Kim, H.-G., Chun, T.-W., Nho, E.-C., 2011. Dead time compensation for grid-connected PWM inverter. In *8th Int. Conf. on Power Electronics - ECCE Asia*. Jeju, South Korea: Ieee, pp. 876–881.
- Hassanain, N.E.A.M. and Fletcher, J.E., 2010. Steady-state performance assessment of three- and five-phase permanent magnet generators connected to a diode bridge rectifier under open-circuit faults. *IET Renewable Power Generation*, 4(5), pp.420–427.
- Herran, M.A., Fischer, J. R., Gonzalez, A., Judewicz, M. G., Carrica, D. O., 2013. Adaptive dead-time compensation for grid-connected PWM inverters of single-stage PV systems. *IEEE Trans. on Power Electronics*, 28(6), pp.2816–2825.
- Hwang, S. and Kim, J., 2010. Dead time compensation method for voltage-fed PWM inverter. *IEEE Trans. on Energy Conversion*, 25(1), pp.1–10.

- Jacobina, C.B. et al., 2002. On-line estimation of the stator resistance of a six-phase induction machine. In *IEEE Industry Applications Conference IAS*. Pittsburgh, Pennsylvania, USA, pp. 746–751.
- Jeong, S. and Park, M., 1991. The analysis and compensation of dead-time effects in PWM inverters. *IEEE Trans. on Industrial Electronics*, 38(2), pp.108–114.
- Jones, M., Vukosavic, S. N., Levi, E., Iqbal, A., 2005. A six-phase series-connected two-motor drive with decoupled dynamic control. *IEEE Trans. on Industry Applications*, 41(4), pp.1056–1066.
- Jones, M., Vukosavic, S.N., Dujic, D., Levi, E., 2009. A synchronous current control scheme for multiphase induction motor drives. *IEEE Trans. on Energy Conversion*, 24(4), pp.860–868.
- Jones, M., Satiawan, I. N. W., Bodo, N., Levi, E., 2012. A dual five-phase space-vector modulation algorithm based on the decomposition method. *IEEE Trans. on Industry Applications*, 48(6), pp.2110–2120.
- Jung, E., Yoo, H., Sul, S.-K., Choi, H.-S., Choi, Y.-Y., 2012. A nine-phase permanent-magnet motor drive system for an ultrahigh-speed elevator. *IEEE Trans. on Industry Applications*, 48(3), pp.987–995.
- Kianinezhad, R., Nahid-Mobarakeh, B., Baghli, L., Betin, F., Capolino, G.-A., 2008. Modeling and Control of Six-Phase Symmetrical Induction Machine Under Fault Condition Due to Open Phases. *IEEE Trans. on Industrial Electronics*, 55(5), pp.1966–1977.
- Kouro, S., Rodriguez, J., Wu, B., Bernet, S., Perez, M., 2012. Powering the future of industry: High-power adjustable speed drive topologies. *IEEE Industry Applications Magazine*, 18(4), pp.26–39.
- Lascu, C., Asiminoaei, L., Boldea, I., Blaabjerg, F., 2007. High performance current controller for selective harmonic compensation in active power filters. *IEEE Trans. on Power Electronics*, 22(5), pp.1826–1835.
- Li, X. and Malik, O.P., 1994. Performance of a double-star synchronous generator with bridge rectified output. *IEEE Trans. on Energy Conversion*, 9(3), pp.613–619.
- Lim, C.S., Levi, E., Jones, M., Rahim, N. A., Hew, W. P., 2013. FCS-MPC based current control of a five-phase induction motor and its comparison with PI-PWM control. *IEEE Trans. on Industrial Electronics*. (EARLY ACCESS, d.o.i: 10.1109/TIE.2013.2248334)
- Limongi, L.R., Bojoi, R., Griva, G., Tenconi, A., 2009. Digital current-control schemes. *IEEE Industrial Electronics Magazine*, 3(1), pp.20–31.
- Liserre, M., Cárdenas, R., Molinas, M., Rodríguez, J., 2011. Overview of multi-MW wind turbines and wind parks. *IEEE Trans. on Industrial Electronics*, 58(4), pp.1081–1095.

- Levi, E., Jones, M., Vukosavic, S. N., Toliyat, H. A., 2004a. A novel concept of a multiphase , multimotor vector controlled drive system supplied from a single voltage source inverter. *IEEE Trans. on Power Electronics*, 19(2), pp.320–335.
- Levi, E., Jones, M., Vukosavic, S. N., Toliyat, H. A., 2004b. Operating principles of a novel multiphase vector-controlled drive. *IEEE Trans. on Energy Conversion*, 19(3), pp.508–517.
- Levi, E., Vukosavic, S.N. and Jones, M., 2005. Vector control schemes for series-connected six- phase two-motor drive systems. *IEE Proc. - Electric Power Applications*, 152(2).
- Levi, E., Jones, M. and Vukosavic, S.N., 2006. A series-connected two-motor six-phase drive with induction and permanent magnet machines. *IEEE Trans. on Energy Conversion*, 21(1), pp.121–129.
- Levi, E., Bojoi, R., Profumo, F., Toliyat, H.A., Williamson, S., 2007a. Multiphase induction motor drives – a technology status review. *IET Electric Power Applications*, 1(4), pp.489–516.
- Levi, E., Jones, M., Vukosavic, S. N., Iqbal, A., Toliyat, H. A., 2007b. Modeling, control, and experimental investigation of with single inverter supply. *IEEE Trans. on Industrial Eelctronics*, 54(3), pp.1504–1516.
- Levi, E., 2008. Multiphase electric machines for variable-speed applications. *IEEE Trans. on Industrial Electronics*, 55(5), pp.1893–1909.
- Levi, E., Satiawan, I. N. W., Bodo, N., Jones, M., 2012. A space-vector modulation scheme for multilevel open-end winding five-phase drives. *IEEE Trans. on Energy Conversion*, 27(1), pp.1–10.
- Lipo, T.A., 1980. A d-q model for six phase induction machines. In *Int. Conf. on Electrical Machines ICEM*. Athens, Greece, pp. 860–867.
- Locment, F., Semail, E. and Kestelyn, X., 2008. Vectorial approach-based control of a seven-phase axial flux machine designed for fault operation. *IEEE Trans. on Industrial Electronics*, 55(10), pp.3682–3691.
- Marouani, K., Baghli, L., Hadiouche, D., Kheloui, A., Rezzoug, A., 2008. A new PWM strategy based on a 24-sector vector space decomposition for a six-phase VSI-fed dual stator induction motor. *IEEE Trans. on Industrial Electronics*, 55(5), pp.1910–1920.
- Mendes, A.M.S. and Cardoso, A.J.M., 2006. Fault-tolerant operating strategies applied to three-phase induction-motor drives. *IEEE Trans. on Industrial Electronics*, 53(6), pp.1807–1817.
- Miranda, R.S., Toliyat, H. A., Jacobina, C. B., Lima, A. M. N., 2007. Short-Circuit Fault Mitigation in Six-Phase Induction Machine Drives. *2007 IEEE Vehicle Power and Propulsion Conference*, pp.370–376.

- Mohammadpour, A. and Parsa, L., 2013. A unified fault-tolerant current control approach for five-phase PM motors with trapezoidal back EMF under different stator winding connections. *IEEE Trans.on Power Electronics*, 28(7), pp.3517–3527.
- Munoz, A.R. and Lipo, T.A., 2000. Dual stator winding induction machine drive. *IEEE Trans. on Industry Applications*, 36(5), pp.1369–1379.
- Ng, C.H., Parker, M.A., Ran, L., Tavner, P.J., Bumby, J.R., Spooner, E., 2008. A multilevel modular converter for a large, light weight wind turbine generator. *IEEE Trans. on Power Electronics*, 23(3), pp.1062–1074.
- Olsen, P.K., Gjerde, S., Nilssen, R. M., Hoelto, J., Hvidsten, S., 2012. A transformerless generator-converter concept making feasible a 100 kV light weight offshore wind turbine: part I - The generator. In *IEEE Energy Conversion Congress and Exposition ECCE*. Raleigh, North Carolina, USA, pp. 247–252.
- Parker, M.A., Ng, C. and Ran, L., 2011. Fault-tolerant control for a modular generator-converter scheme for direct-drive wind turbines. *IEEE Trans. on Industrial Electronics*, 58(1), pp.305–315.
- Parker, M.A., Ran, L. and Finney, S.J., 2013. Distributed control of a fault-tolerant modular inverter for direct-drive wind turbine grid interfacing. *IEEE Trans. on Industrial Electronics*, 60(2), pp.509–522.
- Parker, M.A., Ran, L. and Finney, S.J., 2013. Distributed control of a fault-tolerant modular inverter for direct-drive wind turbine grid interfacing. *IEEE Trans. on Industrial Electronics*, 60(2), pp.509–522.
- Parsa, L. and Toliyat, H. A., 2007. Fault-tolerant interior-permanent-magnet machines for hybrid electric vehicle applications. *IEEE Trans. on Vehicular Technology*, 56(4), pp. 1546–1552.
- Lyra, R.O.C. and Lipo, T.A., 2002. Torque density improvement in a six-phase induction motor with third harmonic current injection. *IEEE Trans. on Industry Applications*, 38(5), pp.1351–1360.
- Riveros, J.A., Yepes, A. G., Barrero, F., Doval-Gandoy, J., Bogado, B., Lopez, O., Jones, M., Levi, E., 2012. Parameter identification of multiphase induction machines with distributed windings — Part 2: time-domain techniques. *IEEE Trans. on Energy Conversion*, pp.1–11.
- Riveros, J.A., Barrero, F., Levi, E., Durán, M. J., Toral, S., Jones, M., 2013. Variable-speed five-phase induction motor drive based on predictive torque control. *IEEE Trans. on Industrial Electronics*, 60(8), pp.2957–2968.
- Ruba, M. and Fodorean, D., 2012. Analysis of fault-tolerant multiphase power converter for a nine-phase permanent magnet synchronous machine. *IEEE Trans. on Industry Application*, 48(6), pp.2092–2101.

- Ryu, H., Kim, J. and Sul, S., 2006. Synchronous-frame current control of multiphase synchronous motor under asymmetric fault condition due to open phases. *IEEE Trans. on Industrial Applications*, 42(4), pp. 1062–1070.
- Shamsi-Nejad, M.-A., Nahid-Mobarakeh, B., Pierfederici, S., Meibody-Tabar, F., 2008. Fault tolerant and minimum loss control of double-star synchronous machines under open phase conditions. *IEEE Trans. on Industrial Electronics*, 55(5), pp.1956–1965.
- Simoes, M.G. and Vieira, P., 2002. A high-torque low-speed multiphase brushless machine-a perspective application for electric vehicles. *IEEE Trans. on Industrial Electronics*, 49(5), pp.1154–1164.
- Singh, G.K., Nam, K. and Lim, S.K., 2005. A simple indirect field-oriented control scheme for multiphase induction machine. *IEEE Trans. on Industrial Electronics*, 52(4), pp.1177–1184.
- Singh, G.K., Senthil Kumar, A. and Saini, R.P., 2010. Selection of capacitance for self-excited six-phase induction generator for stand-alone renewable energy generation. *Energy*, 35(8), pp.3273–3283.
- Spooner, E., Gordon, P., Bumby, J. R., French, C. D., 2005. Lightweight ironless-stator PM generators for direct- drive wind turbines. *IEE Proc. Electric Power Applications*, 152(1), pp.17–26.
- Sun, X., Huang, D. and Wu, G., 2012. The current state of offshore wind energy technology development. *Energy*, 41(1), pp.298–312.
- Sayed-Ahmed, A. and Demerdash, N.A.O., 2012. Fault-tolerant operation of delta-connected scalar- and vector-controlled AC motor drives. *IEEE Trans. on Power Electronics*, 27(6), pp.3041–3049.
- Tani, A., Mengoni, M., Zarri, L., Serra, G., Casadei, D., 2012. Control of multiphase induction motors with an odd number of phases under open-circuit phase faults. *IEEE Trans. on Power Electronics*, 27(2), pp.565–577.
- Vaseghi, B., Takorabet, N., Caron, J. P., Nahid-Mobarakeh, B., Meibody-Tabar, F., Humbert, G., 2011. Study of different architectures of fault-tolerant actuator using a two-channel PM motor. *IEEE Trans. on Industry Applications*, 47(1), pp.47–54.
- Villani, M., Tursini, M., Fabri, G., Castellini, L., 2012. High reliability permanent magnet brushless motor drive for aircraft application. *IEEE Trans. on Industrial Electronics*, 59(5), pp.2073–2081.
- Vukosavic, S.N., Jones, M., Levi, Emil, Varga, J., 2005. Rotor flux oriented control of a symmetrical six-phase induction machine. *Electric Power Systems Research*, 75(2-3), pp.142–152.
- Wang, Y., Gao, Q. and Cai, X., 2011. Mixed PWM for dead-time elimination and compensation in a grid-tied inverter. *IEEE Trans. on Industrial Electronics*, 58(10), pp.4797–4803.

- Wang, X., Zhong, Q., Deng, Z., Yue, S., 2012. Current-controlled multiphase slice permanent magnetic bearingless motors with open-circuited phases : fault-tolerant controllability and its verification. *IEEE Trans. on Industrial Electronics*, 59(5), pp.2059–2072.
- Welchko, B.A., Lipo, T. A., Jahns, T. M., Schulz, S. E., 2004. Fault tolerant three-phase AC motor drive topologies : a comparison of features , cost , and limitations. *IEEE Trans. on Power Electronics*, 19(4), pp.1108–1116.
- Wu, Z., Ojo, O., Sastry, J., 2007. High-Performance Control of a Dual Stator Winding DC Power Induction Generator. *IEEE Trans. on Industry Applications*, 43(2), pp.582–592.
- Wu, B., Lang, Y., Zargari, N., Kouro, S., 2011. *Power conversion and control of wind energy systems*, Hoboken, NJ: IEEE Press - John Wiley and Sons.
- Xiang-Jun, Z., Yongbing, Y., Hongtao, Z., Ying, L., Luguang, F., Xu, Y., 2012. Modelling and control of a multi-phase permanent magnet synchronous generator and efficient hybrid 3L-converters for large direct-drive wind turbines. *IET Electric Power Applications*, 6(6), pp.322–331.
- Yepes, A.G., Freijedo, F. D., Doval-Gandoy, J., Lopez, O., Malvar, J., Fernandez-Comesana, P., 2010. Effects of discretization methods on the performance of resonant controllers. *IEEE Trans. on Power Electronics*, 25(7), pp.1692–1712.
- Yepes, A.G., Freijedo, F. D., Lopez, O., Doval-Gandoy, J., 2011a. Analysis and design of resonant current controllers for voltage-source converters by means of Nyquist diagrams and sensitivity function. *IEEE Trans. on Industrial Electronics*, 58(11), pp.5231–5250.
- Yepes, A.G., Freijedo, F. D., Lopez, O., Doval-Gandoy, J., 2011b. High-performance digital resonant controllers implemented with two integrators. *IEEE Trans. on Power Electronics*, 26(2), pp.563–576.
- Yepes, A.G., Riveros, J. A., Barrero, F, Oscar, L., Jones, M., Levi, E., 2012. Parameter identification of multiphase induction machines with distributed windings — Part 1 : sinusoidal excitation methods. *IEEE Trans. on Energy Conversion*, pp.1–11.
- Yuan, X., Chai, J. and Li, Y., 2012. A transformer-less high-power converter for large permanent magnet wind generator systems. *IEEE Trans. on Sustainable Energy*, 3(3), pp.318–329.
- Zarri, L., Mengoni, M., Gritli, Y., Tani, A., Filippetti, F., Serra, G., Casadei, D., 2013. Detection and localization of stator resistance dissymmetry based on multiple reference frame controllers in multiphase induction motor drives. *IEEE Trans. on Industrial Electronics*, 60(8), pp.3506–3518.
- Zhang, Z., Yan, Y., Yang, S., Bo, Z., 2009. Development of a new permanent-magnet BLDC generator using 12-phase half-wave rectifier. *IEEE Trans. on Industrial Electronics*, 56(6), pp.2023–2029

- Zhao, Y. and Lipo, T.A., 1995. Space vector PWM control of dual three-phase induction machine using vector space decomposition. *IEEE Trans. on Industry Applications*, 31(5), pp.1100–1109.
- Zhao, Y. and Lipo, T.A., 1996a. Modeling and control of a multi-phase induction machine with structural unbalance - Part I. Machine modeling and multi-dimensional current regulation. *IEEE Trans. on Energy Conversion*, 11(3), pp. 570–577.
- Zhao, Y. and Lipo, T.A., 1996b. Modeling and control of a multi-phase induction machine with structural unbalance - Part II. Field-oriented control and experimental verification. *IEEE Trans. on Energy Conversion*, 11(3), pp. 578–584.

Appendix A

SIMULATION MODEL IN MATLAB/SIMULINK ENVIRONMENT

A.1. Introduction

In this thesis, a simulation model has been developed in the Matlab/Simulink environment, to simulate the system shown in Fig. A.1. The simulation model serves as a platform for developing the control algorithms for the six-phase machine, and is also used to run preliminary tests before the actual experiments are conducted.

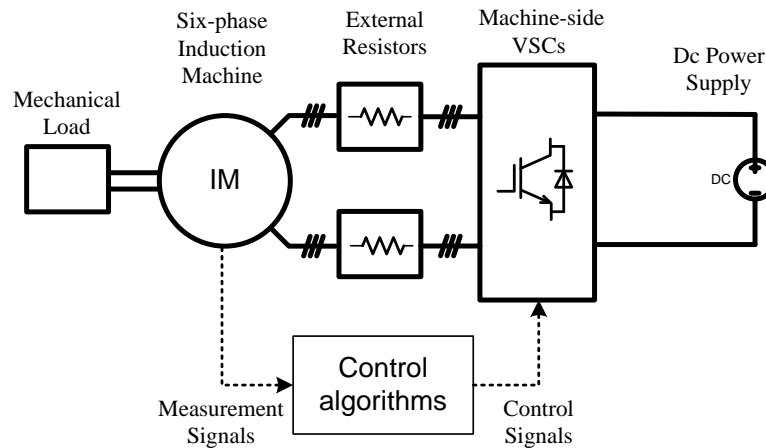


Fig. A.1. Overview of the system simulated in Matlab/Simulink.

Based on the Fig. A.1, it can be observed that the simulation model basically consists of a six-phase induction machine, fed by the machine-side VSCs and mechanically coupled to a load. The machine-side VSCs are two two-level three-phase VSCs which can be configured to be in parallel or in series, depending on the

application. The dc-side of the VSCs is connected to a dc-power supply which keeps the dc-link voltage at a constant value. In order to emulate the effect of machine/converter asymmetry (as needed for Chapters 3 and 4), external resistors are added between the six-phase machine and the machine-side VSCs, as shown in the figure.

This appendix describes how the simulation model is built. It should be noted here that the simulation model has been constructed using basic Simulink blocks, without resorting to the SimPowerSystems library. This is mainly due to the fact that the core component of the simulation model, i.e. the six-phase machine, is not directly available in the SimPowerSystems library and has to be constructed using basic Simulink blocks. Since SimPowerSystems software is not used, special care is required in developing certain parts of the simulation model, such as during implementation of the dc-power supply as a constant voltage source, implementation of the external resistors for emulating the machine/converter asymmetry, and the leg-to-phase voltage transformation when interfacing the VSC with the machine. All these aspects are discussed in what follows.

The blocks in the simulation model can be divided into two parts, i.e. the physical components and the control components. The former consists of all physical apparatus of the system, such as the induction machine, VSC, dc-link, and so on, and will be addressed in Section A.2. Section A.3, on the other hand, covers all the components which are related to the implementation of the control algorithms.

A.2. Modelling of the Physical Blocks

A.2.1. Asymmetrical Six-Phase Induction Machine

Consider an asymmetrical six-phase machine with two sets of isolated three-phase windings, so that zero-sequence components can be neglected. Motoring positive stator current sign convention has been adopted throughout, by taking current flowing

from the converter to the machine as the positive current. Using the VSD method, the machine equations in the stationary reference frame are given with:

$$\begin{aligned}
v_{\alpha s} &= R_s i_{\alpha s} + d\psi_{\alpha s} / dt \\
v_{\beta s} &= R_s i_{\beta s} + d\psi_{\beta s} / dt \\
0 &= R_r i_{\alpha r} + d\psi_{\alpha r} / dt + \omega_r \psi_{\beta r} \\
0 &= R_r i_{\beta r} + d\psi_{\beta r} / dt - \omega_r \psi_{\alpha r}
\end{aligned} \tag{A.1}$$

$$\begin{aligned}
\psi_{\alpha s} &= (L_{ls} + L_m) i_{\alpha s} + L_m i_{\alpha r} \\
\psi_{\beta s} &= (L_{ls} + L_m) i_{\beta s} + L_m i_{\beta r} \\
\psi_{\alpha r} &= (L_{lr} + L_m) i_{\alpha r} + L_m i_{\alpha s} \\
\psi_{\beta r} &= (L_{lr} + L_m) i_{\beta r} + L_m i_{\beta s}
\end{aligned} \tag{A.2}$$

$$T_e = pL_m [i_{\alpha r} i_{\beta s} - i_{\alpha s} i_{\beta r}] \tag{A.3}$$

The x - y components are only relevant for the stator quantities, since rotor is short-circuited. Hence, the stator x - y plane is described with

$$\begin{aligned}
v_{xs} &= R_s i_{xs} + d\psi_{xs} / dt \\
v_{ys} &= R_s i_{ys} + d\psi_{ys} / dt
\end{aligned} \tag{A.4}$$

$$\begin{aligned}
\psi_{xs} &= L_{ls} i_{xs} \\
\psi_{ys} &= L_{ls} i_{ys}
\end{aligned} \tag{A.5}$$

Rotor motion is governed with

$$T_e - T_m = (J / p) \frac{d\omega_r}{dt} \tag{A.6}$$

$$T_e - T_m = J \frac{d\omega_m}{dt} \tag{A.7}$$

For the simulation, the six-phase machine is modelled in the α - β (stationary) common reference frame using equations (A.1) to (A.7). This gives a simpler model structure compared with the model in the d - q reference frame. The final form of the six-phase machine block in Matlab/Simulink is shown in Fig. A.2. Since the equations are expressed in the form of decoupled variables, decoupling transformation $[T]$ is required to transform the phase voltage inputs (denoted as “Vs” in Fig. A.1) to the corresponding axis components. Similarly, inverse decoupling transformations (denoted as “inverse

[T]” in Fig. A.1) are applied to the stator and rotor currents to yield the actual phase components. Note that the “Stator Block”, “Rotor Block” and “Mechanical Block” are in essence equations (A.1) to (A.7), which are therefore not shown in detail.

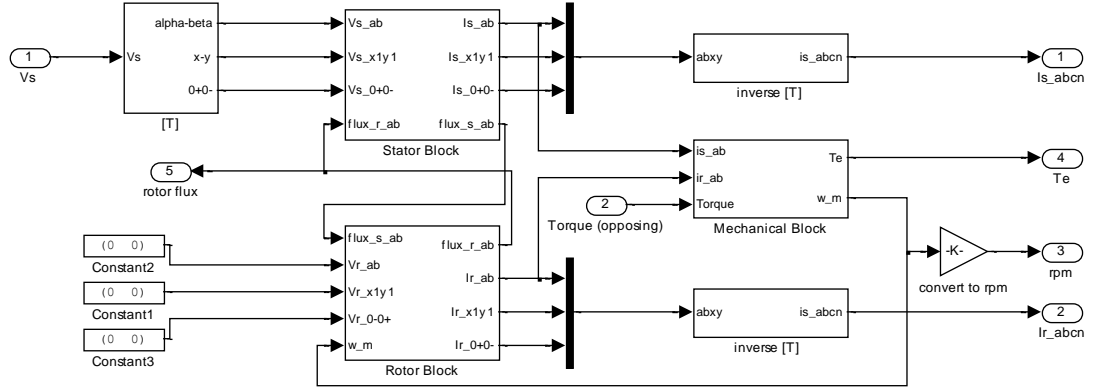


Fig. A.2. Asymmetrical six-phase induction machine model.

A.2.2. Two-level Three-phase VSC

In this thesis, the six-phase induction machine is controlled using two units of two-level three-phase VSCs. In the simulation, each three-phase VSC is modelled as a modular block, so that both parallel- and series-connection topologies can be simulated.

Consider a two-level three-phase VSC connected to a dc-link, as shown in Fig. A.3. A switching state of a VSC can be expressed as $(S_a S_b S_c)$ with the switching state of phase- j defined as:

$$S_j = \begin{cases} 1 & \text{when upperswitch is on} \\ 0 & \text{when lower switch is on} \end{cases} \quad (\text{A.8})$$

Using (A.8), the output leg voltage, with respect of the dc-link mid-point O , is given as:

$$V_{jo} = \begin{cases} \frac{1}{2}V_{dc} & \text{if } S_j = 1 \\ -\frac{1}{2}V_{dc} & \text{if } S_j = 0 \end{cases} \quad (\text{A.9})$$

In the simulation model, this is implemented by using a “Switch” block, to convert the switching signals into the corresponding leg voltages. However, since the machine equations are related to phase voltages rather than leg voltages, the leg voltages have to be transformed into the equivalent phase voltages, using the following equation:

$$\begin{aligned}
 v_{as} &= \frac{1}{3}(2v_{ao} - v_{bo} - v_{co}) \\
 v_{bs} &= \frac{1}{3}(2v_{bo} - v_{ao} - v_{co}) \\
 v_{cs} &= \frac{1}{3}(2v_{co} - v_{ao} - v_{bo})
 \end{aligned} \tag{A.10}$$

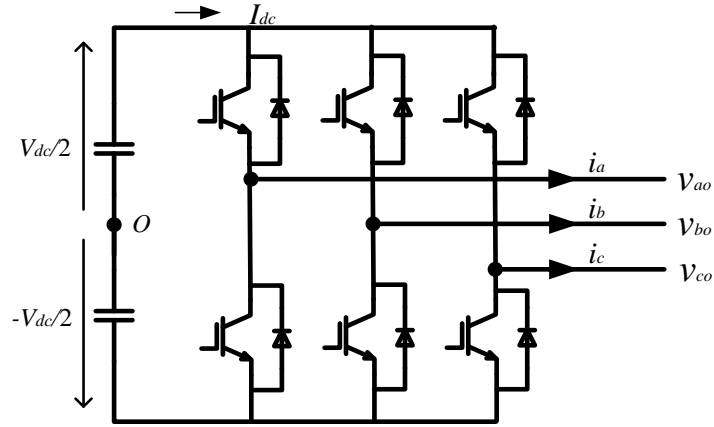


Fig. A.3. Two-level three-phase voltage source converter.

In addition to the phase voltages, dc-link current of the VSC needs to be determined as well. This current is important in calculating the dc-link voltage, as will be discussed in the later part of this appendix. The converter's dc-link current (flowing from the dc-link to the converter) can be expressed as:

$$I_{dc} = S_a i_a + S_b i_b + S_c i_c \tag{A.11}$$

where $i_{a,b,c}$ stand for the converter's phase currents. It should be noted that, although dc-link voltage is here a time-varying quantity, it is denoted with a capital symbol, in line with the notation used in inverter-fed variable-speed drives.

The actual implementation of the VSC in Matlab/Simulink is shown in Fig. A.4. All the blocks shown in the figure can be easily related to equations (A.9) to (A.11), except the "External resistors" and "Dead time" blocks, which will be addressed shortly.

A.2.3. External Resistors

In order to study the effect of machine/converter asymmetry (as needed for Chapter 3 and Chapter 4), additional resistors are added between the VSCs and the six-phase machine to deliberately introduce an unbalanced condition. This effect needs to be included in the simulation model as well.

Intuitively, the external resistors can be emulated by setting the stator resistance of each phase to a different value. However, since the machine model is constructed based on equations in the form of decoupled variables, this cannot be done easily. Hence, an alternative approach is adopted. It is expected that the presence of the external resistance ($R_{external}$) causes additional voltage drop ($v_{drop} = R_{external}i$) between the VSC's output and the machine's terminals. By calculating and then subtracting this voltage drop from the VSC leg voltage, the presence of the external resistors can thus be simulated. This is shown in Fig. A.4, where the "External resistors" block is used to calculate and subtract the voltage drops from the VSC leg voltages, before applying the leg-to-phase voltage transformation. Detailed implementation of the "External resistors" block is shown in Fig. A.5. These values are exactly the same as those external resistors physically added in the experiments in Chapter 3 and 4.

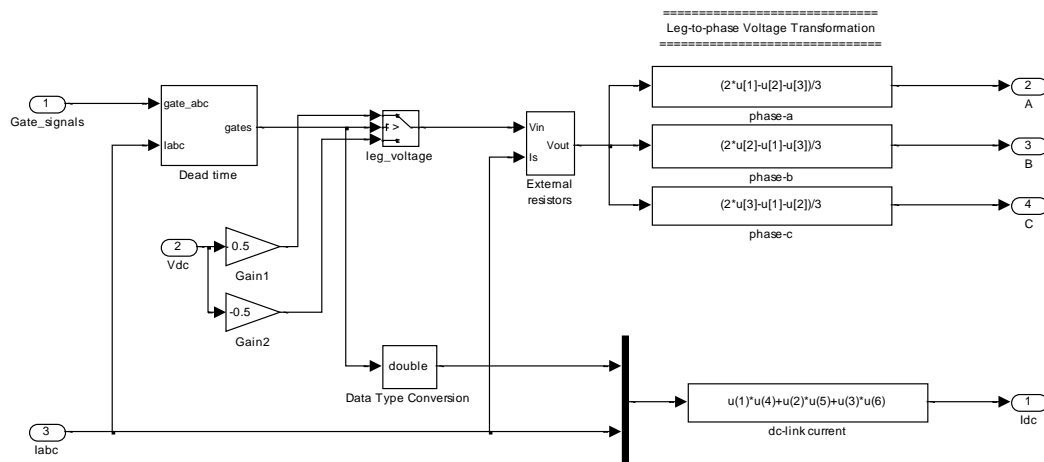


Fig. A.4. Actual implementation of the two-level three-phase VSC in Matlab/Simulink.

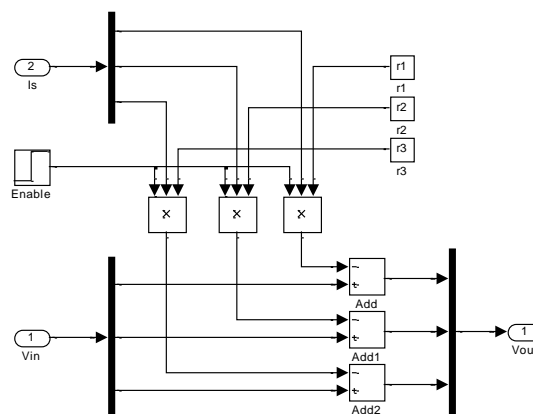


Fig. A.5. Detailed implementation of the "External Resistors" block.

A.2.4. Dead Time

The compensation of dead-time effect in an inverter fed asymmetrical six-phase machine is part of the core considerations in Chapter 3. In order to allow study of the dead-time effect within the simulation model, dead time has to be included.

To start with, dead time is introduced by delaying the turn-on time of the switches so that there exists a period of time when both the upper and lower switches are turned off. The main problem with the dead time is that during this period of time, the leg voltage of the VSC is no longer determined by the switching signal, but instead, decided by the polarity of the phase current. When the phase current is positive, the freewheeling diode of the lower switch will be forward-biased, and the leg voltage is equal to $-\frac{1}{2}V_{dc}$. Alternatively, when the phase current is negative, the upper switch's freewheeling diode will be forward-biased, giving a leg voltage of $\frac{1}{2}V_{dc}$. This dependency of the leg voltage on the current polarity needs to be included in the simulation, in order to emulate the dead-time effect.

Implementation of the dead-time effect is shown in Fig. A.6. First, the dead time is inserted into the gate signals via the block “dead-time insert”. Details of this block are shown in Fig. A.7; the duration of the dead time is specified in the “Transport delay” block. It should be noted that this is not the only way of inserting dead time into the gate signals, and any other feasible approach can be utilised instead of this block. The output of this block is an intermediate switching state, denoted as S_j' , where

$$S_j' = \begin{cases} 2 & \text{when upper switch is on} \\ 1 & \text{when lower switch is on} \\ 0 & \text{when both switches are off} \end{cases} \quad (\text{A.12})$$

Compared to equation (A.8), an additional state has been introduced to represent the dead time. This intermediate switching state needs to be converted back to the regular switching state in (A.8) using the following logic: intermediate switching states

of $S_j' = 1$ and $S_j' = 2$ are equivalent to switching states $S_j = 0$ and $S_j = 1$, respectively. During dead time, i.e. when $S_j' = 2$, the phase current's polarity needs to be checked to determine the equivalent switching state. If the current is positive, the equivalent switching state is $S_j = 0$, otherwise the equivalent switching state is $S_j = 1$. With that, the VSC leg voltage during dead time can be determined correctly, and effect of dead time will appear in the simulation.

Although, ideally, the polarity of the current should be checked by comparing the current with zero, such approach causes strong chattering and significantly slows down the simulation. Thus, instead of a “Compare to zero” block, a “Relay” block with hysteresis band of 0.001 A is utilised to improve the simulation speed.

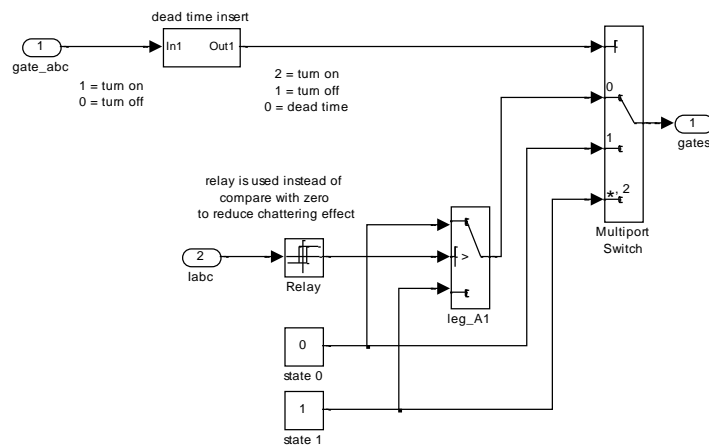


Fig. A.6. Actual implementation of the dead-time effect in Matlab/Simulink.

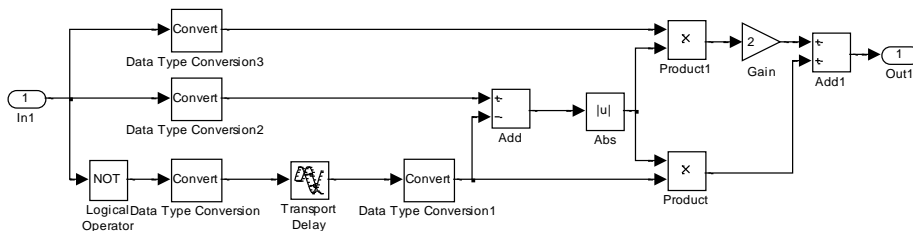


Fig. A.7. Detailed implementation of the “dead-time insert” block.

A.2.5. DC-link

In practice, the dc-link voltage of the VSC is determined by the charging and discharging of the dc-link capacitor. This phenomenon needs to be modelled in the simulation as well, in order to study the dc-link voltage balancing issue in Chapter 4.

In the simulation model, the dc-link in VSC is modelled as an ideal capacitor without including the effect of parasitic resistance and inductance. For the purpose of deriving the dc-link current equation, positive dc-link currents are by default defined as currents flowing away from the dc-link capacitor, as illustrated in Fig. A.8. It should be noted that the current I_1 is the VSC's dc-link current given in (A.11). The governing equation for the capacitor voltage is:

$$C \frac{d}{dt} V_{dc} = I_{cap} = -I_1 - I_2 \quad (\text{A.13})$$

Hence, dc-link voltage is modelled using

$$V_{dc} = \frac{1}{C} \int (-I_1 - I_2) dt \quad (\text{A.14})$$

As mentioned earlier, the VSCs in the simulation model are modelled as modular blocks to allow simulations of both parallel- and series-connected topologies. The main difference between the two topologies lies in the way the dc-link currents are defined, as can be seen in Fig. A.9.

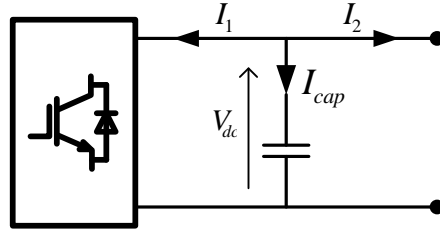


Fig. A.8. Dc-link of a VSC modelled as an ideal capacitor.

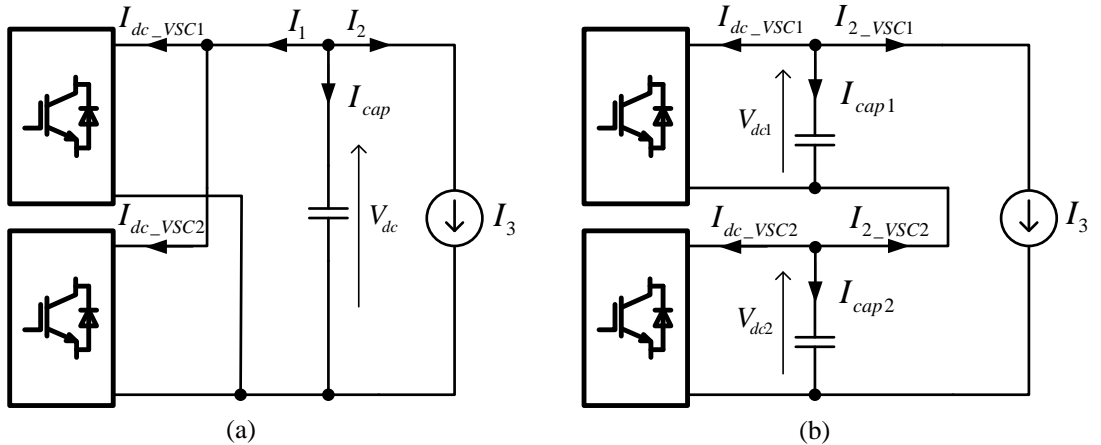


Fig. A.9. Dc-link for topologies with (a) parallel- and (b) series-connected VSCs.

For the case with the two VSCs connected in parallel (Fig. A.9 (a)), only one dc-link exists. From the figure, it can be observed that I_1 is the sum of the dc-link currents from VSC1 and VSC2, while I_2 is equal to the load (or supply) current I_3 , i.e.:

$$\begin{aligned} I_1 &= I_{dc_VSC1} + I_{dc_VSC2} \\ I_2 &= I_3 \end{aligned} \quad (\text{A.15})$$

Hence, the dc-link voltage is calculated as

$$V_{dc} = \frac{1}{C} \int (-I_{dc_VSC1} - I_{dc_VSC2} - I_3) dt \quad (\text{A.16})$$

For the series-connection (Fig. A.9 (b)), two dc-links need to be simulated. Based on the currents indicated in the figure, it is clear that the dc-link voltages for the series-connected topology are given as:

$$\begin{aligned} V_{dc1} &= \frac{1}{C_1} \int (-I_{dc_VSC1} - I_3) dt \\ V_{dc2} &= \frac{1}{C_2} \int (-I_{dc_VSC2} - I_3) dt \end{aligned} \quad (\text{A.17})$$

Based on (A.16) and (A.17), the dc-links for topologies with parallel- and series-connected VSCs can be simulated. Example of the actual implementation of the dc-link in Matlab/Simulink for the case of series-connected VSCs is shown in Fig. A.10.

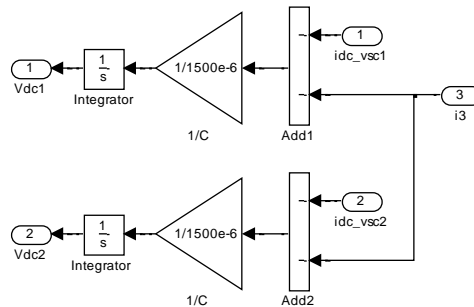


Fig. A.10. Actual implementation of the dc-link (series-connection) in Matlab/Simulink.

A.2.6. Dc-power Supply

From equations (A.16) and (A.17), it is clear that the calculation of dc-link voltage(s) requires the knowledge of the current I_3 . In practice, this is the current

provided by the dc-power supply (as seen in Fig. A.1) in order to maintain a constant dc-link voltage.

To emulate this current from the dc-power supply, a PI controller is utilised in the simulation model, as shown in left portion of Fig. A.11. The PI controller is used to derive current I_3 based on the error between the measured dc-link voltage and the reference dc-link voltage. The current I_3 is then used (by the “dc-link” block shown in right portion of Fig. A.11) to calculate the dc-link voltages, based on (A.16) and (A.17), as discussed in the previous subsection. For the simulation, the PI gains are tuned via trial and error to obtain a sufficiently fast regulation of the dc-link voltage and a realistic emulation of the dc-power supply.

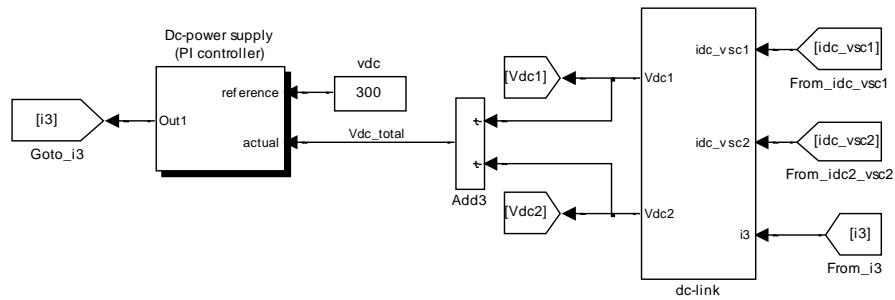


Fig. A.11. Actual implementation of the dc power supply using a PI controller in Matlab/Simulink, for the case with series-connected VSCs.

A.3. Modelling of the Control Blocks

A.3.1. Indirect Rotor Flux Oriented Control

For the control of the six-phase squirrel cage induction machine, indirect rotor flux oriented principle is used. The structure of the control is shown in Fig. A.12. Since the details of the x - y current controllers have been addressed in Chapter 3, they are not repeated here. Only the d - q current controllers and the speed controller are shown in this case.

The feed-forward terms e_d and e_q are used to improve the decoupling of d - q current control, and are given by:

$$e_d = -\omega_s L_s \left(1 - \frac{L_m^2}{L_s L_r} \right) i_{qs}^* \quad (\text{A.18})$$

$$e_q = \omega_s L_s i_{ds}^* \quad (\text{A.19})$$

where reference frame's angular frequency, ω_s , equals the rotor flux's angular frequency,

$$\omega_s = \omega_r + \omega_{sl} \quad (\text{A.20})$$

The slip frequency is estimated using

$$\omega_{sl}^* = \frac{1}{\tau_r} \frac{i_{qs}^*}{i_{ds}^*} \quad (\text{A.21})$$

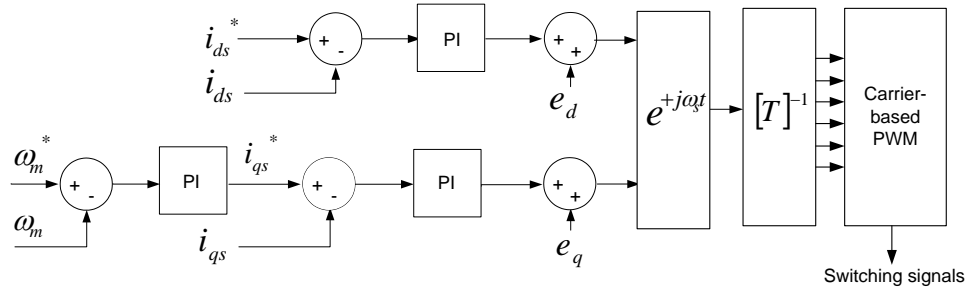


Fig. A.12. Indirect rotor flux oriented control structure including d - q current control.

A.3.2. Carrier-based Pulse Width Modulation

In this thesis, carrier-based pulse with modulation is used to modulate the phase voltage references. To improve dc-link voltage utilisation, double zero-sequence injection method has been used (Bojoi *et al.*, 2002). Based on this method, the two three-phase windings are treated separately. For each three-phase converter, the zero-sequence voltage to be injected is obtained using the conventional min-max method for three-phase systems:

$$v_{zero} = -0.5(\max[v_{an}, v_{bn}, v_{cn}] + \min[v_{an}, v_{bn}, v_{cn}]) \quad (\text{A.22})$$

The resultant modulating signal is obtained by adding v_{zero} to the reference phase voltages, and dividing with V_{dc} . An offset of 0.5 is added before the modulating signal is compared with a triangular carrier of frequency f_c and unity amplitude:

$$\text{modulating signal} = \frac{(v_{phase}^* + v_{zero})}{V_{dc}} + 0.5 \quad (\text{A.23})$$

For two-level VSC, a triangular wave with unity peak-to-peak magnitude is used as the carrier signal. Whenever the modulating signal is higher than the carrier, upper switch of the phase leg will be turned on ($S_j = 1$), while the lower switch in the corresponding phase leg is turned on when the modulating signal is below the carrier ($S_j = 0$). Actual implementation of the pulse-width modulation is shown in Fig. A.12. Note that “Zero-Order Hold” blocks have been inserted before the modulating signals are compared with the carrier signal. This is to provide a closer approximation to the experimental results implemented using digital control, and to reduce numerical errors in the simulation.

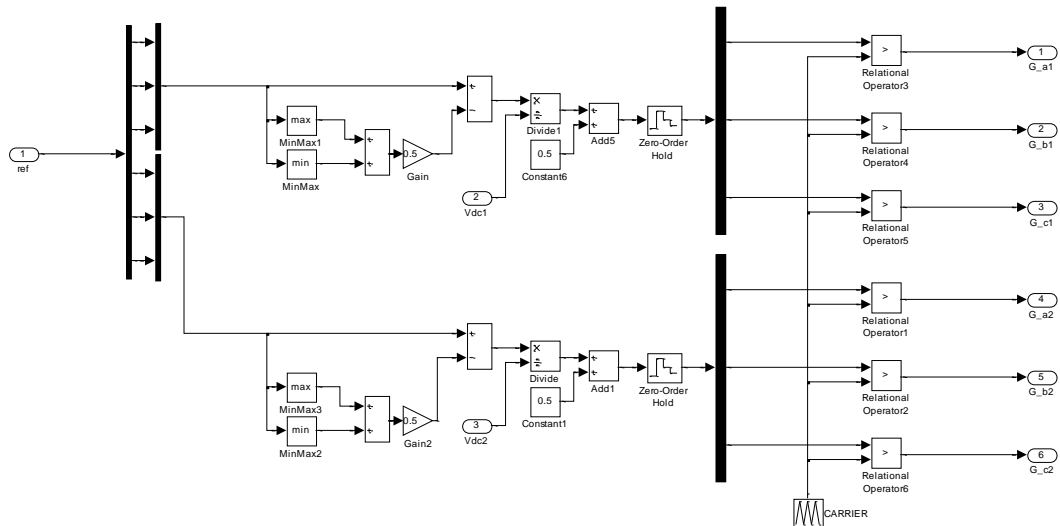


Fig. A.13. Actual implementation of the carrier-based PWM (with double zero-sequence injection) in Matlab/Simulink.

A.4. Summary

This appendix has provided a detail account of the simulation model used for investigating the control of the asymmetrical six-phase induction machine. Even though the model is more complicated than the case would have been had the SimPowerSystems library been used, it gives a better understanding of the operation of each component in the model. The simulation results presented in this thesis as well as

in the conference/journal papers published from the thesis, were obtained using this simulation model. As can be observed by comparing the simulation and experimental results, the simulation model is capable of emulating the actual system with high accuracy.

Appendix B

EXPERIMENTAL SETUP

B.1. Overview

In this research work, both simulation and experimental tests are used to validate the theoretical analysis and to confirm the feasibility of the studied control methods. While the development of the simulation model has been detailed in Appendix A, this appendix provides information on the experimental setup used in this research work.

The overview of the experimental setup is shown in Fig. B.1. Similar as in Fig. A.1., the system consists of an asymmetrical six-phase induction machine fed by machine-side VSCs, with dc-link voltage provided by a dc-power supply. A dc machine, controlled by a commercial dc drive, is coupled to the six-phase machine and acts as mechanical load. Further explanations of the components in the experimental setup are addressed in subsequent parts of this appendix.

B.2. Electric Machines

B.2.1. Asymmetrical Six-phase Induction Machine

The core of this research project, i.e. the asymmetrical six-phase induction machine, is obtained by rewinding a 1.1 kW three-phase induction machine. The resultant machine is wound with three pole pairs, with rated phase voltage and current

of $110 \text{ V}_{\text{rms}}$ and $1.75 \text{ A}_{\text{rms}}$ respectively. The exact machine parameters are yet to be determined, but so far sufficiently good performance has been obtained in simulations and experiments by using the values shown in Table B.1. It has to be stressed here that the stator leakage inductance in the x - y plane is much smaller than the one in the d - q plane, which results in relatively high switching ripple in the phase currents.

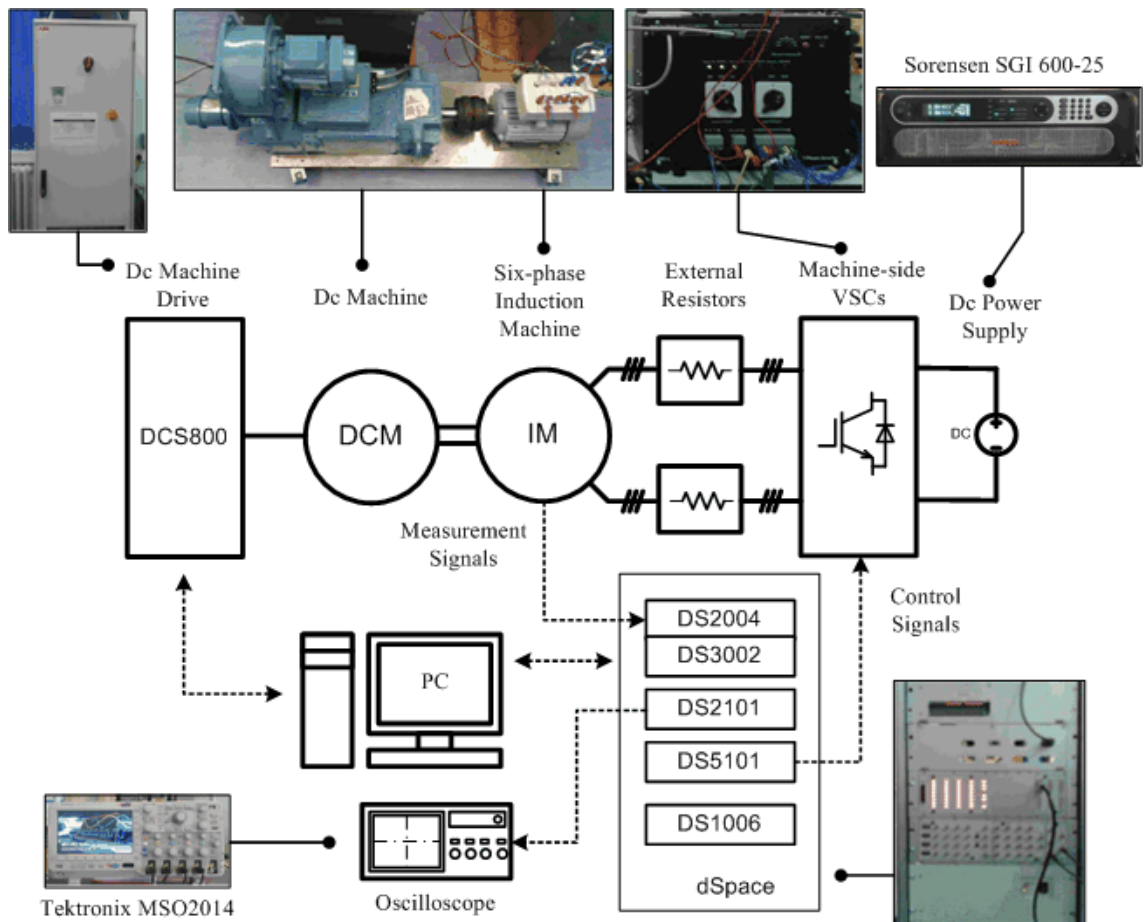


Fig. B.1. Overview of the experimental setup used.

Table B.1. Parameters for the asymmetrical six-phase induction machine.

<u>Stator Parameters</u>	
$R_s = 12.5 \Omega$	
$L_{ls_dq} = 0.0615 \text{ H}$	$L_{ls_xy} = 0.0055 \text{ H}$
$L_m = 0.590 \text{ H}$	
<u>Rotor Parameters</u>	
$R_r = 12.0 \Omega$	$L_{lr} = 0.011 \text{ H}$

B.2.2. Dc Machine

A 7.5 kW dc machine is mechanically coupled to the six-phase machine to provide load torque. Speed and torque control of the machine has been made possible

using the CodeSys program and DCS800 dc drive from ABB. The machine nameplate data are as listed in Table B.2.

Table B.2. Nameplate parameters for the dc machine.

Rated power	= 7.5 kW	Rated speed	= 1750rpm
Armature voltage	= 400V	Armature current	= 24A
Excitation voltage	= 360V	Excitation current	= 1.25A

B.3. Voltage Source Converter

In the experiments, the induction machine is driven by using two custom-built two-level eight-leg VSCs. The overall VSC assembly for the machine supply can operate by utilizing a single (in VSC parallel connection mode) or both VSCs (in series-connected case). These VSCs are referred to as VSC1 and VSC2, as shown in Fig. B.2. Although each VSC is designed with 8 legs, only 7 legs are operational by default (because the input for the 8th leg is used as ‘enable’ pin) and are designated as F1...F7 in what follows.

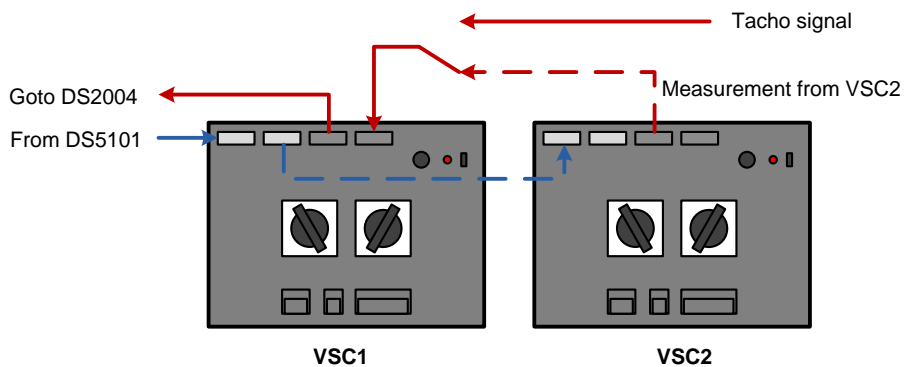


Fig B.2. Connections for single VSC or two VSCs mode.

Referring to Fig. B.2, the blue lines are the PWM signals provided by the dSpace DS5101 PWM module, while the red lines are the default current and dc-link voltage measurement signals from VSC to dSpace DS2004 ADC module. The dotted lines represent the connections that will only be present for two VSCs mode. Dead time of 6 μ s is inserted using onboard circuit embedded in the VSCs. Note that the speed measurement signal from a tacho uses the same connection port as the measurement signals from VSC2. Hence, speed measurement using tacho is only made possible in the

the single VSC mode. Table B.3 summarises the ADC channels and their corresponding signals according to the connections shown in Fig. B.2.

Fig. B.3 shows the respective connections for the case of a six-phase machine configured with two isolated neutrals. While the single VSC operation represents the typical connection, two VSCs mode allows investigation of series-connected VSC topology, such as for the case discussed in Chapter 4.

Table B.3. Measurement signals and corresponding ADC channels.

ADC Channel	Single VSC	Two VSCs
1	-	VSC2-F1 current
2	-	VSC2-F2 current
3	-	VSC2-F3 current
4	-	VSC2-F4 current
5	-	VSC2-F5 current
6	-	VSC2-F6 current
7	-	VSC2-F7 current
8	*Tacho Signal	VSC2-Vdc
9	VSC1-F1 current	
10	VSC1-F2 current	
11	VSC1-F3 current	
12	VSC1-F4 current	
13	VSC1-F5 current	
14	VSC1-F6 current	
15	VSC1-F7 current	
16	VSC1-Vdc	

* when operating with single VSC, channel 8 of the ADC is used to read the speed measurement signal from the tachogenerator.

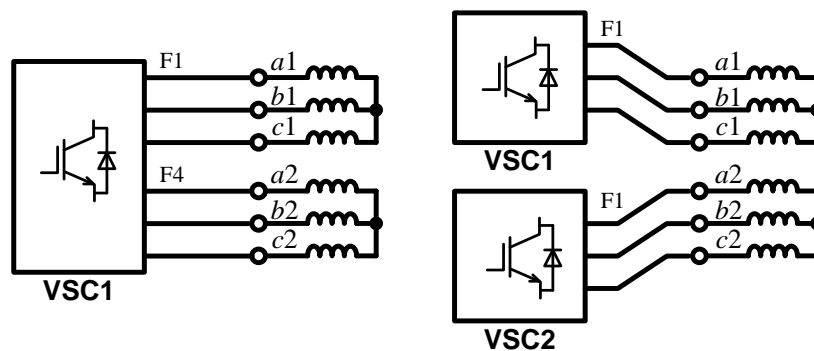


Fig. B.3. Connections between the converters and the six-phase machine for (left) single VSC and (right) two VSCs operation.

B.4. Speed Sensor

Although not explicitly shown in Fig. B.1, speed sensor is an important part of the experimental setup, as it provides the speed measurement needed for implementing closed-loop speed control and field orientation. There are two means of obtaining the

machine speed from in this experimental rig: (i) using a resolver (mounted on the six-phase machine) or (ii) using a tachogenerator (mounted on the dc-machine). Both signals require additional signal conditioning circuits before the signal can be fed to the dSpace.

For the resolver, a resolver-to-encoder converter (RDC) board is used to convert the resolver signal to encoder signal before feeding it to the DS3002 encoder board. Access to this speed measurement is done using DS3002 block in the dSpace program.

For the tacho, the output signal is in the range of ± 60 V for a speed ± 1000 rpm (note that the dc-machine can operate at higher speed, but this speed range is selected based on the rated speed of the six-phase machine). A simple voltage divider circuit is used to scale the voltage down by a factor of 6, to ± 10 V, to be compatible with the DS2004 ADC input range. This speed measurement can be accessed from the dSpace program via channel 8 of the ADC block.

It is suspected that the resolver mounting is not perfect, since a significant speed variation (of the order of ± 5 rpm) was observed in the speed measurement. The tacho measurement gives generally better accuracy of speed measurement, with speed variation of approximately ± 1 rpm. Nevertheless, since tacho could not be used during two VSCs mode, the resolver had to be used in that case. The program for dSpace is hence configured with the possibility of using any of the two speed measurements.

B.5. dSpace System

All control algorithms, presented in Chapter 3 to 5, are implemented using a dSpace system, and control uses the Control Desk software. For this experimental setup, high performance DS1006 processor board is used as the core of the dSpace system. However, DS1006 only provides the computational power for the system, so several other auxiliary modules are required to perform the required control.

Four dSpace modules, designated for different purposes, are used. The modules and their corresponding features are as follow:

- 1) DS5101 Multi-PWM – Digital Waveform Output Board
 - Used to generate up to 16 channels of PWM signals.
 - Time resolution of 25 ns.
 - One limitation of this module is that the output has a minimum pulse length of 800 ns and 250 ns for HIGH (output = 1) and LOW (output = 0), respectively. Hence, the output will not be kept at constant high (100% duty cycle) or constant low (0% duty cycle).
- 2) DS2004 ADC – High-Speed A/D Board
 - Used to provide analogue to digital conversion.
 - 16 channels.
 - 16-bit resolution with maximum conversion time of 800 ns.
- 3) DS3002 Encoder – Incremental Encoder Board
 - Used to read the speed and position information from the incremental encoder.
 - 6 channels, which support encoder with analogue or digital output signal.
 - 32 bits position counters for fourfold line count.
 - 2x12 bit, 10MPS ADC for evaluation of analogue signals.
- 4) DS2101 DAC – D/A Board
 - Used to display selected variables on the oscilloscope.
 - 5 channels with 12-bits resolution.
 - Selectable output range ($\pm 5V$, $\pm 10V$ or $0\sim 10V$).

B.6. Software

B.6.1. Matlab/Simulink and Control Desk for dSpace

The use of dSpace allows easy implementation of a control algorithm via Matlab/Simulink, so that programming in C/C++ language is not required. This significantly reduces the development time of the algorithms. A snapshot of the program implemented in the Matlab/Simulink environment is shown in Fig. B.4. After

compiling and downloading the program into dSpace, control and monitoring can be done using user-defined graphical user interface (GUI) developed in the Control Desk software environment. Snapshot of the GUI developed for control of the six-phase machine for this project is shown in Fig. B.5.

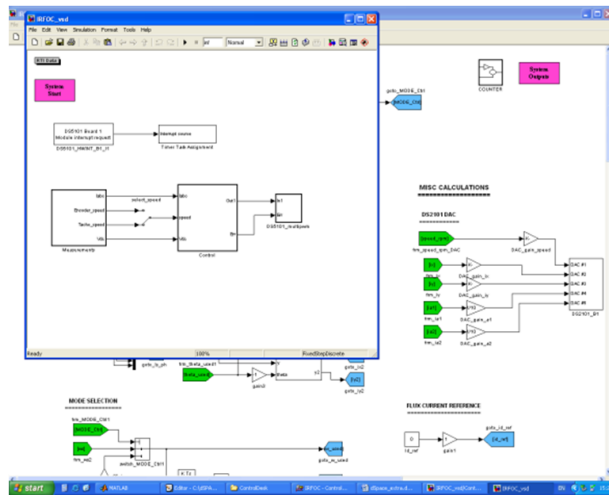


Fig. B.4. Snapshot of dSpace program implemented in the Matlab/Simulink environment.

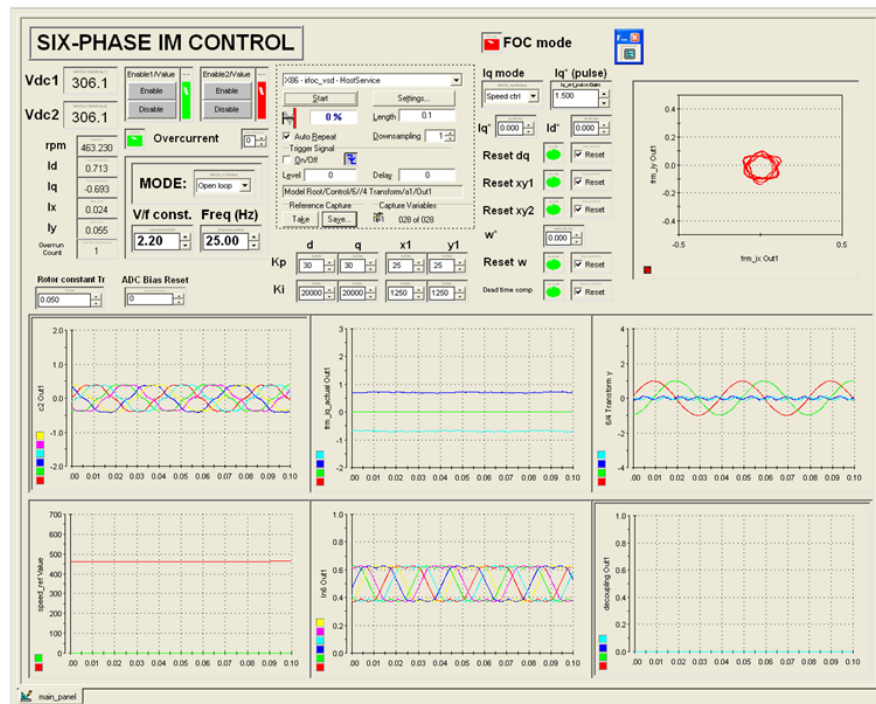


Fig. B.5. Snapshot of GUI developed in Control Desk software environment.

B.6.2. CoDeSys for DCS800

In addition to the six-phase machine, the dc machine has to be controlled as well to provide desired loading to the machine. Although the commercial dc drive DCS800 allows speed control to be done via Drive Window Light software, the control options

provided are limited. Torque control of the machine, which is required for the experiments, is not possible using default features in Drive Window Light. Hence, a user-defined open-loop torque control program has been written for DCS800 using CoDeSys software. The program allows user to operate the machine in either speed or torque control mode, in an open loop manner. The GUI for the control of dc machine is shown in Fig. B.6.

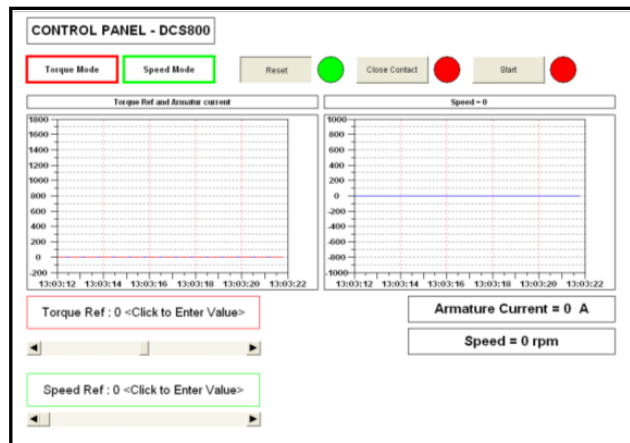


Fig. B.6. Snapshot of GUI developed in CoDeSys software environment.

B.7. Summary

This appendix gives an overview of the experimental setup used in this research project. All the core components of the setup, including hardware and software, have been discussed. It is hoped that, with the information provided in this appendix, a reader can get a clearer idea regarding the implementation of the studied control schemes in this thesis, as well as of the manner in which the experimental results presented in the thesis have been obtained.

Appendix C

DERIVATION OF MACHINE EQUATIONS FOR THE FAULTED MACHINE

C.1. Introduction

This appendix contains derivations of the machine equations for the case when an asymmetrical six-phase induction machine is exposed to an open-circuit fault. In Section C.2, it is first shown that each phase of the machine can be represented as a Thevenin equivalent circuit, consisting of an RL part and a back EMF part. Subsequently, in Section C.3, it is shown that the back EMFs sum to zero during an open-circuit fault, regardless of the type of neutral point configuration (single or two isolated ones) of the stator winding. The results of this appendix are used in the analysis presented in Section 5.4.1.2 of Chapter 5.

C.2. Equations for a Healthy Machine

The machine equations, in terms of phase variables, for a healthy asymmetrical six-phase induction machine are given with

$$\begin{aligned} [v_{ks}] &= [R_s] \cdot [i_{ks}] + \frac{d}{dt} [\psi_{ks}] \\ [v_{kr}] &= [R_r] \cdot [i_{kr}] + \frac{d}{dt} [\psi_{kr}] \end{aligned} \tag{C.1}$$

$$\begin{aligned} [\psi_{ks}] &= [L_{ss}] \cdot [i_{ks}] + [L_{sr}] \cdot [i_{kr}] \\ [\psi_{kr}] &= [L_{rr}] \cdot [i_{kr}] + [L_{rs}] \cdot [i_{ks}] \end{aligned} \quad (C.2)$$

where $[I_6]$ is the 6×6 identity matrix, and

$$\begin{aligned} [v_{ks}] &= [v_{a1s} \ v_{b1s} \ v_{c1s} \ v_{a2s} \ v_{b2s} \ v_{c2s}]^T \\ [v_{kr}] &= [0 \ 0 \ 0 \ 0 \ 0 \ 0]^T \\ [i_{ks}] &= [i_{a1s} \ i_{b1s} \ i_{c1s} \ i_{a2s} \ i_{b2s} \ i_{c2s}]^T \\ [i_{kr}] &= [i_{a1r} \ i_{b1r} \ i_{c1r} \ i_{a2r} \ i_{b2r} \ i_{c2r}]^T \end{aligned} \quad (C.3)$$

$$[L_{ss}] = L_{ls} \cdot [I_6] + [L_{ms}] = L_{ls} \cdot [I_6] + M \cdot \begin{bmatrix} 1 & -\frac{1}{2} & -\frac{1}{2} & \frac{\sqrt{3}}{2} & -\frac{\sqrt{3}}{2} & 0 \\ -\frac{1}{2} & 1 & -\frac{1}{2} & 0 & \frac{\sqrt{3}}{2} & -\frac{\sqrt{3}}{2} \\ -\frac{1}{2} & -\frac{1}{2} & 1 & -\frac{\sqrt{3}}{2} & 0 & \frac{\sqrt{3}}{2} \\ \frac{\sqrt{3}}{2} & 0 & -\frac{\sqrt{3}}{2} & 1 & -\frac{1}{2} & -\frac{1}{2} \\ -\frac{\sqrt{3}}{2} & \frac{\sqrt{3}}{2} & 0 & -\frac{1}{2} & 1 & -\frac{1}{2} \\ 0 & -\frac{\sqrt{3}}{2} & \frac{\sqrt{3}}{2} & -\frac{1}{2} & -\frac{1}{2} & 1 \end{bmatrix} \quad (C.4)$$

$$[L_{rr}] = L_{lr} \cdot [I_6] + [L_{ms}] = L_{lr} \cdot [I_6] + M \cdot \begin{bmatrix} 1 & -\frac{1}{2} & -\frac{1}{2} & \frac{\sqrt{3}}{2} & -\frac{\sqrt{3}}{2} & 0 \\ -\frac{1}{2} & 1 & -\frac{1}{2} & 0 & \frac{\sqrt{3}}{2} & -\frac{\sqrt{3}}{2} \\ -\frac{1}{2} & -\frac{1}{2} & 1 & -\frac{\sqrt{3}}{2} & 0 & \frac{\sqrt{3}}{2} \\ \frac{\sqrt{3}}{2} & 0 & -\frac{\sqrt{3}}{2} & 1 & -\frac{1}{2} & -\frac{1}{2} \\ -\frac{\sqrt{3}}{2} & \frac{\sqrt{3}}{2} & 0 & -\frac{1}{2} & 1 & -\frac{1}{2} \\ 0 & -\frac{\sqrt{3}}{2} & \frac{\sqrt{3}}{2} & -\frac{1}{2} & -\frac{1}{2} & 1 \end{bmatrix} \quad (C.5)$$

$$[L_{sr}] = M \cdot \begin{bmatrix} \cos \theta_r & \cos(\theta_r + \frac{2\pi}{3}) & \cos(\theta_r + \frac{4\pi}{3}) & \cos(\theta_r + \frac{\pi}{6}) & \cos(\theta_r + \frac{5\pi}{6}) & \cos(\theta_r - \frac{\pi}{2}) \\ \cos(\theta_r + \frac{4\pi}{3}) & \cos \theta_r & \cos(\theta_r + \frac{2\pi}{3}) & \cos(\theta_r - \frac{\pi}{2}) & \cos(\theta_r + \frac{\pi}{6}) & \cos(\theta_r + \frac{5\pi}{6}) \\ \cos(\theta_r + \frac{2\pi}{3}) & \cos(\theta_r + \frac{4\pi}{3}) & \cos \theta_r & \cos(\theta_r + \frac{5\pi}{6}) & \cos(\theta_r - \frac{\pi}{2}) & \cos(\theta_r + \frac{\pi}{6}) \\ \cos(\theta_r + \frac{11\pi}{6}) & \cos(\theta_r + \frac{\pi}{2}) & \cos(\theta_r + \frac{7\pi}{2}) & \cos \theta_r & \cos(\theta_r + \frac{2\pi}{3}) & \cos(\theta_r + \frac{4\pi}{3}) \\ \cos(\theta_r + \frac{7\pi}{2}) & \cos(\theta_r + \frac{11\pi}{6}) & \cos(\theta_r + \frac{\pi}{2}) & \cos(\theta_r + \frac{4\pi}{3}) & \cos \theta_r & \cos(\theta_r + \frac{2\pi}{3}) \\ \cos(\theta_r + \frac{\pi}{2}) & \cos(\theta_r + \frac{7\pi}{2}) & \cos(\theta_r + \frac{11\pi}{6}) & \cos(\theta_r + \frac{2\pi}{3}) & \cos(\theta_r + \frac{4\pi}{3}) & \cos \theta_r \end{bmatrix} \quad (C.6)$$

$$[L_{rs}] = [L_{sr}]^T \quad (C.7)$$

The stator voltage equations can be expressed in the form of a Thevenin equivalent circuit consisting of an RL part and a back EMF part, as follows:

$$\begin{bmatrix} v_{a1s} \\ v_{b1s} \\ v_{c1s} \\ v_{a2s} \\ v_{b2s} \\ v_{c2s} \end{bmatrix} = \underbrace{\left(R_s [I_6] + L_{ls} [I_6] \cdot \frac{d}{dt} \right)}_{RL} \begin{bmatrix} i_{a1s} \\ i_{b1s} \\ i_{c1s} \\ i_{a2s} \\ i_{b2s} \\ i_{c2s} \end{bmatrix} + \underbrace{\left[L_{ms} \right] \cdot \frac{d}{dt}}_{\text{Back EMF}} \begin{bmatrix} i_{a1s} \\ i_{b1s} \\ i_{c1s} \\ i_{a2s} \\ i_{b2s} \\ i_{c2s} \end{bmatrix} + \frac{d}{dt} [L_{sr}] \cdot \begin{bmatrix} i_{a1r} \\ i_{b1r} \\ i_{c1r} \\ i_{a2r} \\ i_{b2r} \\ i_{c2r} \end{bmatrix} \quad (\text{C.8})$$

From the equation, it is evident that the back EMF expression contains two parts: the first one is related to the time derivatives of the stator currents (E_{ks}'), while the second one is related to the time derivatives of the rotor currents (E_{ks}''):

$$\begin{aligned} [E_{ks}] &= [L_{ms}] \cdot \frac{d}{dt} [i_{ks}] + \frac{d}{dt} [L_{sr}] \cdot [i_{kr}] \\ &= [E_{ks}'] + [E_{ks}''] \end{aligned} \quad (\text{C.9})$$

A graphical representation of the Thevenin's equivalent circuit is illustrated in Fig. C.1. It should be noted here that in order for the Thevenin representation of each phase (as shown in Fig. C.1) to be valid, the RL part of each phase should be associated to the corresponding phase current only. This is why the term $[L_{ms}] \cdot \frac{d}{dt} [i_{ks}]$, with each matrix element containing coupling effect of different phases, is not lumped together with $L_{ls} [I_6] \cdot \frac{d}{dt} [i_{ks}]$ in the RL part.

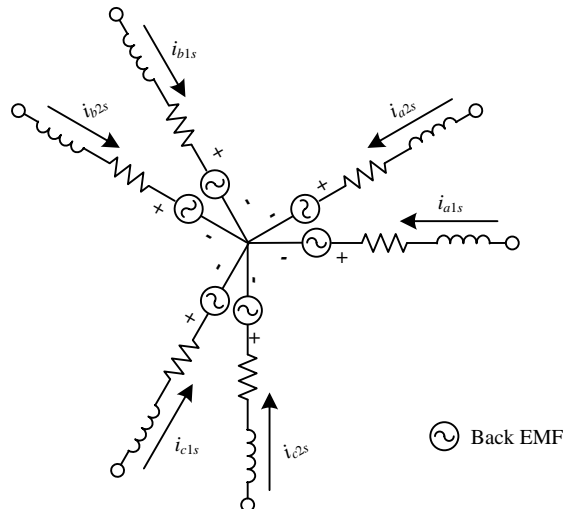


Fig. C.1. Thevenin equivalent circuit for an asymmetrical six-phase induction machine based on (C.8).

C.3. Back EMFs during Open-Circuit Fault

When phase- $c2$ of the machine is open-circuited due to a fault, the corresponding phase current becomes zero, $i_{c2s} = 0$. Substituting this constraint into the back EMF equation, the expression for E_{ks}' is given with

$$\begin{aligned}
 \begin{bmatrix} E_{a1s}' \\ E_{b1s}' \\ E_{c1s}' \\ E_{a2s}' \\ E_{b2s}' \\ E_{c2s}' \end{bmatrix} &= [L_{ms}] \cdot \frac{d}{dt} \begin{bmatrix} i_{a1s} \\ i_{b1s} \\ i_{c1s} \\ i_{a2s} \\ i_{b2s} \\ i_{c2s} \end{bmatrix} = L_{ms} \begin{bmatrix} 1 & -\frac{1}{2} & -\frac{1}{2} & \frac{\sqrt{3}}{2} & -\frac{\sqrt{3}}{2} & 0 \\ -\frac{1}{2} & 1 & -\frac{1}{2} & 0 & \frac{\sqrt{3}}{2} & -\frac{\sqrt{3}}{2} \\ -\frac{1}{2} & -\frac{1}{2} & 1 & -\frac{\sqrt{3}}{2} & 0 & \frac{\sqrt{3}}{2} \\ \frac{\sqrt{3}}{2} & 0 & -\frac{\sqrt{3}}{2} & 1 & -\frac{1}{2} & -\frac{1}{2} \\ -\frac{\sqrt{3}}{2} & \frac{\sqrt{3}}{2} & 0 & -\frac{1}{2} & 1 & -\frac{1}{2} \\ 0 & -\frac{\sqrt{3}}{2} & \frac{\sqrt{3}}{2} & -\frac{1}{2} & -\frac{1}{2} & 1 \end{bmatrix} \cdot \frac{d}{dt} \begin{bmatrix} i_{a1s} \\ i_{b1s} \\ i_{c1s} \\ i_{a2s} \\ i_{b2s} \\ 0 \end{bmatrix} \\
 &= L_{ms} \frac{d}{dt} \begin{bmatrix} i_{a1s} - \frac{1}{2}i_{b1s} - \frac{1}{2}i_{c1s} + \frac{\sqrt{3}}{2}i_{a2s} - \frac{\sqrt{3}}{2}i_{b2s} + 0 \\ -\frac{1}{2}i_{a1s} + i_{b1s} - \frac{1}{2}i_{c1s} + 0 + \frac{\sqrt{3}}{2}i_{b2s} + 0 \\ -\frac{1}{2}i_{a1s} - \frac{1}{2}i_{b1s} + i_{c1s} - \frac{\sqrt{3}}{2}i_{a2s} + 0 + 0 \\ \frac{\sqrt{3}}{2}i_{a1s} + 0 - \frac{\sqrt{3}}{2}i_{c1s} + i_{a2s} - \frac{1}{2}i_{b2s} + 0 \\ -\frac{\sqrt{3}}{2}i_{a1s} + \frac{\sqrt{3}}{2}i_{b1s} + 0 - \frac{1}{2}i_{a2s} + i_{b2s} + 0 \\ 0 - \frac{\sqrt{3}}{2}i_{b1s} + \frac{\sqrt{3}}{2}i_{c1s} - \frac{1}{2}i_{a2s} - \frac{1}{2}i_{b2s} + 0 \end{bmatrix}
 \end{aligned} \tag{C.10}$$

For the two isolated neutrals case, $i_{a1s} + i_{b1s} + i_{c1s} = 0$ and $i_{a2s} + i_{b2s} = 0$. Hence, the sums of the E_{ks}' for winding 1 and winding 2 are found both to be equal to zero:

$$\begin{aligned}
 E_{a1s}' + E_{b1s}' + E_{c1s}' &= L_{ms} \frac{d}{dt} \left[\begin{aligned} &\left(i_{a1s} - \frac{1}{2}i_{b1s} - \frac{1}{2}i_{c1s} + \frac{\sqrt{3}}{2}i_{a2s} - \frac{\sqrt{3}}{2}i_{b2s} + 0 \right) \\ &+ \left(-\frac{1}{2}i_{a1s} + i_{b1s} - \frac{1}{2}i_{c1s} + 0 + \frac{\sqrt{3}}{2}i_{b2s} + 0 \right) \\ &+ \left(-\frac{1}{2}i_{a1s} - \frac{1}{2}i_{b1s} + i_{c1s} - \frac{\sqrt{3}}{2}i_{a2s} + 0 + 0 \right) \end{aligned} \right] = 0 \\
 E_{a2s}' + E_{b2s}' + E_{c2s}' &= L_{ms} \frac{d}{dt} \left[\begin{aligned} &\left(\frac{\sqrt{3}}{2}i_{a1s} + 0 - \frac{\sqrt{3}}{2}i_{c1s} + i_{a2s} - \frac{1}{2}i_{b2s} + 0 \right) \\ &+ \left(-\frac{\sqrt{3}}{2}i_{a1s} + \frac{\sqrt{3}}{2}i_{b1s} + 0 - \frac{1}{2}i_{a2s} + i_{b2s} + 0 \right) \\ &+ \left(0 - \frac{\sqrt{3}}{2}i_{b1s} + \frac{\sqrt{3}}{2}i_{c1s} - \frac{1}{2}i_{a2s} - \frac{1}{2}i_{b2s} + 0 \right) \end{aligned} \right] = 0
 \end{aligned} \tag{C.11}$$

Based on the same principle, it is easy to see that the sum of the E_{ks}' for all six phases in the single isolated neutral case is zero as well:

$$E_{a1s}' + E_{b1s}' + E_{c1s}' + E_{a2s}' + E_{b2s}' + E_{c2s}' = 0 \tag{C.12}$$

On the other hand, the part of back EMF related to the time derivatives of rotor currents, E_{ks}'' , is given with the following expressions:

$$\begin{aligned}
 \begin{bmatrix} E_{a1s}'' \\ E_{b1s}'' \\ E_{c1s}'' \\ E_{a2s}'' \\ E_{b2s}'' \\ E_{c2s}'' \end{bmatrix} &= \frac{d}{dt} [L_{sr}] \cdot \begin{bmatrix} i_{a1r} \\ i_{b1r} \\ i_{c1r} \\ i_{a2r} \\ i_{b2r} \\ i_{c2r} \end{bmatrix} \\
 &= \frac{d}{dt} L_{ms} \begin{bmatrix} i_{a1s} \cos \theta_r + i_{b1s} \cos(\theta_r + \frac{2\pi}{3}) + i_{c1s} \cos(\theta_r + \frac{4\pi}{3}) + i_{a2s} \cos(\theta_r + \frac{\pi}{6}) + i_{b2s} \cos(\theta_r - \frac{\pi}{2}) \\ i_{a1s} \cos(\theta_r + \frac{4\pi}{3}) + i_{b1s} \cos \theta_r + i_{c1s} \cos(\theta_r + \frac{2\pi}{3}) + i_{a2s} \cos(\theta_r - \frac{\pi}{2}) + i_{b2s} \cos(\theta_r + \frac{\pi}{6}) \\ i_{a1s} \cos(\theta_r + \frac{2\pi}{3}) + i_{b1s} \cos(\theta_r + \frac{4\pi}{3}) + i_{c1s} \cos \theta_r + i_{a2s} \cos(\theta_r + \frac{5\pi}{6}) + i_{b2s} \cos(\theta_r - \frac{\pi}{2}) \\ i_{a1s} \cos(\theta_r + \frac{11\pi}{6}) + i_{b1s} \cos(\theta_r + \frac{\pi}{2}) + i_{c1s} \cos(\theta_r + \frac{7\pi}{2}) + i_{a2s} \cos \theta_r + i_{b2s} \cos(\theta_r + \frac{2\pi}{3}) \\ i_{a1s} \cos(\theta_r + \frac{7\pi}{2}) + i_{b1s} \cos(\theta_r + \frac{11\pi}{6}) + i_{c1s} \cos(\theta_r + \frac{\pi}{2}) + i_{a2s} \cos(\theta_r + \frac{4\pi}{3}) + i_{b2s} \cos \theta_r \\ i_{a1s} \cos(\theta_r + \frac{\pi}{2}) + i_{b1s} \cos(\theta_r + \frac{7\pi}{2}) + i_{c1s} \cos(\theta_r + \frac{11\pi}{6}) + i_{a2s} \cos(\theta_r + \frac{2\pi}{3}) + i_{b2s} \cos(\theta_r + \frac{4\pi}{3}) \end{bmatrix} \quad (C.13)
 \end{aligned}$$

Since the zero-sequence components of the rotor currents are zero, the following relation holds true

$$i_{a1r} + i_{b1r} + i_{c1r} = i_{a2r} + i_{b2r} + i_{c2r} = 0 \quad (C.14)$$

Thus, the sum of all back EMFs E_{ks}'' is again zero,

$$E_{a1s}'' + E_{b1s}'' + E_{c1s}'' = E_{a2s}'' + E_{b2s}'' + E_{c2s}'' = 0 \quad (C.15)$$

This relation is valid regardless of the stator winding neutral point configuration.

Based on (C.11), (C.12) and (C.15), it can be concluded that the back EMF of the machine sums to zero even in the event of an open-circuit phase fault. For the case of two isolated neutrals,

$$\begin{aligned}
 E_{a1s} + E_{b1s} + E_{c1s} &= 0 \\
 E_{a2s} + E_{b2s} + E_{c2s} &= 0
 \end{aligned} \quad (C.16)$$

while for the case of a single isolated neutral,

$$E_{a1s} + E_{b1s} + E_{c1s} + E_{a2s} + E_{b2s} + E_{c2s} = 0 \quad (C.17)$$

These conclusions are used in the analysis and derivations presented in Section 5.4.1.2 of Chapter 5.

Appendix D

PUBLICATIONS FROM THESIS

IEEE Transactions Papers

1. Che, H.S., Levi, E., Jones, M., Duran, M., Hew, W. P., Rahim, N.A., 2013b. Operation of a six-phase induction machine using series-connected machine-side converters. *IEEE Trans. on Industrial Electronics* (accepted; available in IEEE Xplore as early access).
2. Che, H.S., Levi, E., Jones, M., Hew, W. P., Rahim, N. A., 2013c. Current control methods for an asymmetrical six-phase induction motor drive. *IEEE Trans. on Power Electronics* (accepted; available in IEEE Xplore as early access).

Conferences (published unless indicated otherwise)

3. Che, H.S., Duran, M. J., Hew, W. P., Rahim, N. A., Levi, E., Jones, M., 2012a. Dc-link voltage balancing of six-phase wind energy systems with series-connected machine-side converters and NPC grid-side converter. In *Annual Conference of IEEE Industrial Electronics Society IECON*. Montreal, Canada, pp. 3541–3546.
4. Che, H.S., Hew, W. P., Rahim, N. A., Levi, E., Jones, M., Duran, M. J., 2012b. A six-phase wind energy induction generator system with series-connected DC-links. In *IEEE Power Electronics for Distributed Generation Systems PEDG*. Aalborg, Denmark, pp. 26–33.
5. Che, H.S., Hew, W. P., Rahim, N. A., Levi, E., Jones, M., Duran, M. J., 2012c. Current control of a six-phase induction generator for wind energy plants. In *International Power Electronics and Motion Control Conference, EPE-PEMC ECCE Europe*. Novi Sad, Serbia, CD-ROM.
6. Che, H.S., Duran, M.J., E. Levi, Jones, M., Hew, W.P., Rahim, N.A., 2013a. Post-fault operation of an asymmetrical six-phase induction machine with single and two isolated neutral points. In *IEEE Energy Conversion Congress and Exposition, ECCE*. Denver, Colorado, USA (accepted).